國立中山大學材料與光電科學學系

碩士論文

鉬與鋯之奈米晶薄膜之晶粒成長與機械性質

Grain Growth and Mechanical Properties of Nanocrystalline Mo and Zr Thin Films

研究生：王顗任 撰

指導教授：黃志青 博士

中華民國 九十九 年 七 月

國立中山大學研究生學位論文審定書

本校材料與光電科學學系碩士班

研究生王顗任（學號：M973100021）所提論文

鉬與鋯之奈米晶薄膜之晶粒成長與機械性質
Grain Growth and Mechanical Properties of Nanocrystalline Mo and Zr Thin Films

經本委員會審查並舉行口試，符合碩士學位論文標準。

學位考試委員簽章：

高伯威　　

張文昌　　黃志青

指導教授　黃志青

系主任/所長　陳明

致謝

兩年的時光轉眼就到了，又到了說再見的時刻。遙想兩年前剛入學的時候，對中山的一切都懵懵懂懂，幸好遇見了我的恩師黃志青教授，讓我有幸加入黃幫。兩年來，老師不僅僅在學業上進行指導，在生活方面也時常關心學生們的狀況，而每個月的助教費更是我經濟上重要的來源，能夠加入黃幫，是我做過最正確的選擇。感謝貴儀中心的王良珠小姐、林明政先生、陳貴香小姐、李秀月小姐，感謝你們在實驗上提供的協助，還有奈米中心與奈米核心實驗室，尤其感謝 FIB 技術員陳彥文學長，總是能在預期的時間內將我的試片完成。感謝擔任我口試委員的高伯威教授與謝克昌教授，由於你們寶貴的建議與指正，才使得論文更加完備。

感謝實驗室的所有成員，陪我走過兩年的時光。感謝李敬仁學長、陳海明學長、賴炎暉學長三位博士後研究員，感謝你們在我實驗遇到瓶頸時提供意見，還有百忙之中還要修改我的論文。感謝周鴻昇學長、劉名哲學長、裴浩然學長，感謝你們在實驗方面提供的協助，教導我儀器的使用與數據分析，還有選課時提供建議。感謝郭哲男學長、宋大豪學長，感謝你們實驗上的幫助，以及為實驗室帶來歡樂的氣氛。感謝我的同學官聖堯與孫碩陽，以及可愛的學弟妹柏佑、逸志、婷婷、瀚生，感謝你們在實驗上與生活上的瑣事給予幫助。還有遠在美國的羅友杰學長，感謝你對我的建言，還有常常開團考察美食。

最後感謝我的父母與家人，讓我在生活、學業、實驗各方面都無後顧之憂，有你們的支持才會有今天的我。也感謝 EQ 成長團體的各位，在長達一學期的團體中，給予我支持與安慰。要感謝的人實在太多了，所以還是感謝天吧。Thank you, God.

Content

List of Tables

List of Figures

中文摘要

在本論文中，探討了鉭與鋯之奈米晶薄膜之機械性質。實驗中使用的鉭與鋯之奈米晶薄膜係使用直流磁控濺鍍製備，並經過快速退火系統退火，接著使用 X 光繞射儀與穿透式電子顯微鏡觀察，最後使用奈米壓痕系統量測其機械性質。經過退火後的鋯薄膜，其平均晶粒大小較高溫濺鍍的薄膜來得高，但因熱震影響，使其產生脫膜現象。而由 X 光繞射圖求得之平均晶粒大小與穿透式電子顯微影象相近，其差距可視為誤差。鉭之奈米晶薄膜經由拉伸與奈米壓痕測試，其薄膜在拉伸過程中發生脫膜現象，吾人將其歸因於薄膜的蜂巢狀結構所致。在鋯之奈米晶薄膜方面，其 X 光繞射圖與穿透式電子顯微鏡觀察皆指出，在鍍膜溫度小於 300 °C 時，晶粒並無明顯成長，要使其晶粒明顯成長，鍍膜溫至少要大於 300 °C。經過奈米壓痕測試後，在鍍膜溫度 400 °C 的試片，其硬度與彈性係數皆高於其它試片。經與大晶粒之鋯金屬做比較，吾人認為其 Hall-Petch 關係式中的斜率 k 相當小，且是在鋯之奈米晶薄膜之範圍。

Abstract

In this study, the mechanical properties of nanocrystalline Mo and Zr thin films are examined. The specimens of nanocrystalline Mo and Zr thin films were all fabricated by DC magnetron sputtering at various temperatures. These specimens were annealed in RTA system and then investigated by X-ray diffractormeter as well as TEM. After that, nanocrystalline Mo and Zr thin films were tested by nanoindentation. The average grain sizes in Zr thin films annealed are larger than deposited at high temperature, but the films after annealing are stripped away from the substrates due to the thermal shock. The average grain sizes estimated by XRD patterns are in common with those estimated by TEM images. We suggest that the difference is deviation. Nanocrystalline Mo thin films were first tested by both nanoindentation and tensile tests. Mo thin films were stripped away during tensile tests. We consider that the phenomenon is due to the honeycombed structure of the films. The X-ray diffraction patterns and TEM observations indicated that there is no evident grain growth in the nanocrystalline Zr thin films, deposited at 100 °C, 200 °C, and 300 °C, except at 400 °C. The deposition temperature for apparent grain growth in the Zr thin films is at least above 300 °C. After nanoindentation tests, the hardness (*H*) and Young's modulus (*E*) of specimens deposited at 400 °C are higher than that of other specimens. Compared to coarse-grained Zr metals, we suggest that the slope k in the Hall-Petch relationship is quite

small and in the range of nanocrystalline Zr thin films.

Chapter 1 Introduction

1.1 Nanocrystalline materials

Nanocrystalline materials were defined as the materials with the grain sizes smaller than 100 nm, as reported by Birringer et al. [1]. They found a novel type of solid structure which is without any short or long range order and called that a "gas-like solid". Over the past decades, nanocrystalline materials have attracted extensive interests due to their novel properties, such as high strength and increasing strength/ductility with increasing strain rate, termed as high strain rate sensitivity, which is different from the corresponding coarse-grained counterparts [2, 3].

Hall-Petch equation is a well-known equation describing the relationship between yield strength and grain size [4, 5]:

$$\sigma = \sigma_0 + kD^{-1/2}, \tag{1-1}$$

where σ is the yield strength, D is the average grain size in diameter, σ_0 is the friction stress (the overall resistance of crystal lattice to dislocation movement), and k is the constant which depends on materials. On the basis of Equation (1-1), the strength of nanocrystalline materials will be quite high because of small D values. The variation of flow stress as a function of grain size in coarse-grained and nanocrystalline materials is shown in Figure 1.1. In coarse-grained region, yield stress increases with grain refinement as shown in Figure 1.1. It is well fitted based on Equation (1-1). The concept of dislocation pileup [6] was commonly

used to explain the deformation mechanism of coarse-grained materials. Nevertheless, the slope k changes in nanocrystalline region and becomes negative when grain size is reduced to the value smaller than 10 nm. This phenomenon is called “inverse Hall-Petch” behavior [7-9].

Nanocrystalline materials start localized deformation when adequate work hardening mechanism is absent under deformation process. Thus, shear bands are formed along the shear plane, suggesting that the formation of shear bands occur not only in amorphous polymers and metallic glasses but also in nanocrystalline materials [10]. Jia et al. [11] have reported that nanocrystalline Fe metal with the body-centered cubic (bcc) structure deforms through the formation of shear bands at quasi-static strain rates in room-temperature compression, which can be seen in Figure 1.2. They further have indicated that the band width decreases with decreasing grain size and decreasing strain. Localized shear bands were also found in other bcc metals and alloys [12-14].

As well known, strain rate sensitivity is a function of strain rate and defined by the following equation [15]:

$$\sigma = k\dot{\varepsilon}^{m}, \tag{1-2}$$

where σ is the flow stress, $\dot{\varepsilon}$ is the true strain rate, and k is a constant. The m values of most normal metals at room temperature are lower than 0.1 whereas those of superplastic metals are higher than 0.4 [15]. Strain rate sensitivity is a crucially important factor in superplastic deformation behavior. Superplastic materials usually exhibit a high value of strain rate sensitivity. Although no room-temperature superplastic behavior in nanocrystalline metals was reported, a higher m value was obtained in nanocrystalline materials [16]. Schwaiger et

al. [17] found the *m* value of nanocrystalline Ni metals with an average grain size of 30-40 nm, prepared by electrodepsition, is 0.02. In their studies, two different experimental techniques of depth-sensing instrumented indentation and tensile testing were applied for the measurement of *m* value. The data obtained from the tensile testing are indicated in Figure 1.3. In addition, it was found that the flow stress of nanocrystalline Ni metal increases with increasing strain rates. Figure 1.4 provides a summary of experimental results on the effect of applied strain rate. As shown in Figure 1.4, it is evident that the *m* value of nanocrystalline materials is much higher than that of their coarse-grained counterparts.

1.2 Molybdenum

Molybdenum (Mo), whose atomic number is 42, is an element of sixth group as well as Cr and W. Its melting point is 2620 °C, which is the sixth highest of all elements in the periodic table of elements. Thus, most Mo metals and alloys were prepared by sintering due to its high melting point. Mo exhibits the unique physical and chemical properties, such as good thermal conductivity, low electrical resistivity, high strength, and low thermal expansion. Moreover, in room temperature, stable chemical reaction makes Mo resist most kinds of acids and alkalis. However, although Mo is stable in air at room temperature, it starts to oxidize at 250 °C. The oxidization reaction increases with increasing temperature. Due to the unique physical and chemical properties, Mo is widely used in refractories, semiconductor industry, optoelectronics, and aeronautics. The fundamental data related to Mo are tabulated in the Table 1.1.

In mechanical properties, Mo metal due to their high melting point (2620 °C) and high recrystallization temperature shows a high stiffness at high temperature and good resistance

against creep resulting in the applications on the heating furnaces. However, the heating temperature of Mo can only reach 1650 °C in vacuum or noble gas since it is easy to oxidize at high temperature as mentioned above [18].

The thermal conductivity of Mo is about one-third value of Cu, which is still higher than that in most metals in addition to Cu, Ag, and Al. Besides thermal conductivity, the thermal expansion coefficient of Mo (5.5 μm/m°C) is similar to that of Si (4.1 μm/m°C) and, thus, the thermal stress at the interface between Mo and Si should be quite low [19]. This will cause a well coherent interface between Mo and Si, which will be beneficial to the subsequent mechanical measurement.

1.3 Zirconium

Zirconium (Zr), whose atomic number is 40, is a transition element of fourth group as well as Ti and Hf. It is a lustrous and malleable metal and its melting point is 1855 °C. The α-Zr is hexagonal close-packed (hcp) from 25 to 863 °C, and the β-Zr is bcc from 863 to 1855 °C. Zr has the fourth lowest eletronegativity, which is 1.33 on the Pauling scale, after yttrium, lutetium, and hafnium. The modulus and thermal expansion coefficient of Zr are 89.8 GPa and 5.9 μm/m°C, respectively. The other properties of Zr are listed in Table 1.2.

Zr exhibits a good resistance to corrosion, so it is usually used in surgical appliances, vacuum tube getters, or as an alloying agent in steels. About 90 pct of all Zr produced is used in nucleation reactors because of its low absorption of neutrons and good resistance to corrosion. Polycrystalline Zr films are used in thin multilayers for various applications [20-22]. Baudry et al. [20] had studied the structure and magnetic behavior of Zr-Ho mutilayers.

They found that Ho-Zr interfaces generate an out-of-plane contribution to magnetic anisotropy in the multilayers. The interface anisotropy is oriented perpendicular to the basal plane of the hcp structure and increases with the thinner Ho layers. Liu et al. [22] used nanocrystalline Zr layers (~30 nm in grain size) to improve the ductility of ZrCu metallic glass. They found that the thin film metallic glass could become highly ductile at room temperature and thought that a nanocrystalline Zr layer could block or absorb the shear band propagation in the interface of Zr and ZrCu metallic glass.

1.4 Motivation

In the past decades, bcc and hcp nanocrystalline metals were reported much less than face-centered cubic (fcc) nanocrystalline metals. It was found that there is the formation of shear bands in bcc nanocrystalline metals in some circumstances [11-14], but not in most reported fcc nanocrystalline metals. The deformation mechanisms of bcc nanocrstalline metals may be different from those in fcc nanocrystalline metals in some circumstances. For hcp materials, it has been reported that deformation twin played a major role in the deformation of Zr metal. It deformed by several modes: prismatic, pyramidal, and basal slip, two types of tensile twinning: $\{10\bar{1}2\}<10\bar{1}\bar{1}>$ and $\{11\bar{2}1\}<11\bar{2}\bar{6}>$, and two types of compression twinning: $\{11\bar{2}2\}<11\bar{2}\bar{3}>$ and $\{10\bar{1}1\}<10\bar{1}\bar{2}>$ [23, 24]. In the range of nanocrystalline grain sizes, hcp nanocrystalline metals were reported much less than fcc nanocrystalline metals. It is reasonable to assume that the deformation mechanisms of hcp nanocrstalline metals should be different from those in coarse-grained counterparts in some circumstances. We note that Mo and Zr are good candidates as bcc and hcp nanocrysalline metal due to its unique natures. In this study, we prepare nanocrystalline Mo and Zr thin

films by sputtering and investigate their mechanical properties.

According to Hall-Petch equation [4, 5], the strength and hardness of polycrystalline materials increase with decreasing grain size. Thus, nanocrystalline metals must show their extremely high strength, which has never been seen before. Nevertheless, there is a critical grain size for the transition of Hall-Petch behavior. Once the grain size of nanocrystalline metals is smaller than a critical value, the inverse Hall-Petch behavior will occur [25]. It was argued that there are lots of defects and porous in the nanocrystalline metals, which was reported in early years, due to the fabrication methods. Recently, it was reported that there were some nanocrystalline metals with few defects and porous made by electrodeposition [8, 26-30]. The quality of nanocrystalline metals prepared by electrodeposition are much better than those by other methods. However, nanocrystalline Mo and Zr metals are unable to be deposited by electrodeposition. As time goes by, vacuum systems are improved substantially. It allows to easily deposit high quality films and control grain size easily through vapor deposition. It suggests that nanocrystalline Mo and Zr films with various grain sizes can be deposied by sputtering and heat treatment. These films with various grain sizes will be used for the examination of Hall-Petch behavior.

The properties of polymers are quite different from those of metals. Some literatures reported that polymers have been widely used as the substrate and metal films were deposited on polymers [31-36]. A simple equation for the analysis of the mechanical properties of metal films and substrates was proposed. It can be roughly expressed as [31, 32]:

$$F_{total} = F_{polymer} + F_{film}, \tag{1-3}$$

where $F_{polymer}$, F_{film}, and F_{total} are the force on polymer, film, and both, respectively. A scheme was illustrated in Figure 1.5. Based on Equation (1-3), we can extract the strength of metal films from the substrate easily.

In this study, nanocrystalline Mo and Zr thin films prepared by sputtering are investigated in terms of the relationship between their mechanical behaviors and average grain size under tensile and nanoindentation tests, especially for deformation mechanisms. The Hall-Petch equation is applied to examine the dependence of strength and grain sizes in the nanocrystalline Mo and Zr thin films. The reliability and sensitivity of the mechanical properties of the nanocrystalline Mo and Zr thin films are discussed.

Chapter 2 Background and literature review

2.1 Fabrication methods

There are three kinds of fabrication methods of nanocrystalline materials:

(1) Mechanical alloying:

It includes cryomilling in a liquid nitrogen medium. It has been used to manufacture nanocrystalline materials in reasonable qualities and the resulting powder has been hot consolidated to near-full density with insignificant grain growth [37, 38]. It is the key to maintain the fine grains during consolidation that the presence of fine oxides or nitrides resulting from the milling process. The advantage of this process lies in its ability to produce reasonable size billets of material, its disadvantages include the inability to control material purity and obtain full density.

(2) Electrodeposition:

It includes direct current and pulse electrodeposition. It has been used to deposited sheets of nanocrystalline metals, such as Ni, Co, and Cu [27, 38-40]. Grain size can be controlled and sheets with thickness of 100 μm or more are repeatedly produced. The other advantages are that the absence of a columnar structure, and the presence of clusters of grains with minimal misorientation between each other. Although electrodeposition is commonly used to deposit nanocrystalline metals, there still are some problems waiting to be solved. Hydrogen levels in the deposition can be substantial and form hydrogen-filled nano-bubbles in the microstructure even though

full-density is measured.

(3) Gas-phase condensation:

So far, oven sources, sputtering sources, electron gun evaporation, and laser evaporation have been utilized. Sanders et al. [41, 42] produced power particles with grain size from 5 to 50 nm, and then the particles are consolidated by high pressure and additional thermal energy. Hugo et al. [43] synthesized two uniform 100 nm thick Ni films by using pulsed laser deposition and DC magnetron sputtering. Both films had grain size under 50 nm and were so transparent to electrons that can be observed by TEM without thinning procedure. Therefore, sputtering seems to be suitable for the production of nanocrystalline films. The application of a commercially available magnetron sputtering device for preparation of metallic and ceramic nanocrystalline materials (Al, Mo, W, Cu, Ti, TiO_2, NiO and ZrO_2) with grain size form 7 to 50 nm has been studied [44].

2.2 Sputtering

Sputtering which is a physical process uses plasma to bombard a negative bias target and eject the atoms of target surface through momentum transfer to deposit on substrates. Plasma is a kind of gas which contains ions, electrons, and neutrons [45]. The electrons between two electrodes are energetic to collide the gas molecules or atoms because of the strong electric fields. In the specific zone, the gas molecules or atoms are through the procedures of dissociation, ionization, excitation, charge transformation, and recombination to produce plasma. There are two types of the electrons of plasma: the electrons produced by molecules or atoms dissociation, and secondary electrons produced by ion bombardment to the cathode.

The gas molecules or atoms gain the energy from the excited electrons to glow discharge. There are five zones of glow discharge:

(1) Cathode glow:

The positive ions are neutralized in this zone.

(2) Cathode dark space or Crook's dark space:

In this zone, the electrons emitted from cathode are less energetic and the concentration of positive ions is too high, so it is a dark space here.

(3) Negative glow:

Secondary electrons are energetic enough to ionize and excite the gas molecules or atoms. Thus, it is the brightest zone. The substrates are put in this zone during sputtering.

(4) Faraday dark space and Positive column:

It is necessary for Faraday dark space and positive column that the distance between the two electrodes must be long enough. In general sputtering systems, these two zones are nonexistent.

The inert gasses are Argon regularly, and sometimes are Kr, N_2, O_2 and so on.

The sputtering yield, Y, is the ratio of the number of emitted atoms per incident ion. It is shown in Equation (2-1) [46]:

$$Y = \text{number of emitted particles} / \text{number of incident particles.} \quad (2\text{-}1)$$

The yields are completely identical whether the bombardment caused by an ion or an atom. Physical sputtering relies on the transfer of momentum and kinetic energy from incident particle to the surface atom. Consequently, the sputtering yields are independent of the charge

of particle. The scheme of physical sputtering process is shown in Figure 2.1.

The advantages for using sputtering include: excellent uniformity of large area film, easy to control surface roughness of film, and able to produce various films from targets. There are different kinds of sputtering.

2.2.1 DC sputtering

The characteristic of DC sputtering is that two diodes must be conductors. One of them is target. If target is not conductor, there will be gas ions accumulated on one diode. The movement of gas ions will get stop when the charges are saturated. Hence, DC plasma will terminate if target is not conductor.

Electric field accelerates free electrons to collide with gas molecules or atoms. After the collision, it makes gas molecules or atoms dissolved, ionized, or excited. The gas ions due to the collision are also accelerated by electric field, and bombard the surface of target. Then there are more free electrons produced. These loops make DC plasma keep continuous.

2.2.2 RF sputtering

Unlike DC sputtering, the power supply for RF sputtering is operated at high frequency [46]. The most common frequency is 13.56 MHz which is in the range of radio frequency, so called RF sputtering. Some experiments have run the gamut from 60 MHz to 80MHz or more. The cathode and anode are electrically reversed in a part of the RF cycle. It eliminates the

charges accumulated on an insulating surface by providing an equal number of opposite charges. Therefore, insulators or metals can be sputtered in RF cycles [46].

Another advantage of RF sputtering system is that the oscillation of electric fields results in the extra movement of free electrons within plasma. The most interesting description is an analogy to the electron "surfing" on the electric field waves in plasma [46]. This phenomenon enhances the possibility of a collision between free electrons and gas molecules or atoms, and results in higher plasma density compared to DC sputtering. The result causes higher ion currents to cathode and a faster sputter rate.

2.2.3 Reactive sputtering

Reactive sputtering is a kind of sputtering, which introduced reactive gases into the chamber during sputtering process. Most chemical compound targets are made by powder sintering, so there will be some gases within the voids and impurities. Reactive sputtering not only utilizes the principle of physical vapor deposition (PVD), but also combines the advantage of plasma to enhance the chemical reaction during chemical vapor deposition (CVD). Hence, it is able to sputter at low temperature and use the high purity metal target and reactive gas [47].

2.2.4 Magnetron sputtering

During sputtering, there are 70% of the energy transferring to heat, 25% transferring to excite secondary electrons, and only 2.2% transferring to sputtering. Adding a static magnetic

field at the cathode location can enhance the sputtering rate, called magnetron sputtering. The magnetic field is located parallel to the cathode surface. The electrons within the dual fields will move on spiral. This raises the probability of collision between free electrons and gas molecules or atoms. The well-known relationship between Lorentz force $\vec{F}$ and electric field force $\vec{E}$ is shown in Equation (2-2) [46]:

$$\vec{F} = m\frac{d\vec{v}}{dt} = -q\left(\vec{E} + \vec{v} \times \vec{B}\right), \tag{2-2}$$

where $\vec{B}$ is the magnetic field of strength; m, q, and $\vec{v}$ are electron mass, charge, and velocity, respectively.

According Equation (2-2), secondary electrons, which are emitted from the cathode due to ion bombardment, are limited to move in the direction perpendicular to both the electric field and the magnetic field. It is called the $\vec{E} \times \vec{B}$ drift, which is also relative to the Hall effect. This drift causes electrons move on spiral, and there will be more chances to collide gas molecules or atoms to produce plasma. The magnetic field is set up correctly, it can make the $\vec{E} \times \vec{B}$ drift be arranged to close target, and a current loop of drifting secondary electrons will be formed. There is a simple scheme shown in Figure 2.2. The magnetic field configuration for a circular planar magnetron cathode is shown in Figure 2.3.

Unlike the DC and RF diodes, these secondary electrons are constrained in the region near by the cathode. Eventually, the kinetic energy of secondary electrons gets lost because of collision with gas atoms (ionizing) or other electrons (electron heating), and results in extremely dense plasma in the drift region. There is no doubt that the plasma density is much higher in the region and will etch a ring pattern on cathode.

In magnetron sputtering system, there are more secondary electrons and extremely dense plasma resulted from the high possibility of the collision between ions in the drift region and cathode. The relationship between voltage and current in a magnetron sputtering system is shown in Equation (2-3) [46]:

$$I = kV^n, \tag{2-3}$$

where I and V are the discharge current and voltage respectively, and k and n are system material and gas-dependent constants. According to Equation (2-3), the discharge current in magnetron sputtering system is obviously much higher than typical sputtering system at the same voltage.

2.2.5 Nucleation and growth of sputter-deposited films

As the molecules or atoms of materials arrive the substrate surface, the adsorption, re-evaporation, surface diffusion, nucleation, and growth processes occur, and then start to deposit as a film. The nucleation and growth modes of thin films are dependent on the properties of as-deposited films such as thin film density, surface morphology, and grain size. Several considerable aspects of film growth are shown as follows [48]:

(1) Substrate surface and roughness − initially and as the thin film grows

(2) Surface temperature − initially and as the thin film grows

(3) Adatom surface mobility

(4) Geometrical showing effects (angle-of-incidence effects)

(5) Reaction and mass transport during deposition such as segregation effects and void

formation

While thin film grows, the surface roughness increases with various grow rate of planes due to some features or crystallographic. It starts to nucleate and grow on the substrate surface when the adatom flux onto the substrate surface exceeds the flux of adatoms leaving from the substrate surface. The nucleation process is controlled by adsorption energy between the adatoms and substrate or growing films, the surface diffusion energy required to transfer an adatom to an adjacent adsorption site, and the binding energy between adatoms [49, 50]. In reality, the migration of adatoms is not random but dependent on the substrate crystallographic direction and surface topography as well as other external conditions such as temperature [50]. The surface diffusion is rapid at high temperature, and that will affect the surface roughness. Some processes, such as recovery, recrystallization, and grain growth, also get promoted at high temperatures. Thin film quality may be controlled by these parameters.

Basically, film formations have three basic growth modes: island (or Volmer-Webber) mode, layer (or Frank-Vander Merwe) mode, and Stranki-Krastanov mode. These are illustrated schematically in Figure 2.4 and described as follows:

(1) Island (or Volmer-Webber) mode:

When atoms or molecules in the deposit are more strongly bound to each other than to substrate, the smallest stable cluster nucleates on the substrate and grows in three dimensions to form an island. Thus, it is called island mode. Many systems of metals on insulators, alkali halide crystals, graphic, and mica substrates are of this growth mode.

(2) Layer (or Frank-Vander Merwe) mode:

When the binding energy between coating atoms to substrate atoms is stronger than that between coating atoms, the first arriving atoms will condense as a single monolayer and there is no energy barrier for nucleation. It begins to grow as two dimensional layer-by-layer, and therefore is called layer mode. This growth mode occurs for heterepitaxial thin film growth in semiconductor-semiconductor systems and some metal-metal systems.

(3) Stranki-Krastanov mode:

It is essentially a combination of the layer-by-layer and island growth modes. In this case, one or more monolayers form first, and then subsequent layer growth becomes unfavorable and islands thus form. This growth mode is fairly common and has been observed in metal-metal and metal-semiconductor systems.

2.2.6 Thornton zone

A general film morphology for sputtering which was first proposed by Movchan and Demchishim in 1969 [51]. A modified zone scheme was introduced later by Thornton [52, 53] and is shown in Figure 2.5.

In Figure 2.5, the microstructure of zone 1, which occurs at substrate temperature lower than 0.15 T_m, is porous and consists of tapered crysatllites separated by voids. This open columnar microstructure forms because very limited surface mobility disallows the adatoms to fill the intercrystallite valleys shadowed by the crystallite peaks. Zone T, which is with

fibrous columnar grains and density greater than zone 1, occurs at the temperature region from 0.15 T_m to 0.45 T_m. In the temperature region from 0.45 T_m to 0.7 T_m, zone 2 occurs, and the microstructure is controlled by surface diffusion. Lattice diffusion (or bulk diffusion) dominates the equiaxed grain microstructure in zone 3 at the further high substrate temperature higher than 0.7 T_m.

It is the ultimate motivation for depositing materials to a substrate from vapor phase to form useful engineering products. Extensive researches to date have already provided great insight into what parameters of vapor deposition process affect the development of the deposited material microstructure. To fabricate films reproducibly and to understand how the entire deposition process dominates the film microstructure and properties, film growth has been investigated through lots of experiments. Most of these researches have concentrated upon that the final physical properties of films in engineering application are affected by the critical microstructural variables, such as the occurrence of point, linear, and planar defects during film nucleation and growth, and the formation of amorphous, polycrystalline, or single crystal deposits,. The most important factors affecting vapor deposited materials growth are [54]:

(1) Elemental composition of the depositing atoms.

(2) Film growth temperature.

(3) Deposit thickness.

(4) Substrate materials, cleanliness, crystallinity, and orientation.

(5) Deposition rate.

(6) Kinetic energy of the atoms landing on the substrate.

(7) The angle of incident vapor atoms.

(8) Presence and nature of a surrounding gas phase.

As these parameters have been identified, it is the desire to develop the process roadmap showing the relationship between the process parameters and microstructures. The roadmap is shown in Table 2.1 which can aid engineers when they design film synthesis equipment. That will help us to produce high quality films.

2.3 Mechanical properties

2.3.1 Strength

On the basis of Equation (1-1), the advantage of nanocrystalline materials naturally raises the expectation of super strong materials. The mechanical properties of metals, mostly fcc metals, with grain size less than 100 nm have been primarily derived from uniaxial tension/compression test and micro- or nano-indentation [27-29, 41, 55, 56]. Hardness and strength have been found to increase with decreasing grain size in the regime down to at least 15 nm. Grain refinement leading to strengthening has traditionally been explained by the concept of dislocation pileups at grain boundaries [6]. Nonetheless there is no experimental confirmation of dislocation pileups in deformed nanocrystalline specimens. Hence, the reason for the continued Hall-Petch relationship down to nanoscale grain size is not fully understood.

The inverse Hall-Petch relationship was reported by Chokshi et al. in 1989 [25], but was later found that it is an artifact due to sample porosity [57]. Few years later, Schuh et al. [7, 9] and Jeong et al. [8] used electrodeposited full density nanocrystalline samples and claimed that strength declined with further grain refinement below a grain size of ~10 nm. In this regime, grain boundary sliding and Coble creep apparently constitute the dominant

deformation modes [58].

2.3.2 Strain rate effect

Some studies have reported that nanocrystalline metals exhibit highly strain rate sensitive under different loading conditions. The investigations also reveal that an increasing strain rate usually raises tensile strength, whereas ductility under different strain rate substantially varies with processing, composition, and testing methods [2]. Cheng et al. [37] observed that the yield strength of nanocrystalline Cu with average grain size 62 nm raised with increasing strain rates. The strain rate sensitivity of the nanocrystalline Cu is 0.0272 which is much high than that of conventional coarse-grained Cu (m=0.006) [59]. These results are shown in Figure 2.6. It is evident that the m values of nanocrystalline Cu at room temperature are up to a factor of 4 compared to conventional coarse-grained Cu. This phenomenon was also found in nanocrystalline Ni, as shown in Figure 2.7.

2.3.3 Localized deformation

In the absence of adequate work hardening mechanisms, local softening caused by thermal or geometrical fluctuations triggers the localized plastic deformation. One possibility is the concentration of large deformation in narrow shear bands similar to those in amorphous materials [10]. The simple force instability in a tensile test, such as necking, can easily develop as predicted by Considere criterion [60]. It is shown in Equation (2-4).

$$\left(\frac{\partial\sigma}{\partial\varepsilon}\right)_{\dot{\varepsilon}} \leq \sigma, \tag{2-4}$$

where σ and ε are true stress and true strain, respectively. Nanocrystalline metals tend to lose the work hardening quickly on deformation owing to their low dislocation storage efficiency inside the tiny grains, and then they would neck right away after the plastic flow commencement.

As we mentioned in Chapter 1, there are shear bands found in bcc metals [10-14]. These shear bands are caused by localized deformation, as shown in Figure 2.8. The grains inside a shear band are elongated, but, by contrast, the grains outside a shear band remain equiaxed. Shear bands are not only in bcc metals but also seen in fcc under some tests. Sanders et al. [41] found shear bands in nanocrystalline Pd under compression testing, and Vinogradov et al. [61] found shear bands in nanocrystalline Cu under fatigue testing. However, shear banding has been undiscovered to be a common mode of deformation for all nanocrystalline materials.

2.4 Deformation mechanisms

2.4.1 Hall-Petch relationship

Hall-Petch equation has widely used to predict the effect of grain size on strength for polycrystalline materials. At grain sizes smaller than 100 nm, nanocrystalline metals seldom follow Hall-Petch type strengthening with grain refinement. Furthermore, below a certain transition grain size, on the order of 5-15 nm in fcc metals, there is a region in which strength and hardness decline with decreasing grain size. This phenomenon is shown in Figure 1.1.

In the TEM observations, it has filed to discover any evidence of dislocation pileups or dislocation tangles in deformed nanocrystalline metals [62]. Budrovic et al. [63] used in-situ X ray peak broadening experiment to detect the dislocation in nanocrystalline Ni, and they also found the absence of dislocation storage in it. These results suggest that these classic work hardening models are inappropriate for nanocrystalline metals, even if Hall-Petch relationship is suitable in the region from 10 to 100 nm. Instead, the dislocation activity of nanocrystalline metals is fundamentally different from that of coarse-grained metals.

2.4.2 Grain boundary activity

Nano grain rotation via grain boundary sliding has been predicted to be an important deformation mode in nanocrystalline materials with grain size smaller than 10 nm [64-66]. Reducing the grain size and increasing the fraction of the grain boundary atoms lead to extra grain boundary sliding and softening of the material consistent with reported inverse Hall-Petch behavior.

Shan et al. [67] reported in situ straining dark field transmission electron microscope observation of grain rotation in nanocrystalline Ni. They revealed that continuous grain contrast changed and the plastic deformation of nanocrystalline Ni via the grain rotation. This results from grain boundary sliding, which requires short range atomic motion and stress assisted free volume migration but except for long range diffusive processes like Coble creep. Grain boundary activity plays an important role in influencing upon the plastic deformation of nanocrystalline metals. It is evident that dislocation in nanocrystalline metals plays a minor role in deformation mechanisms.

2.4.3 Twinning and partial dislocation

The observation of partial dislocations was rationalized by that partial dislocations are easier to nucleate than perfect dislocations [68]. The stress in the boundary would be reduced immediately by the generation of the first partial dislocation, thereby greatly decreasing the driving force for the second one to form a perfect dislocation. The motion of these partial dislocations would result in the formation of stacking faults or deformation twins.

Twinning is an alternative mode of plastic deformation and it has been observed in conventional fcc metals and alloys with low stacking fault energy [69]. Kumar et al. [30] observed twins during the deformation of electrodeposited nanocrystalline Ni in transmission electron microscope. Compared to nanocrystlline Ni, conventional coarse-grained Ni is prone to twinning during strain annealing. Hydrogen and other interstitial impurities are often present in electrodeposited materials, besides they can influence the twinning stress of the material as well. For instance, it is known that nitrogen lowers the stacking fault energy in stainless steels and encourage twinning [70]. Chen et al. [71] reported deformation twinning in vapor deposited nanocrystalline Al that was severely deformed by micro-indentation and grinding. It was interesting that there were no deformation twin seen in coarse-grained Al. There is a scheme as shown in Figure 2.9.

Research into the structure, deformation and failure of nanocrystalline materials has provided resources of experimental information during the past decade. Grain boundaries play a major role in the structure as well as the deformation behaviors of nanocrystalline materials. Based on this concept, Kumar et al. [30] submitted a model for damage evolution

and fracture, as shown in Figure 2.10. In the early stage of deformation, partial dislocations are emitted from grain boundaries to release the stress accumulated in grain boundaries, as well as grain boundary sliding and rotation facilitate void formation at grain boundaries simultaneously. Triple junction voids and cracks also result from grain boundary movement. These grain boundary and triple junction voids then act as sites for nucleation of the dimples which are several times larger than the individual origin grains. The rim of these dimples on the fracture surface unnecessarily coincides with grain boundaries.

2.5 Nanoindentation

Since the sizes of devices get into the region of nanometers, the mechanical test methods of bulk materials are no longer for use. Therefore, the technologies for testing thin films are developed, and nanoindentation system is one of these. The relationship between load and displacement are used to determine hardness (H) and Young's modulus (E) in nanoidentation system. The relationship between contact area and Young's modulus is able to calculated by using the raw data of load and displacement when specimen is unloading. After that, the area function of indenter can be used to estimate contact area. Then, the hardness and Young's modulus of the specimen are calculated in elastic deformation model.

The hardness of materials is a function of load and contact area. Because of the difficulty in observing the contact area in nanoindentation system, there should be an adequate equation of load and contact area to resolve the problem. Timoshenko and Goodier [72] reported the influence of non-rigid indenter on indentation according to elastic deformation model. They determined the function of reduced modulus (E_r) as shown in Equation (2-5).

$$\frac{1}{E_r} = \frac{1-\upsilon_s^2}{E_s} + \frac{1-\upsilon_i^2}{E_i}, \tag{2-5}$$

where E_s, υ_s, E_i, and υ_i are the Young's modulus and Poisson's ratio of specimen and indenter respectively.

The curve of load versus displacement in nanoindentation system is shown in Figure 2.11, where h_c, h_{el}, and h_{max} are displacement of contact, elastic deformation, and maximum respectively. P_{max}, and S_{max} are the maximum load and contact stiffness respectively. Young's modulus is calculated by contact stiffness, as shown is Equation (2-6) [73].

$$S = \frac{dP}{dh} = \beta \frac{2E_r\sqrt{A}}{\sqrt{\pi}}, \tag{2-6}$$

where β and A is constant of indenter geometry and contact area respectively. When indenter indents the specimen, elastic and plastic deformation will occur at the same time. Elastic deformation will recover elastically during unloading. Hence, elastic contact stiffness (S_{max}) is defined as the derivative of the curve of load versus displacement at maximum load. Pharr et al. [74] had estimated hardness and Young's modulus of materials closely.

Hardness of nanoindentation can be estimated by the average pressure which material can resist under maximum load. It is shown in Equation (2-7) [75].

$$H = \frac{P_{\max}}{A}. \tag{2-7}$$

According to Equations (2-6) and (2-7), contact area and initial contact stiffness are the triggers of these equations. P_{max}, E_i, υ_s, and υ_i, these values are kown. Once contact area and elastic contact stiffness are obtained from data, H, E_r, and E_s, may be calculated by Equation (2-7), (2-6), and (2-5) respectively.

Displacement, h, includes displacement of contact area and surface area. Assume that it is plastic deformation in contact area but pure elastic deformation in other area during loading. Therefore, it gives

$$h = h_c + h_{el}, \tag{2-8}$$

and h_{el} is only relative to elastic deformation during loading. Hence, h_{el} becomes

$$h_{el} = \varepsilon\left(h - h_f\right), \tag{2-9}$$

where h_f and ε are residual depth as indenter entirely removes and constant of indenter geometry. Sneddon [73], Pharr et al. [74] and Oliver and Pharr [75] had introduced a general equation of load, displacement, and contact area from unloading curve. Assume deformation during unloading is completely elastic. The relationship between load and displacement of elastic deformation during unloading is shown as follows:

$$P = B\left(h - h_f\right)^m, \tag{2-10}$$

where B and m are all constants. According to Equation (2-6),

$$S = \frac{dP}{dh} = Bm\left(h - h_f\right)^{m-1}. \tag{2-11}$$

Use Equations (2-10) and (2-11), it is obtained:

$$h - h_f = m\frac{P}{S}. \tag{2-12}$$

Combine Equations (2-9) and (2-12), h_{el} is obtained:

$$h_{el} = \varepsilon\left(h - h_f\right) = \varepsilon m\frac{P}{S}. \tag{2-13}$$

Then, contact depth (h_c) is

$$h_c = h - h_{el} = h - \varepsilon m\frac{P}{S}. \tag{2-14}$$

Contact area (A) can be determined by h_c because A is a function of h_c. As geometry of indenter is identified, equation of A can be defined by curve fitting. It is shown as follows:

$$A = f\left(h_c\right) = c_0 h_c^2 + c_1 h_c^{1/2} + c_3 h_c^{1/4} + \ldots + c_8 h_c^{1/128}, \tag{2-15}$$

where c_0 is a constant for a perfect indenter, and the others are the factor to describe the blunting of tip. For a perfect Berkovish tip, contact area is

$$A = f(h_c) = 24.5h_c^2 . \quad (2\text{-}16)$$

Then, the other parameters can be determined by these equations.

2.6 The factors influencing thin film mechanical properties

2.6.1 Indentation size effect

Hardness of thin films is always higher than bulk materials because the depth of indentation is shallow. The actual contact area is much larger than the value from calculation under a shallow indentation [76]. Accordingly, the value of hardness is overrated. It is known as indentation size effect. The value of hardness will decrease with increasing depth and approach a fixed value.

2.6.2 Surface roughness

There should be a little roughness on specimen surface, and the rough surface will change one-point contact into multi-point contact. This makes the calculation of contact area a deviation. In order to lower the influence of surface roughness, it is useful to increase the depth and size of indenter. The influence of surface roughness had been reported by some literatures [77-79]. In terms of surface roughness theory, it can avoid surface roughness affecting mechanical properties to produce surface with roughness less than 20% of the depth of indentation.

2.6.3 Substrate effect

Nanoindentation system is usually used to determine the mechanical properties of micro- or nanoscale materials. Nevertheless, thickness of thin films is so thin that the values from nanoindentation are affected by the interaction of thin films and substrates [80]. If thin film is softer than substrate and indentation depth is less than thickness of thin film, the influence of substrate on hardness of thin film is less because of plastic deformation constrained in thin film. On the other hand, the external energy is absorbed by substrate rather than thin film if thin film is harder than substrate. Accordingly, plastic deformation will occur in substrate and hardness of thin film will be affected by substrate. Whether thin film is softer or harder than substrate, it is in order to avoid substrate effect that indentation depth is less than 10% of thickness of thin film.

2.6.4 Pile-up and sink-in effect

Pile-up and sink-in usually occur in nanoidentation test. Pile-up will make true contact area more than the value from calculation, but sink-in will make less. These two phenomena result in the deviation, which can be up to 60% [81], of contact area. Nevertheless, Bolshakov and Pharr [81], McElhaney et al. [82], and Miyake et al. [83] had reported using AFM, SEM, finite element simulation, or other facilities for identifying the true contact area to correct the deviation.

Chapter 3 Experimental procedures

3.1 Introduction

In this study, nanocrystalline Mo and Zr thin films are selected as the samples for all the experiments. Nanocrystalline Mo thin films are deposited on different substrates, Kapton® foils and P-type (100) Si wafers, by using the magnetron sputtering system. However, Nanocrystalline Zr thin films are deposited only on the (100) single crystal Si wafers by using the same system. After the deposition, the thickness and the surface roughness of all films can be measured accurately by using the 3D alpha-step profilometer. Grain size of these films is identified by XRD and TEM. Moreover, the nanoindentation tests are conducted on the samples in order to characterize the mechanical properties of the films by a nanoindenter system. Nanocrystalline Mo thin films are carried out with tensile tests by an Instron 5582 universal testing machine. The flow chart of experimental procedures is in shown in Figure 3.1.

3.2 Materials

Kapton® HPP-ST foil with thickness 175 μm was made by Dupont™. The properties of Kapton® HPP-ST foil are shown in Table 3.1. The pure Mo target which was purchased from MUSTEC Co., Ltd, Hsinchu, Taiwan, is used to sputter. The purity level of the target is 99.995%. The pure Zr target which was purchased from Well-Being Enterprise Co., Ltd, Taipei, Taiwan, is used to sputter. The purity level of the target is 99.9%. The diameter of all

targets is 101.6 mm (4 inches) and the thickness is 6 mm.

3.3 Sample preparations

3.3.1 Substrate preparations

Kapton® HPP-ST foils and P-type (100) silicon wafers are used as the substrates in this study. In order to clean the particles, metallic/ionic impurities and greasy dirt which has already existed on the substrates, the following simplified procedures for substrate cleaning are adopted at room temperature.

(1) In order to remove the dust and impurities on the surface of substrates, an ultrasonic cleaner with deionized water (D. I. water) is used to clean substrates for 10 minutes.

(2) Substrates are rinsed in ethanol for 10 minutes by using an ultrasonic cleaner. This is due to removing the greasy and the organic dirt on the surface of substrates.

(3) By using an ultrasonic cleaner, substrates are cleaned in acetone for 10 minutes after rinsing in ethanol. This is due to making sure the greasy and the organic dirt are purged.

(4) After rinsing in acetone, substrates are cleaned in ethanol by an ultrasonic cleaner for 10 minutes. This procedure removes the residual acetone from the surface of substrates.

(5) Substrates are cleaned in the D. I. water by an ultrasonic cleaner for 10 minutes. This procedure removes the residual ethanol from the surface of substrates.

(6) Finally, nitrogen is used to dry substrates.

The films deposited on Kapton® HPP-ST foils are used to tensile test at room temperature. The detailed size and dimension of the dog-bone-shape Kapton® HPP-ST foils is depicted in Figure 3.2. The foils are cut from Kapton® HPP-ST sheet.

3.3.2 Thin film preparations

The machine for sputtering is shown in Figure 3.3. It is a multi-target magnetron sputtering system which was bought from AST-Taiwan. There are three guns in the system, including one DC and two RF target sets. It is applied to co-sputtering any kinds of composite material thin films or depositing semiconductor, dielectric, metal thin films simultaneously. Moreover, the substrate heater is set up in the system and can be introduced into high temperature processes up to 400 °C.

These films are in the form of monolithic films. The diameter and thickness of targets are 101.6 mm (4 inches) and 6 mm, respectively. The substrates are set on a 6 inches disc which is located in the top of chamber and the distance between disc and target is about 80 mm.

There are two sputtering steps in this study. The sputtering processes are described as follows:

(1) Before depositing nanocrystalline Mo and Zr films, Ti thin film is deposited first. For this is to enhance the adhesion between nanocrystalline thin films and substrate. Ti target is set on DC diode and set the power at 150 W. During the sputtering processes, a rotary pump is used to achieve a moderate vacuum and a cryo-pump is used to achieve a base pressure of 1×10^{-5} torr in the main chamber. After achieving the base pressure, pure Ar is introduced into the main chamber as the

working gas. The flow rate of pure Ar is fixed at 30 standard cubic centimeters per minute (sccm) and the pressure is 4 mtorr during the sputtering process. The rotating speed of disc which substrates are set on is 10 rpm during deposition. This rotation can ensure the uniform thickness of all the thin films. Meanwhile, substrates are deposited at room temperature. The deposition time is 60 seconds.

(2) Mo target is set on DC diode and set the power at 200 W. The base pressure is 1×10^{-5} torr. The flow rate of pure Ar is 10 sccm and the pressure is 1 mtorr during sputtering process. The rotational speed of disc is 10 rpm. Substrates are deposited at room temperature. The deposition time is 10800 seconds.

(3) Zr deposition parameters are almost the same as Mo deposition except the deposition time and temperature. The deposition time is 8100 seconds, and the temperature is set from 25 °C to 400 °C.

In order to remove oxide layers and pollutants from the surface of the targets, the pre-sputtering process is executed for 10 minutes before deposition for both sputtering steps. In summary, the details of the sputtering conditions for both sputtering steps are listed in Table 3.2.

3.3.3 Grain growth

Grain growth is a kind of thermal activation process, so heat treatment is a good way to develop larger grains. The rapid thermal annealing system (RTA), which is bought from AST-Taiwan, is used in this study. The samples can be annealed in the system in vacuum or in working gases, such as Ar, H_2, N_2, and O_2.

The samples deposited at room temperature are annealed at 500 °C, 600 °C, and 700 °C, respectively, and the base pressure is 1×10^{-6} torr. The heating rates are all 1 °C per second. Because of the limitation of the machine, the holding time is 300 seconds at all temperatures but 180 seconds at 700 °C.

3.4 Properties measurements and analyses

3.4.1 3D alpha-step profilometer

After deposition of nanocrystalline Mo and Zr thin films by a multi-target magnetron sputtering system, the thickness and surface roughness of these films are measured by a 3D alpha-step profilometer. The Veeco Dektak 150 Stylus profiler 3D alpha-step profilometer, as shown in Figure 3.4, can measure the surface profiles by a mechanical styles. To measure the surface profiles, this stylus move across the specimens with the stylus force of 3 mg. The measurement range of the profilometer is set on 525 μm, and the resolution of the profilometer is 300 datum points per second. Usually, the scanning duration of each specimen is set at least 30 seconds per 500 μm.

3.4.2 X-ray diffraction analysis

Siemens D5000 X-ray diffractormeter is used in the present study. The working voltage and current are set on 40 kV and 30 mA respectively. The size of filter is 0.02 mm. The data are used to analyze grain sizes of nanocrystalline Mo and Zr thin films. The range of 2 theta

is from 20° to 60°, and the scanning rate is 0.02° per second. Because of the peak of single crystal Si substrate at 69°, it should be avoided to prevent the damage on the machine. Then, match the data from JCPDS database.

3.4.3 Scanning electron microscopy

It is a good way to observe the surface of a specimen by scanning electron microscope (SEM). The sample of SEM is easier to prepare than TEM sample. In this study, JEOL JSM-6700F is selected to observe the microstructure and surface morphology of nanocrystalline thin films.

3.4.4 Transmission electron microscopy

The observation of the fine and localized microstructure of the thin films may rely on transmission electron microscope (TEM) due to the resolution restriction of SEM. The cross-sectional plane of the TEM specimens can be prepared via the SMI 3050 focus ion beam (FIB) system. The SMI 3050 FIB system, shown in Figure 3.5, belongs to the dual-beam type of FIB, where one beam can provide a second-electron image to observe the appearance of the specimen, and the other one can provide the etching function by Ga ion beam for the TEM specimen, cross-section image, and patterns and so forth. The specimens are fixed on an Al holder and cleaned by nitrogen. Then, they are moved into the FIB chamber.

There are four main procedures in the FIB-TEM specimen preparation technique. First, in order to protect against the damage of Ga ion beam during the process of preparation, the carbon film is deposited on the sample surface with a small area. Second, the slope-etching is

conducted on the upper and under areas. The TEM specimen in the trapezoid shape is fabricated in this procedure. Third, the trapezoid TEM specimen is thinned out by Ga ion beam until the thickness is less than 100 nm. Finally, the bottom part and both sides of the TEM specimen are cut. The cut TEM specimens are moved to a carbon-coated Cu grid and examined by the JEOL 3010 analytical scanning transmission electron microscopy (AEM). The AEM is operated at 300 keV.

3.4.5 Nanoindentaion tests

After the deposition of thin films on substrates, the nanoindentation tests are conducted by using the MTS XP nanoindenter system, as shown in Figure 3.6, at room temperature. The data are recorded by a computer with TestWorks 4 software. In this experiment, continuous stiffness measurement (CSM) is chosen. In CSM mode, the strain rate and the depth are set on 0.05 s^{-1} and 300 nm, respectively. It is possible by nanoindentation technique to analyze hardness (H) and Young's modulus (E) profiles at very shallow depth. A Berkovich tip is used in the present tests. The shape of Berkovich tip is three sided pyramid of geometrical symmetry, and has a flat profile with a center-to-face angle of 65.3°. Besides, the nanoindenter is extremely sensitive to the external environment and the roughness of specimen surface. It is necessary to keep the specimen surface clean and dry before indentation tests.

3.4.6 Tensile tests

After the deposition of thin films on Pi foils, the constant crosshead speed tensile tests

are conducted by using an Instron 5582 universal testing machine at room temperature. The data are recorded by a computer with Instron Bluehill 2 software. In this experiment, the load cell is 500 kg and the crosshead speeds are respectively 1.5, 7.5, and 15 μm per second. The strain rate are 10^{-4} s^{-1} and 10^{-3} s^{-1}. As for the foil tensile specimens, the over length, gauge length and gauge width are 40 mm, 15 mm, and 3 mm, respectively. The thickness of the dog-bone-shape PI foils is 175 μm. Moreover, the brass clamping apparatus are designed in order to firmly fix the specimen on the instrument. The stress-strain curves are exported after tensile tests. Therefore, the mechanical properties, such as room-temperature yield stress and elongation can be obtained and analyzed further.

Chapter 4 Results and Discussion

4.1 3D alpha-step profilometer examinations

After finishing the sputtering processes, the thickness of monolithic nanocrystalline Mo and Zr thin films was examined by a 3D alpha-step profilometer. The average thickness of nanocrystalline Mo thin films deposited on Si wafers and on Kapton foils for 10800 seconds is almost the same, which is 3.6 μm. The average thickness of nanocrystalline Zr thin films deposited on Si wafers for 8100 seconds is 2.1 μm. These results are including Ti thin films which were deposited for 60 seconds before Mo and Zr sputtering.

4.2 The thin films after annealing

All thin films after annealing are stripped away from the substrates no matter what temperature is. We think there are thermal shocks happening in these samples. Since the thin films are at least 2 μm in thickness, the rapid heating rate is too fast for all samples. The thermal stresses are in the samples, and get more and more. Furthermore, when the thermal stresses are large enough, the thin films get tripped away from the substrates due to the cracks caused by the tresses in the samples. Since the thin films are broken after heat treatment, only nanocrystalline Zr thin films are investigated by X-ray diffractormeter after annealing.

4.3 X-ray diffraction patterns

Scherrer's equation, as shown in Equation (4-1) [84], is a well-known equation to calculate average grain size by X-ray diffraction pattern.

$$D = \frac{\kappa\lambda}{B\cos\theta}, \tag{4-1}$$

B, *D*, θ, λ, and κ are full width at half maximum (FWHM), average grain size, value of 2 theta at maximum peak, incident wave length, and constant, respectively.

Mo thin films

The X-ray diffraction pattern of nanocrystalline Mo thin film on Si wafer is shown in Figure 4.1. The 2 theta range is scanned from 20° to 60°. The strongest peak is at 40.4°. It indicates (110) plane in nanocrystalline Mo thin film. The grain size estimated by Equation (4-1) is 23 nm.

Zr thin films

The X-ray diffraction pattern, scanned from 20° to 60°, of nanocrystalline Zr thin films is shown in Figures 4.2 and 4.3. The strongest peak is at 34.6°. It indicates (0002) plane in nanocrystalline Zr thin film. Based on JCPDS database, the strongest peak should be $(10\bar{1}1)$ plane. It is reasonable to say there should be large number of textures in the nanocrystalline Zr thin films fabricated by sputtering. That makes the other peaks so weak and hard to be recognized.

In Figure 4.2, RT means the specimen deposited at room temperature, and 500C, 600C and 700C indicate the specimens annealed at 500 °C, 600 °C, and 700 °C, respectively. Based on the patterns of Zr thin films, we estimated the grain sizes of specimens by using Equation (4-1). The grain sizes of specimens annealed at room temperature, 500 °C, 600 °C, and 700 °C are 17 nm, 25 nm, 39 nm, and 55 nm, respectively.

In Figure 4.3, RT means the specimen deposited at room temperature, and 100, 200, 300, and 400 indicate the specimens deposited at 100 °C, 200 °C, 300 °C, and 400 °C, respectively. The grain sizes of specimens deposited at room temperature, 100 °C, 200 °C, 300 °C, and 400 °C estimated by Equation (4-1) are 17 nm, 19 nm, 16 nm, 21 nm, and 27 nm, respectively.

4.4 SEM observation

Mo thin films

After deposition, a JEOL 3010 AEM is used to determine the grain size of nanocrystalline Mo thin films. The nanocrystalline Mo thin films deposited on Si wafers are selected for the AEM sample preparation via a SMI 3050 FIB system. Since Kapton is a polymer, there are some forbidden things for polymers in many facilities. Some pictures taken from the nanocrystalline Mo thin film on Si wafer by SMI 3050 FIB system are shown in Figure 4.4. In Figure 4.4, the surface of nanocrystalline Mo thin film on Si wafer is honeycombed. Based on Table 2.1 and Figure 2.5, it seems to be zone 1 in Thornton zone diagram. There are voided boundaries, fibrous grains, and so many pores in this film. We consider that is the reason why the value of E is lower than it of Mo bulk material.

Zr thin films

The surface morphology of nanocrystalline Zr thin film on Si wafer is shown in Figure 4.5, taken by JEOL JSM-6700F. The surface morphology is much flatter than nanocrystalline Mo thin film because melting point of Zr is much lower than Mo, and the grain sizes are smaller than 100 nm. It seems to be zone T in Thornton zone. There should be many columnar and fibrous grains in the film. At least it is much denser than zone 1.

4.5 TEM observation

Mo thin films

Although X-ray diffraction can compute the average grain size, the direct image is more powerful evident. The grain size of nanocrystalline Mo thin film is determined by the direct image taken by JEOL 3010 AEM. The nanocrystalline Mo thin film on Si wafer is chosen as TEM sample prepared via SMI 3050 FIB system. The operation voltage is 200 kV. The selected area diffraction pattern (SADP) is shown in Figure 4.6. Based on Figure 4.6, there is a ring pattern in this figure. It shows that this sample should be a nanocrystalline metal.

There are bright field and dark field images in Figures 4.7 and 4.8. The grain boundaries are apparently seen in these figures. Nonetheless, these grains are columnar and fibrous grains. We consider the width of these grains is the grain size, not the length of the grains. According to Figure 4.7, the average grain size of nanocrystalline Mo thin film is about 25 nm. The dark field images in Figure 4.8 are taken with different diffraction beams at the same

location. It further indicates that these are different grains in various zones. These results are identical to the bright field images.

Zr thin films

The dark field images are shown in Figures 4.9-4.13. These images indicate that there are defects in these samples and the grain boundaries are difficult to be recognized. We took at least 10 pictures for each sample, and then used the software, Optimas, to measure the sizes of the grains we chose. Furthermore, we calculated the average grain sizes of theses grains (at least 200 grains for each sample). The distributions of grain sizes in samples are shown in Figures 4.14-4.18. The average grain sizes are estimated by these data, and the results are consistent with the results estimated by Scherrer's equation. The average grain sizes of specimens deposited at room temperature, 100 °C, 200 °C, 300 °C, and 400 °C are 20 nm, 20 nm, 22 nm, 23 nm, and 30 nm, respectively. These results are shown in Table 4.1. According to Table 4.1, it seems that there should be no (or a little) grain growth in Zr thin films deposited at the temperature range from room temperature to 300 °C.

4.6 Tensile tests on nanocrystalline Mo thin films on Kapton foils

In order to compare the tensile and compression mechanical properties of the nanocrystalline Mo thin films on Kapton foils, the specimens are measured by tensile and nanoindentation tests in this study. The average thickness of nanocrystalline Mo thin films on Kapton foils is 3.6 μm. The uniaxial stress is conducted on the specimens by an Instron 5582 machine at room temperature. The strain rates are 10^{-3} s^{-1} and 10^{-4} s^{-1}, respectively. The data recording rates are all 10 s^{-1}. These results of these tensile tests are shown in Figure 4.19-4.22.

Figure 4.19 is the load-displacement curves under tensile tests at strain rate 10^{-4} s^{-1} of Kapton foil, and 3.6 μm-thick nanocrystalline Mo thin film on Kapton foil. The curve of Mo is calculated according to Equation (1-3). The maximum load and elongation of 3.6 μm-thick nanocrystalline Mo thin film at strain rate 10^{-4} s^{-1} are 0.49 kgf and 2.3 mm, respectively. Figure 4.21 is tested under the same condition, but strain rate is 10^{-3} s^{-1}. The maximum load and elongation of 3.6 μm-thick nanocrystalline Mo thin film strain rate 10^{-3} s^{-1} are 0.48 kgf and 3.0 mm, respectively. Based on Figures 4.19 and 4.21, there are strain rate effects in Kapton foils but not in Mo thin films. Figures 4.20 and 4.22 are the stress-strain curves of nanocrystalline Mo thin films under tensile tests at strain rate 10^{-4} s^{-1} and 10^{-3} s^{-1}, respectively. According to Figures 4.20 and 4.22, the ultimate tensile strength is less than 500 MPa, and the elastic modulus is less than 5 GPa. Compared to Table 1.1, these values are much lower than Mo bulk materials.

These results of tensile tests of nanocrystalline Mo thin film on Kapton foils are incredible. We tried to find the reason why this phenomenon happened. The samples after tensile tests are shown in Figures 4.23 and 4.24. It is apparently to see that the films are stripped away during tensile tests. Based on Figure 4.4, we suggest that the morphology results in this phenomenon.

4.7 Results of nanoindentaion tests

Mo thin films

The nanocrystalline Mo thin films on P-type (100) silicon wafers are tested by the MTS

XP nanoindenter system via CSM mode at strain rate 0.05 per second and indentation depth 200 nm. The load-displacement curve is shown in Figure 4.25. In Figure 4.25, the maximum depth is set on 200 nm, and the maximum load is 9.7 nm. The hardness (*H*) and Young's modulus (*E*) measured by nanoindentation test are 14.5 GPa and 287 GPa. Compare to Table 1.1, the value of *E* is a little lower than it of Mo bulk materials.

Zr thin films

In order to analyze the mechanical properties of the nanocrystalline Zr thin films on silicon wafers, the specimens are measured by indentation tests in this study. The average thickness of nanocrystalline Zr thin films on substrates is 2.1 μm. The stress from indenter tip is conducted on the specimens by at room temperature. The specimens are indented via CSM mode. The indentation depth and strain rate are 300 nm and 0.05 per second, respectively. The load-displacement curves of these tests are shown in Figures 4.26.

Figure 4.26 is tested under CSM mode. All the curves are recorded by MTS XP nanoindenter system. In Figure 4.24, the values of maximum load of specimens RT, 100, 200, 300 and 400 are 11.8 mN, 10.6 mN, 11.0 mN, 11.3 mN and 13.9 mN, respectively.

According to Equations (2-5), (2-6), (2-7), (2-14), and (2-15), the hardness (*H*) and Young's modulus (*E*) of specimens can be analyzed by all the data recorded by MTS XP nanoindenter system. The values computed are listed in Table 4.2. In Table 4.2, the values of *H* and *E* of specimens are similar except specimen 400. Based on Table 4.1, there should be no obvious grain growth in specimens RT, 100, 200, and 300. Nonetheless, it is evident that the values of *H* and *E* of specimen 400 are much higher than those of other specimens.

Kutty et al. [85] studied the hot hardness of Zr and its alloys for nuclear reactors. They used Zr metal whose microstructure is equiaxed grains with 25 μm in diameter, and derived the relationship between hardness and temperature.

$$H = 232.91 - 0.35T + 1.07 \times 10^{-4} T^2 + 2.19 \times 10^{-8} T^3, \qquad (4\text{-}2)$$

where H is hardness in kg/mm^2, and T is temperature in K. According to Equation (4-2), we estimate the hardness of Zr metal with grain size 25 μm is 1.38 GPa at room temperature. Based on TEM observation and nanoindentation tests, the relationship between hardness and grain sizes is shown in Figure 4.27. In Figure 4.27, it seems that the inverse Hall-Petch behavior occurs in nanocrystalline Zr thin films. After considering the values of E of Zr thin film deposited at 400 °C in Table 4.2, we suggest that the sample may be oxidized. The other samples are in the range of nanocrystalline materials as shown in Figure 1.1. The slope k is smaller than that in the range of coarse-grained materials.

4.8 TEM observation after indentation tests

Zr thin films

After indentation tests, the samples are observed by JEOL 3010 AEM. The samples of cross section at indentation point are made by FIB system. The bright field images are shown in Figures 4.28-4.32. These samples are severely deformed, and there are lots of defects, such as stacking faults and twins, in these samples.

Chapter 5 Conclusions

In this study, the mechanical properties of nanocrystalline Mo and Zr thin films are examined. These specimens deposited at various temperatures were investigated by X-ray diffractormeter as well as TEM and tested by nanoindentation. The average grain sizes were estimated by XRD patterns and TEM images. The hardness and Young's modulus of nanocrystalline Mo and Zr thin films are estimated by nanoindentation tests, and the effect of deposition temperature on grain growth of nanocrystalline Zr thin films is examined. The conclusions are summarized below:

(1) We suggest that there are thermal shocks happening in these samples because of the rapid heating rate and the thickness of the thin films. The thermal stresses are in the samples, and get more and more. Furthermore, when the thermal stresses are large enough, the thin films get tripped away from the substrates due to the cracks caused by the tresses in the samples.

(2) Defects of materials will affect mechanical properties of materials, especially in tensile tests. They have more influence on mechanical properties during tensile tests than during compression tests.

(3) The average grain sizes estimated by XRD patterns are in common with those estimated by TEM images. The peak broadening of XRD patterns caused by grain size is so large that we can ignore the other factors, such as residual stress and X-ray machine, which can cause peak broadening.

(4) The grain grows larger in Zr thin films annealed, but the more thermal stresses make the films stripped away from the substrates.

(5) The critical deposition temperature with appreciable grain growth in nanocrystalline Zr thin films is estimated to be at least over 300 °C. There should be no evident

grain growth below this temperature.

(6) According to the mechanical properties of nanocrystalline Zr thin films determined by nanoindentation tests, the slope k is quite small than that in the range of coarse-grained materials.

References

1. R. Birringer, H. Gleiter, H. P. Klein and P. Marquardt, Physics Letters A **102**, 365-369 (1984).
2. K. S. Kumar, H. Van Swygenhoven and S. Suresh, Acta Materialia **51**, 5743-5774 (2003).
3. M. Chen, E. Ma and K. Hemker, *Mechanical Behavior of Nanocrystalline Metals*, in *Nanomaterials Handbook*, CRC/Taylor & Francis. p. 497-531 (2006).
4. E. O. Hall, Proceedings of the Physical Society. Section B 747-753 (1951).
5. N. J. Petch, J. Iron and Steel Institute **174**, 25-28 (1953).
6. A. A. W. Thompson, Acta Metallurgica **23**, 1337-1342 (1975).
7. C. A. Schuh, T. G. Nieh and T. Yamasaki, Scripta Materialia **46**, 735-740 (2002).
8. D. H. Jeong, U. Erb, K. T. Aust and G. Palumbo, Scripta Materialia **48**, 1067-1072 (2003).
9. C. A. Schuh, T. G. Nieh and H. Iwasaki, Acta Materialia **51**, 431-443 (2003).
10. J. Carsley, A. Fisher, W. Milligan and E. Aifantis, Metallurgical and Materials Transactions A **29**, 2261-2271 (1998).
11. D. Jia, K. T. Ramesh and E. Ma, Acta Materialia **51**, 3495-3509 (2003).
12. Q. Wei, D. Jia, K. T. Ramesh and E. Ma, Applied Physics Letters **81**, 1240-1242 (2002).
13. Q. Wei, T. Jiao, K. T. Ramesh and E. Ma, Scripta Materialia **50**, 359-364 (2004).
14. Q. Wei, K. Ramesh, B. Schuster, L. Kecskes and R. Dowding, JOM Journal of the Minerals, Metals and Materials Society **58**, 40-44 (2006).
15. O. D. Sherby and J. Wadsworth, Progress in Materials Science **33**, 169-221 (1989).
16. Q. Wei, S. Cheng, K. T. Ramesh and E. Ma, Materials Science and Engineering A

381, 71-79 (2004).

17. R. Schwaiger, B. Moser, M. Dao, N. Chollacoop and S. Suresh, Acta Materialia **51**, 5159-5172 (2003).
18. C. Briant, JOM Journal of the Minerals, Metals and Materials Society **52**, 36-36 (2000).
19. J. Shields and P. Lipetzky, JOM Journal of the Minerals, Metals and Materials Society **52**, 37-39 (2000).
20. A. Baudry and et al., Journal of Physics: Condensed Matter **12**, 3719 (2000).
21. L. Smardz, Journal of Alloys and Compounds **395**, 17-22 (2005).
22. M. C. Liu, J. C. Huang, H. S. Chou, Y. H. Lai, C. J. Lee and T. G. Nieh, Scripta Materialia **61**, 840-843 (2009).
23. E. J. Rapperport, Acta Metallurgica **7**, 254-260 (1959).
24. I. J. Beyerlein and C. N. TomÈ, International Journal of Plasticity **24**, 867-895 (2008).
25. A. H. Chokshi, A. Rosen, J. Karch and H. Gleiter, Scripta Metallurgica **23**, 1679-1683 (1989).
26. U. Erb, Nanostructured Materials **6**, 533-538 (1995).
27. F. Ebrahimi, Q. Zhai and D. Kong, Scripta Materialia **39**, 315-321 (1998).
28. F. Ebrahimi, G. R. Bourne, M. S. Kelly and T. E. Matthews, Nanostructured Materials **11**, 343-350 (1999).
29. F. Dalla Torre, H. Van Swygenhoven and M. Victoria, Acta Materialia **50**, 3957-3970 (2002).
30. K. S. Kumar, S. Suresh, M. F. Chisholm, J. A. Horton and P. Wang, Acta Materialia **51**, 387-405 (2003).
31. F. Macionczyk and W. Bruckner, Journal of Applied Physics **86**, 4922 (1999).
32. D. Y. W. Yu and F. Spaepen, Journal of Applied Physics **95**, 2991-2997 (2004).

33. T. Li, Z. Y. Huang, Z. C. Xi, S. P. Lacour, S. Wagner and Z. Suo, Mechanics of Materials **37**, 261-273 (2005).

34. X. Yong, L. Teng, S. Zhigang and J. J. Vlassak, Applied Physics Letters **87**, 161910 (2005).

35. T. Li and Z. Suo, International Journal of Solids and Structures **43**, 2351-2363 (2006).

36. T. Li and Z. Suo, International Journal of Solids and Structures **44**, 1696-1705 (2007).

37. S. Cheng, E. Ma, Y. M. Wang, L. J. Kecskes, K. M. Youssef, C. C. Koch, U. P. Trociewitz and K. Han, Acta Materialia **53**, 1521-1533 (2005).

38. R. K. Guduru, K. L. Murty, K. M. Youssef, R. O. Scattergood and C. C. Koch, Materials Science and Engineering: A **463**, 14-21 (2007).

39. A. M. El-Sherik, U. Erb, G. Palumbo and K. T. Aust, Scripta Metallurgica et Materialia **27**, 1185-1188 (1992).

40. U. Erb. *Electrodiposited Nanocrystals - Synthesis, Structure, Properties and Future Applications*: Pergamon-Elsevier Science Ltd (1995).

41. P. G. Sanders, J. A. Eastman and J. R. Weertman, Acta Materialia **45**, 4019-4025 (1997).

42. P. G. Sanders, G. E. Fougere, L. J. Thompson, J. A. Eastman and J. R. Weertman, Nanostructured Materials **8**, 243-252 (1997).

43. R. C. Hugo, H. Kung, J. R. Weertman, R. Mitra, J. A. Knapp and D. M. Follstaedt, Acta Materialia **51**, 1937-1943 (2003).

44. H. Gleiter, Progress in Materials Science **33**, 223-315 (1989).

45. B. Chapman, *Glow Discharge Processes: Sputtering and Plasma Etching*, John Wiley & Sons (1980).

46. K. Seshan, *Handbook of thin-film deposition processes and techniques: principles, methods, equipment, and applications*. Park Ridge, N.J., Noyes Publications (2002).

47. R. Ondo-Ndong, F. Pascal-Delannoy, A. Boyer, A. Giani and A. Foucaran, Materials Science and Engineering B **97**, 68-73 (2003).

48. D. M. Mattox, *Handbook of physical vapor deposition (PVD) processing*. Westwood, N.J., Noyes Publications (1998).

49. J. A. Thornton, *Physical Vapor Deposition*, in *Semiconductor Materials and Process Technology Handbook for Very Large Scale Integration (VLSI) and Ultra Large Scale Integration (ULSI)*, Park Ridge, N.J., Noyes Publications. p. 329-454 (1988).

50. K. Wasa and S. Hayakawa, *Handbook of Sputter Deposition Technology*. Park Ridge, N.J., Noyes Publications (1992).

51. B. A. Movchan and A. V. Demchish, Physics of Metals and Metallography **28**, 83-90 (1969).

52. J. A. Thornton, Journal of Vacuum Science and Technology **11**, 666-670 (1974).

53. J. A. Thornton, Journal of Vacuum Science & Technology **12**, 830-835 (1975).

54. R. F. Bunshah, *Handbook of deposition technologies for films and coatings*. Park Ridge, N.J., Noyes Publications (1994).

55. Y. M. Wang, K. Wang, D. Pan, K. Lu, K. J. Hemker and E. Ma, Scripta Materialia **48**, 1581-1586 (2003).

56. L. Lu, S. X. Li and K. Lu, Scripta Materialia **45**, 1163-1169 (2001).

57. J. R. Weertman, *Mechanical Behavior of Nanocrystalline Metals*, in *Nanostructured Materials: Processing, Properties, and Potential Applications*, Norwich, William Andrew Publishing. p. 397–421 (2002).

58. R. A. Masumura, P. M. Hazzledine and C. S. Pande, Acta Materialia **46**, 4527-4534 (1998).

59. Y. M. Wang and E. Ma, Acta Materialia **52**, 1699-1709 (2004).

60. Y. Wang, M. Chen, F. Zhou and E. Ma, Nature **419**, 912 (2002).

61. A. Vinogradov and S. Hashimoto. *Fatigue of severely deformed metals*: Wiley-V C H Verlag Gmbh (2003).

62. M. Legros, K. J. Hemker, A. Gouldstone, S. Suresh, R. M. Keller-Flaig and E. Arzt, Acta Materialia **50**, 3435-3452 (2002).

63. Z. Budrovic, H. Van Swygenhoven, P. M. Derlet, S. Van Petegem and B. Schmitt, Science **304**, 273 (2004).

64. J. Schiotz, F. D. Di Tolla and K. W. Jacobsen, Nature **391**, 561 (1998).

65. J. Schiotz and K. W. Jacobsen, Science **301**, 1357 (2003).

66. H. Van Swygenhoven, Science **296**, 66 (2002).

67. Z. Shan, E. A. Stach, J. M. K. Wiezorek, J. A. Knapp, D. M. Follstaedt and S. X. Mao, Science **305**, 654 (2004).

68. J. R. Rice, Journal of the Mechanics and Physics of Solids **40**, 239-271 (1992).

69. P. Müllner, C. Solenthaler and M. O. Speidel, Acta Metallurgica et Materialia **42**, 1727-1732 (1994).

70. P. Müllner, C. Solenthaler and M. O. Speidel, in *Twinning in Advanced Materials*, Warrendale, PA, TMS. p. 483-490 (1994).

71. M. Chen, E. Ma, K. J. Hemker, H. Sheng, Y. Wang and X. Cheng, Science **300**, 1275-1277 (2003).

72. S. Timoshenko and J. N. Goodier, *Theory of Elasticity*. 2nd ed. New York, McGraw-Hill (1951).

73. I. N. Sneddon, International Journal of Engineering Science **3**, 47-57 (1965).

74. G. M. Pharr, W. C. Oliver and F. R. Brotzen, Journal of Materials Research **7**, 613-617 (1992).

75. W. C. Oliver and G. M. Pharr, Journal of Materials Research **19**, 3-20 (2004).

76. I. Manika and J. Maniks, Acta Materialia **54**, 2049-2056 (2006).

77. F. K. Mante, G. R. Baran and B. Lucas, Biomaterials **20**, 1051-1055 (1999).

78. M. B. Daia, P. Aubert, S. Labdi, C. Sant, F. A. Sadi, P. Houdy and J. L. Bozet, Journal of Applied Physics **87**, 7753-7757 (2000).

79. K. D. Bouzakis, N. Michailidis, S. Hadjiyiannis, G. Skordaris and G. Erkens, Materials Characterization **49**, 149-156 (2002).

80. M. Qasmi, P. Delobelle, F. Richard and A. Bosseboeuf, Surface and Coatings Technology **200**, 4185-4194 (2006).

81. A. Bolshakov and G. M. Pharr, Journal of Materials Research **13**, 1049-1058 (1998).

82. K. W. McElhaney, J. J. Vlassak and W. D. Nix, Journal of Materials Research **13**, 1300-1306 (1998).

83. K. Miyake, S. Fujisawa, A. Korenaga, T. Ishida and S. Sasaki, Japanese Journal of Applied Physics **43**, 4602-4605 (2004).

84. D. Rickerby and A. Matthews, *Advanced Surface Coatings: a Handbook of Surface Engineering*. Glasgow, Blackie & Son Limited (1991).

85. T. R. G. Kutty, K. Ravi and C. Ganguly, Journal of Nuclear Materials **265**, 91-99 (1999).

86. H. S. Huang, Ph. D Thesis, *The Effects of Processing Parameters and Additives on Sintering Behavior of Molybdenum and its Brittleness*, Department of Materials Science and Engineering, National Taiwan University, (2002).

87. H. G. Yang, Master Thesis, *Properties, Structures of Zr and ZrNx Thin Films and their Application for Diffusion Barrier by DC Magnetron Sputtering*, Department of Materials Science and Engineering, National Cheng Kung University, (2002).

88. DuPont™. www.dupont.com.

89. W. D. Nix, Materials Science and Engineering A **234-236**, 37-44 (1997).

Table 1.1 The fundamental data related to Mo bulk materials [86].

Melting point	2620 °C
Boiling point	5560 °C
Density	10.2 g/cm^3
Thermal expansion	5.5x10^{-6} K^{-1}
Electrical resistivity	48 nΩm
Young's modulus	320 GPa
Poisson ratio	0.293

Table 1.2 The fundamental data related to Zr bulk materials [87].

Melting point	1852 °C
Boiling point	4409 °C
Density	6.49 g/cm^3
Thermal expansion	5.9x10^{-6} K^{-1}
Electrical resistivity	440 nΩm
Young's modulus	89.8 GPa
Poisson ratio	0.34

Table 2.1 Zone structures in sputtered films [52].

Zone	T/T_m	Characteristics	Film properties
1	<0.1 at 0.15 Pa to <0.5 at 4 Pa	Voided boundaries, fibrous grains. Zone 1 is promoted by substrate roughness and oblique deposition.	Hard
T	0.1 to 0.4 at 0.15 Pa, ~0.4 to 0.5 at 4 Pa	Fibrous grains, dense grain boundary arrays.	High dislocation density, hard, high strength, low ductility.
2	0.4 to 0.7	Columnar grains, dense grain boundaries.	Hard, low ductility.
3	0.6 to 1.0	Large equiaxed grains, bright surface.	Low dislocation density, soft recrystallized grains.

Table 3.1 Physical properties of Kapton® HPP-ST films [88].

Typical Properties of Kapton® HPP-ST at 23°C (73°F)

Property	Unit	1 mil 25µm	2 mil 50µm	3 mil 75µm	5 mil 125µm	Test Method
Physical						
Tensile Strength	kpsi (MPa)	34 (234)	34 (234)	34 (234)	34 (234)	ASTM D-882-91
Elongation	%	80	82	82	82	ASTM D-882-91
Tensile Modulus	kpsi (GPa)	400 (2.8)	400 (2.8)	400 (2.8)	400 (2.8)	ASTM D-882-91
Adhesion	pli (N/mm)	10 (1.8)	10 (1.8)	10 (1.8)	10 (1.8)	IPC-TM-650 Method 2.4.9*
Density	g/cc	1.42	1.42	1.42	1.42	ASTM D-1505-90
MIT Folding Endurance	cycles	285,000	55,000	6,000	3,000	ASTM D-2176-89
Tear Strength-propagating (Elmendorf), N		0.07	0.21	0.38	0.58	ASTM D-1922-89
Tear Strength, initial (Graves), N		7.2	16.3	26.3	46.9	ASTM D-1004-90
Thermal						
Flammability		94V0	94V0	94V0	94V0	UL-94
Shrinkage (30 min at 150°C)	%	0.03	0.03	0.03	0.03	IPC-TM-650 Method 2.2.4A
Limiting Oxygen Index	%	37	43	46	45	ASTM D-2863-87
Electrical						
Dielectric Strength	kV/mil (kV/mm)	7.7 (303)	6.1 (240)	5.2 (205)	3.9 (154)	ASTM D-149-91
Dielectric Constant	1kHz	3.4	3.4	3.5	3.5	ASTM D-150-92
Dissipation Factor at 1 kHz		0.0018	0.0020	0.0020	0.0026	ASTM D-150-92
Volume Resistivity	ohm-cm	1.5×10^{17}	1.5×10^{17}	1.4×10^{17}	1.0×10^{17}	ASTM D-257-91

*Acrylic adhesive to 1 oz. copper

Table 3.2 The details of the sputtering conditions in this study.

Target	Ti	Mo	Zr
Power	DC 150 W	DC 200 W	DC 200 W
Base pressure	10^{-5} torr	10^{-5} torr	10^{-5} torr
Ar	30 sccm 4 mtorr	10 sccm 1 mtorr	10 sccm 1 mtorr
Temperature	25 °C	25 °C	25 °C – 400 °C
Rotary	10 rpm	10 rpm	10 rpm
Deposition time	60 s	10800 s	8100 s

Table 4.1 The average grain size of Zr thin films deposited at various temperatures.

Sputter temperature	Average grain size (nm)	
	XRD	TEM
RT	17	20
100 °C	19	20
200 °C	16	22
300 °C	21	23
400 °C	27	30

Table 4.2 The hardness and Young's modulus of nanocrystalline Zr thin films.

Sputter temperature	E (GPa)	H (GPa)
RT	128	7.0
100 °C	127	6.5
200 °C	129	6.9
300 °C	129	7.0
400 °C	141	9.2

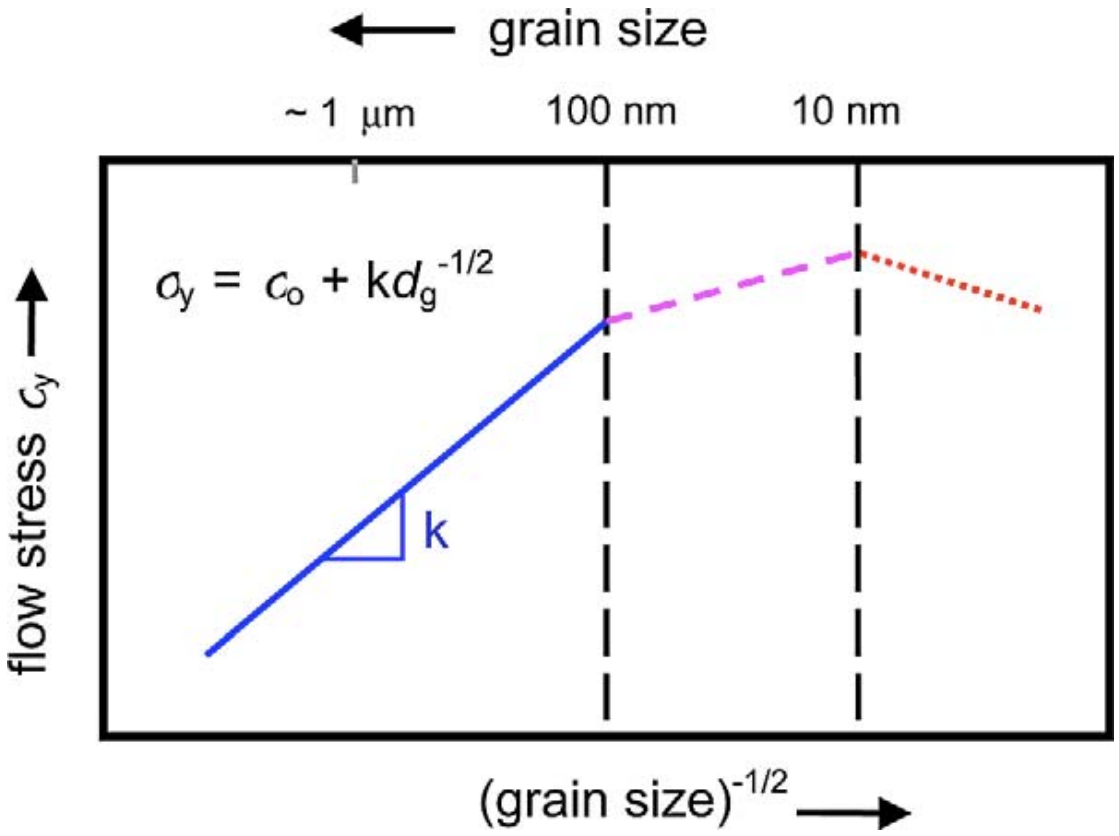

Figure 1.1 The variation of flow stress as a function of grain size in coarse-grained and nanocrystalline materials [2].

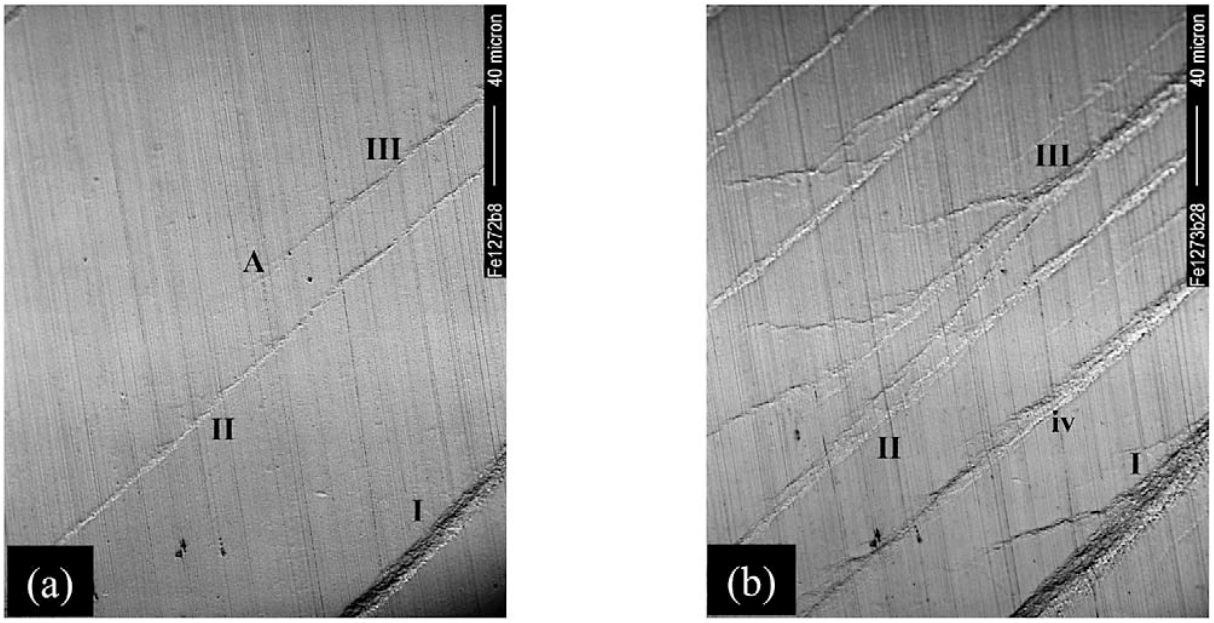

Figure 1.2 Evolution and development of shear bands in Fe with grain size 268 nm. Observations of shear bands at the same location but different strain level: (a) 3.7% (b) 7.8%. Loading axis is vertical [11].

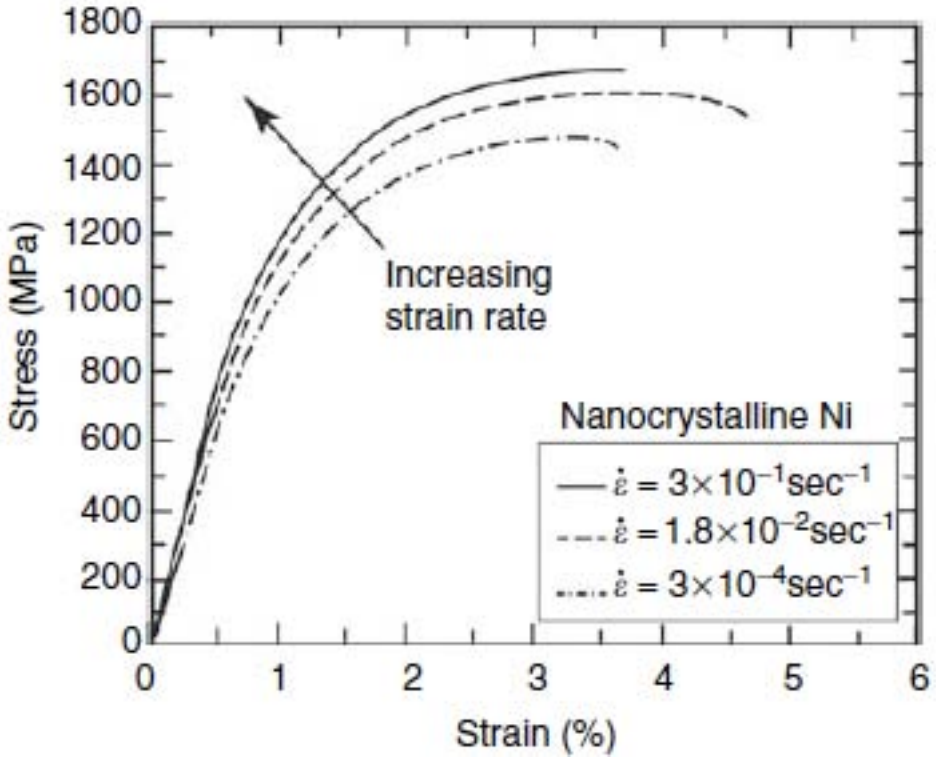

Figure 1.3 Engineering stress-strain curves of an electrodeposited nanocrystalline Ni with grain size of 40 nm by using tensile testing at different strain rates [17].

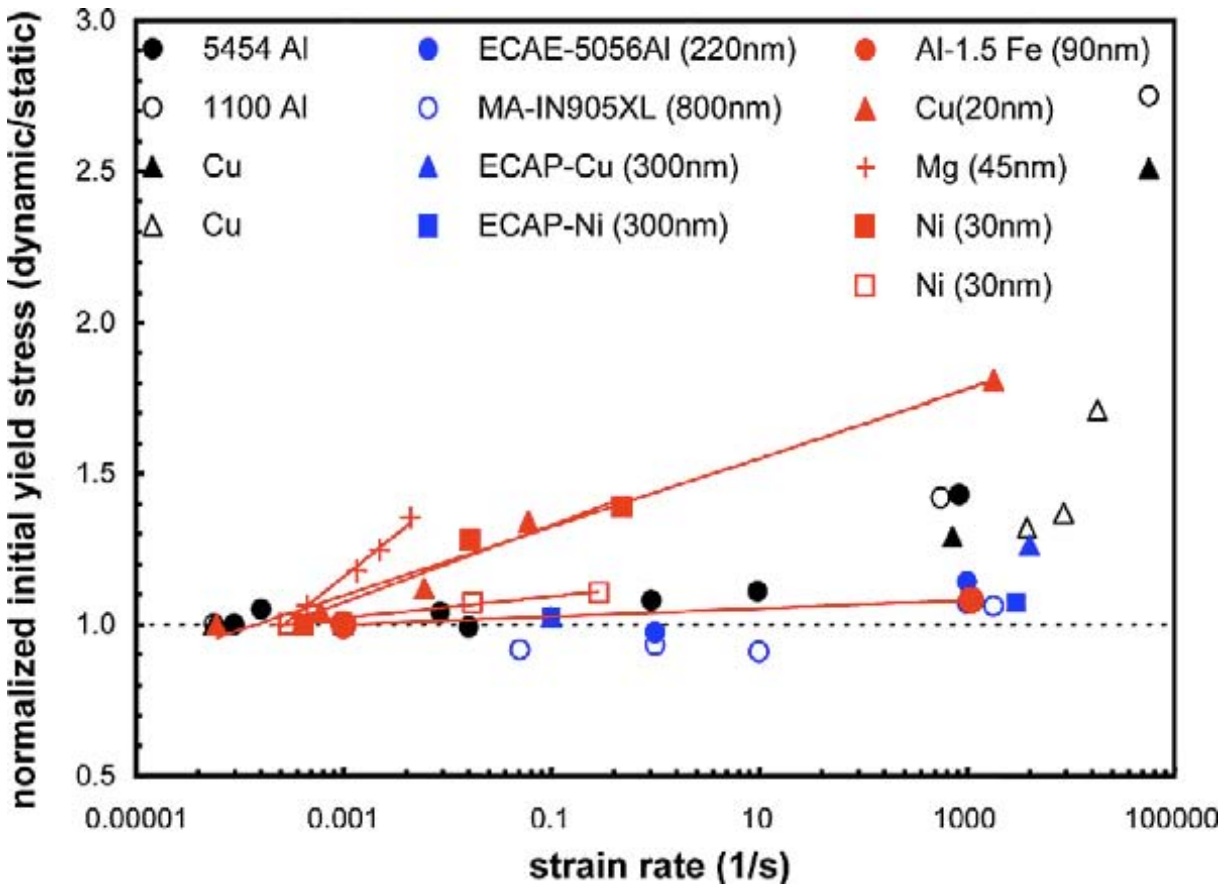

Figure 1.4 A summary of experimental results available in the literature on the effect of strain rate [2].

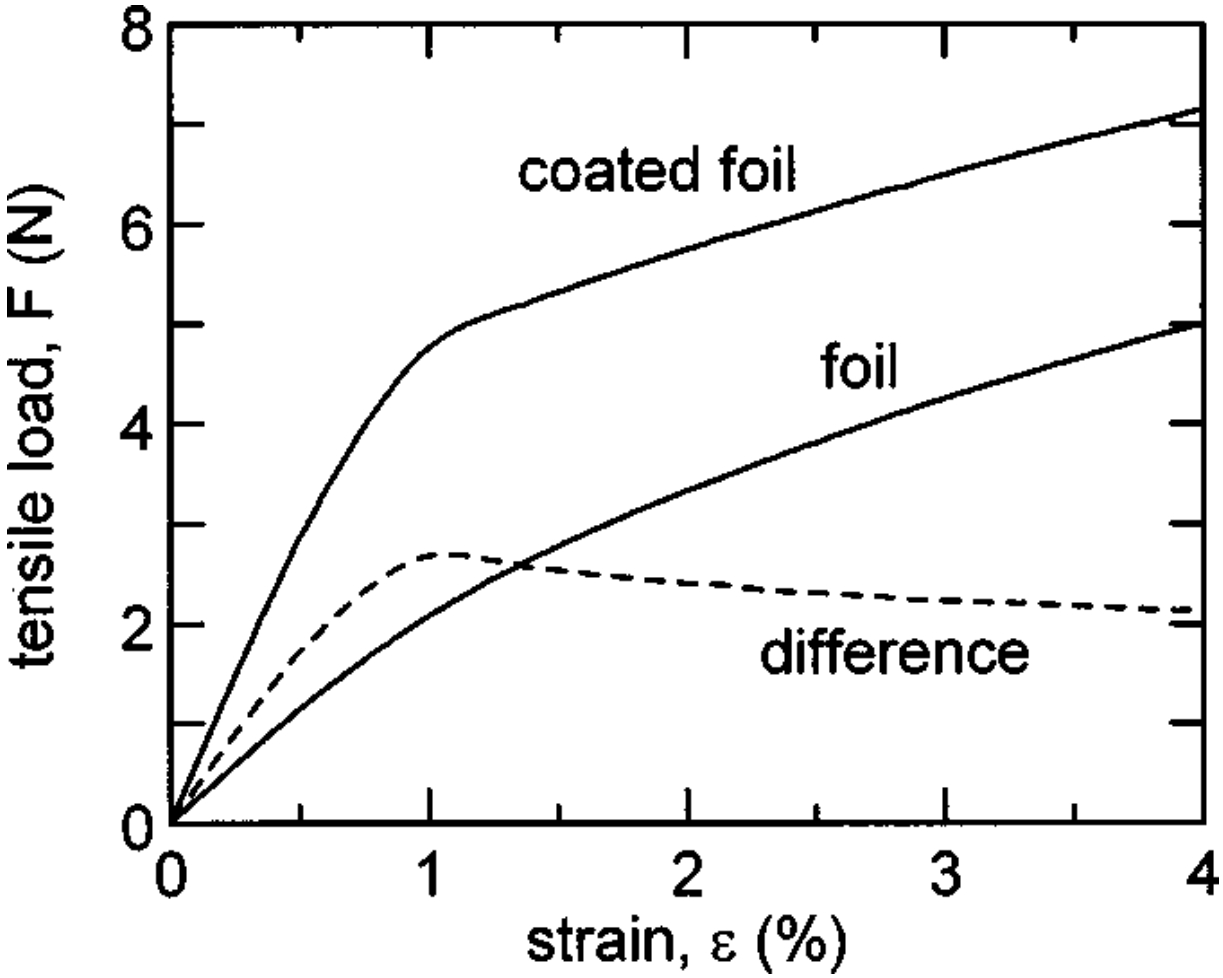

Figure 1.5 The scheme illustrating Equation (1-3) [31].

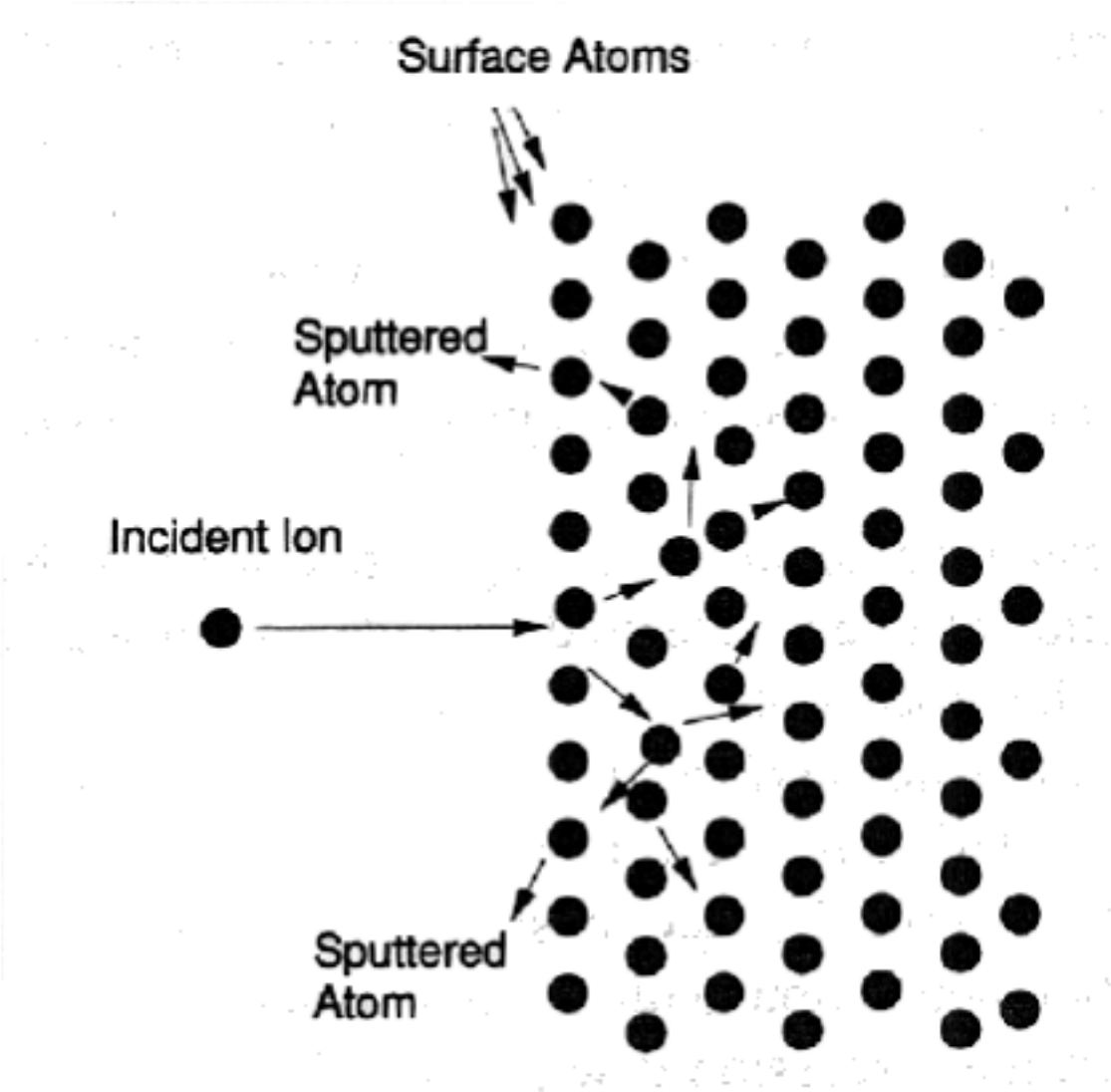

Figure 2.1 The scheme of physical sputtering process [46].

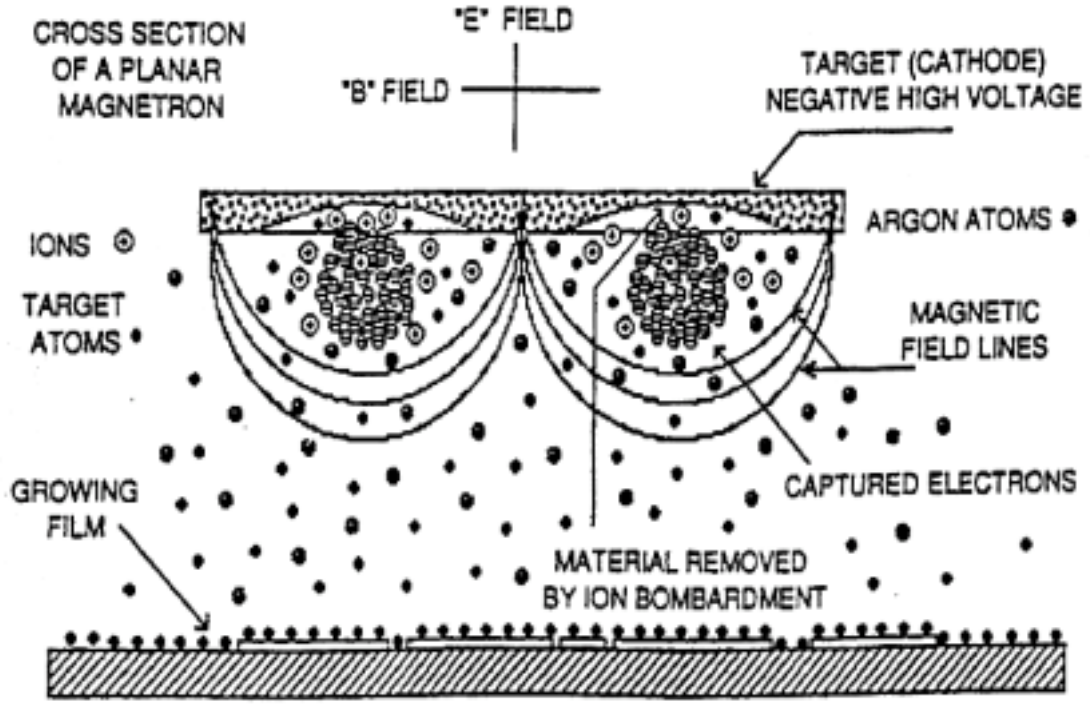

Figure 2.2 The scheme of magnetron sputtering [46].

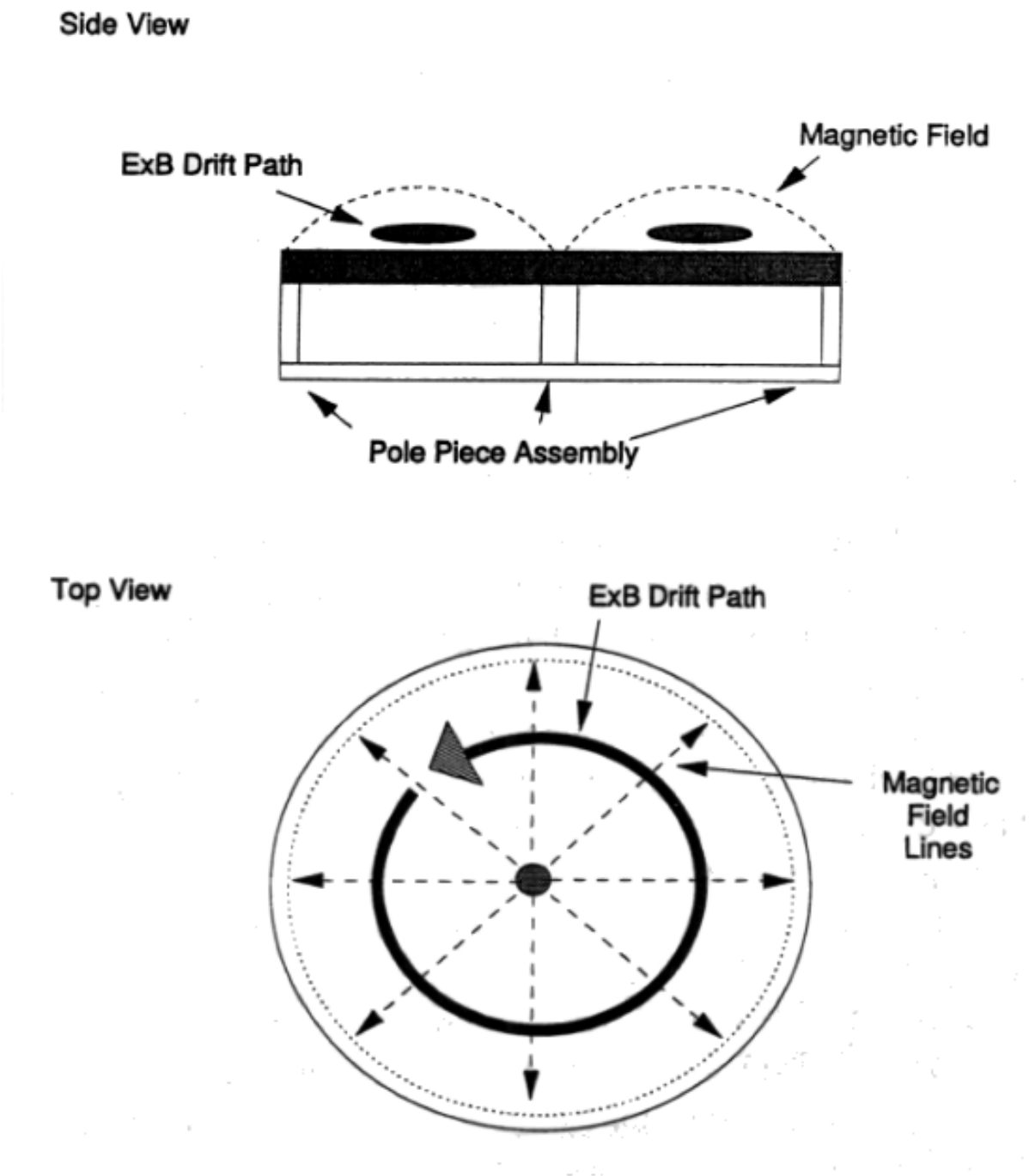

Figure 2.3 The magnetic field configuration for a circular planar magnetron cathode [46].

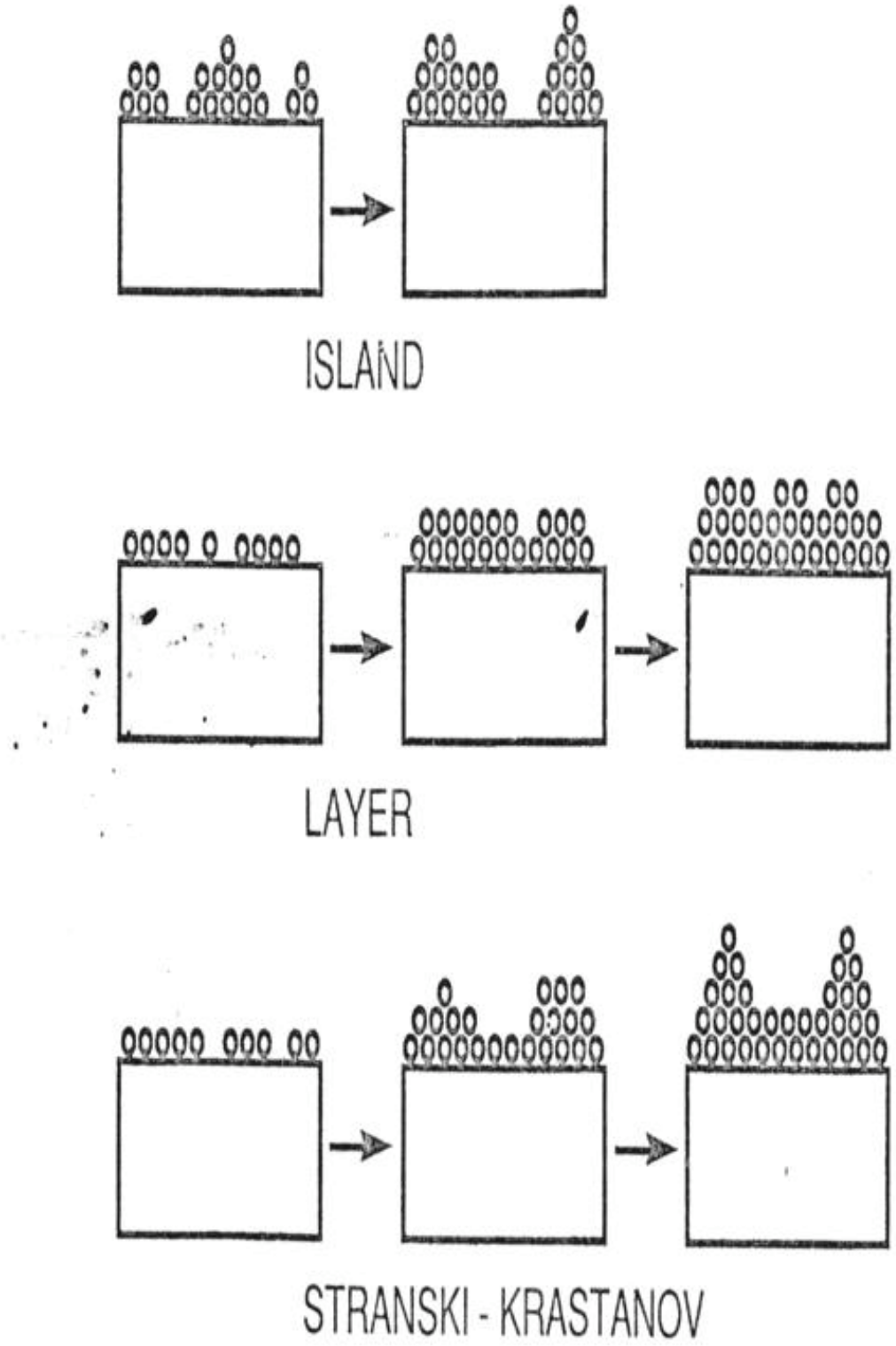

Figure 2.4 Film growth mode (a) Volmer-Weber, (b) Frank-Vander Merwe and (c) Stranki-Kratanov [50].

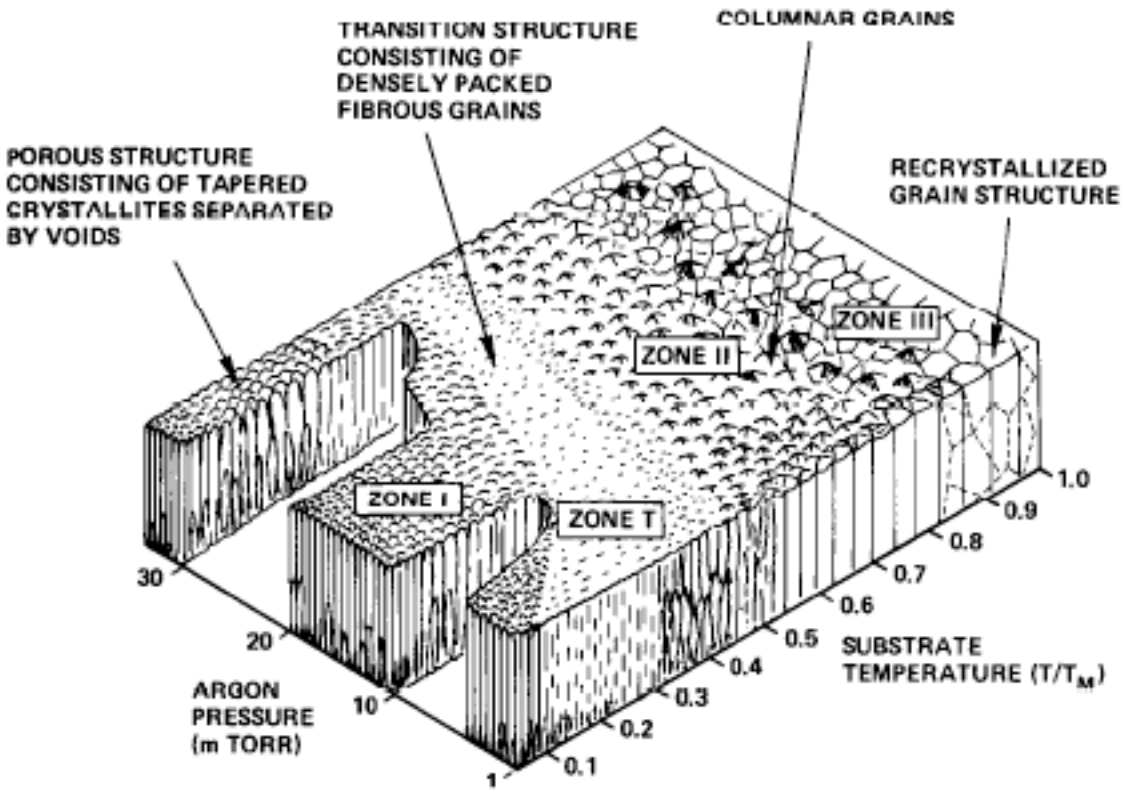

Figure 2.5 Thornton zone diagram. Experimental study of sputtering reveals repeatable microstructural trends-improved material quality with higher temperature and lower chamber gas pressure [52].

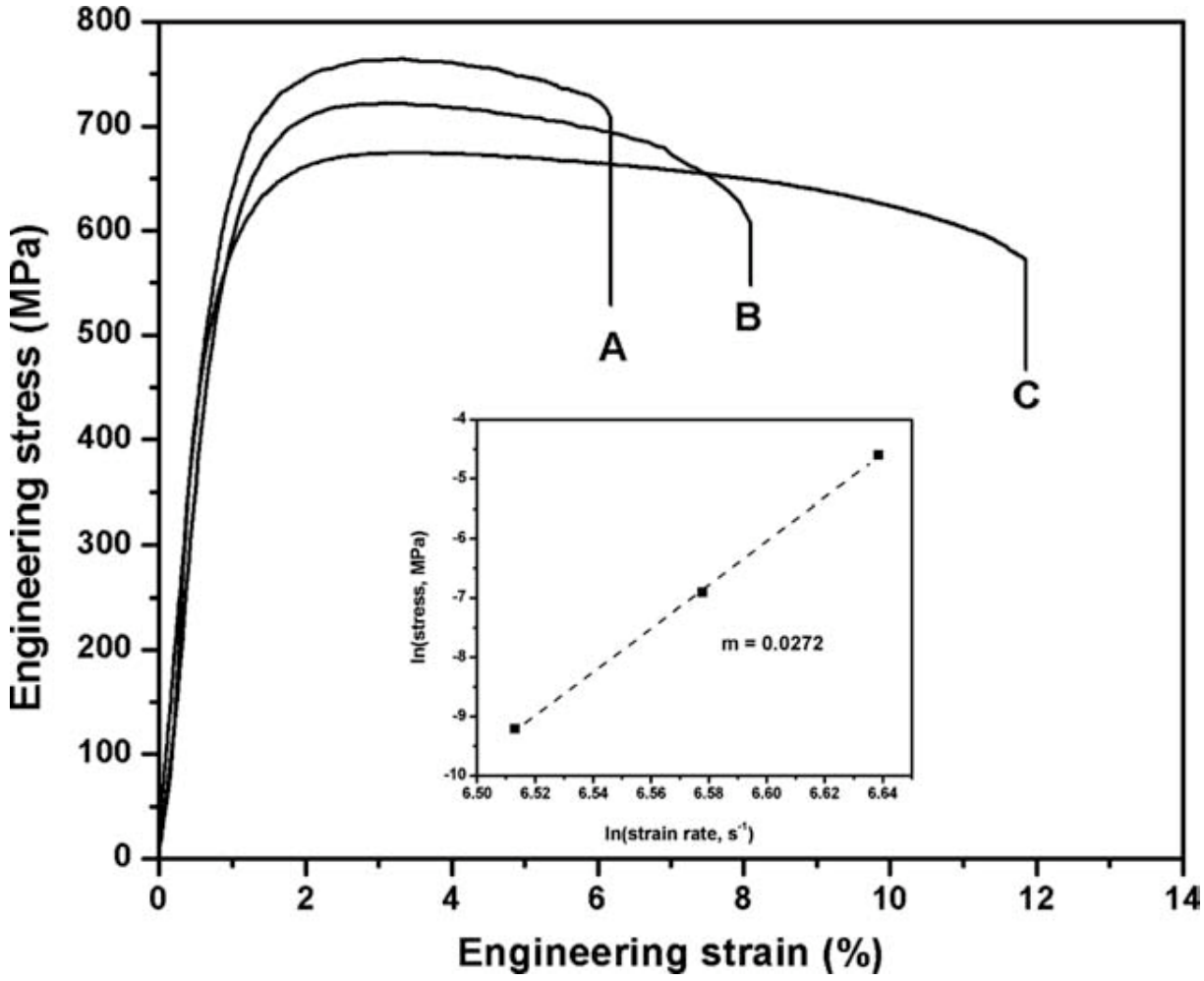

Figure 2.6 Tensile test of nanocrystlline Cu with average grain size of 62 nm at room temperature under different strain rate: (A) $\dot{\varepsilon}=10^{-2}$ s^{-1}; (B) $\dot{\varepsilon}=10^{-3}$ s^{-1}; (C) $\dot{\varepsilon}=10^{-4}$ s^{-1}. The strain rate sensitivity, *m*, is 0.0272 [37].

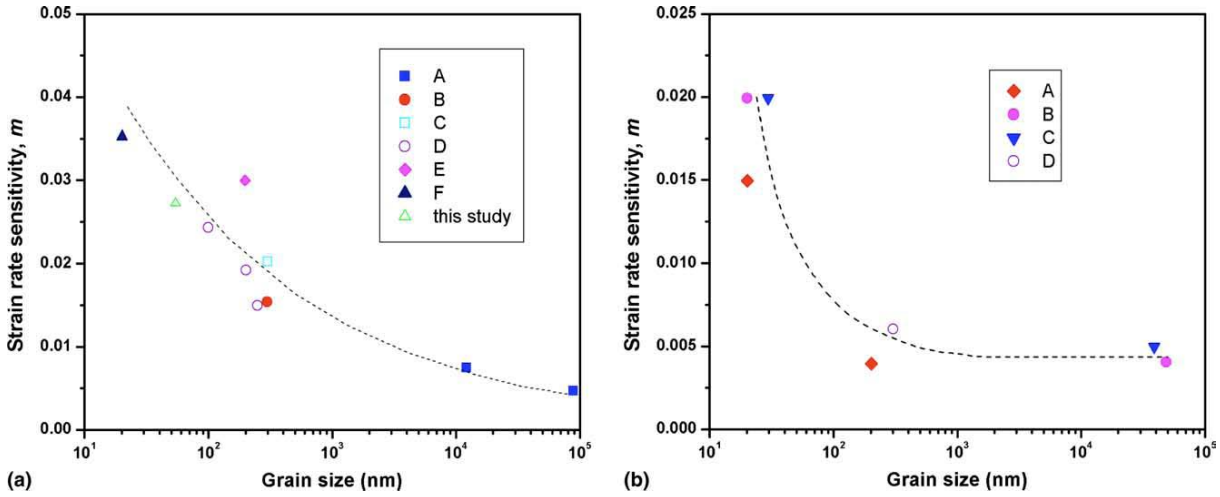

Figure 2.7 Summary of strain rate sensitivity m vs. grain size d for (a) Cu and (b) Ni [37].

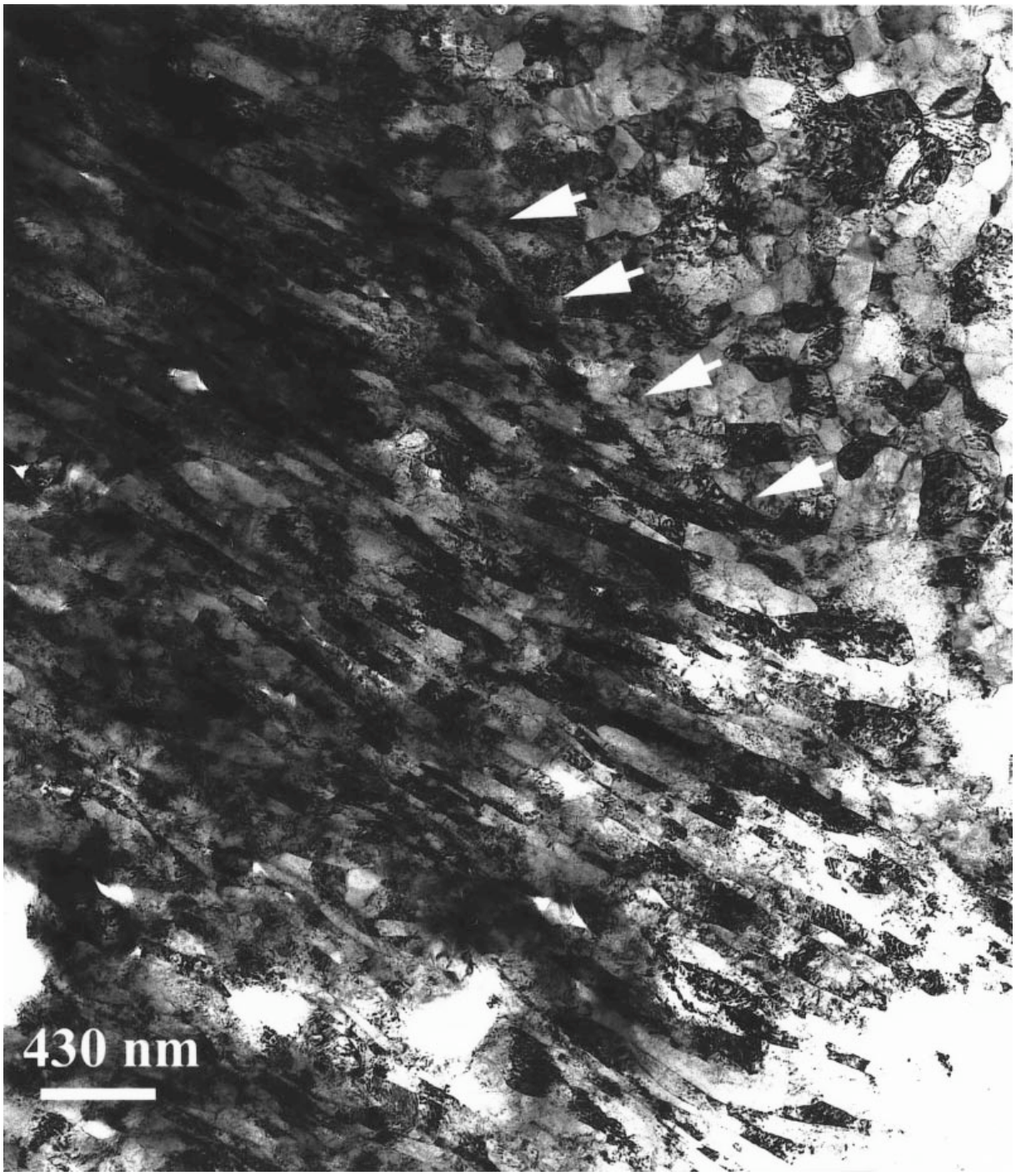

Figure 2.8 Bright field TEM image showing a shear band marked by arrows and the uniform microstructure outside the band [12].

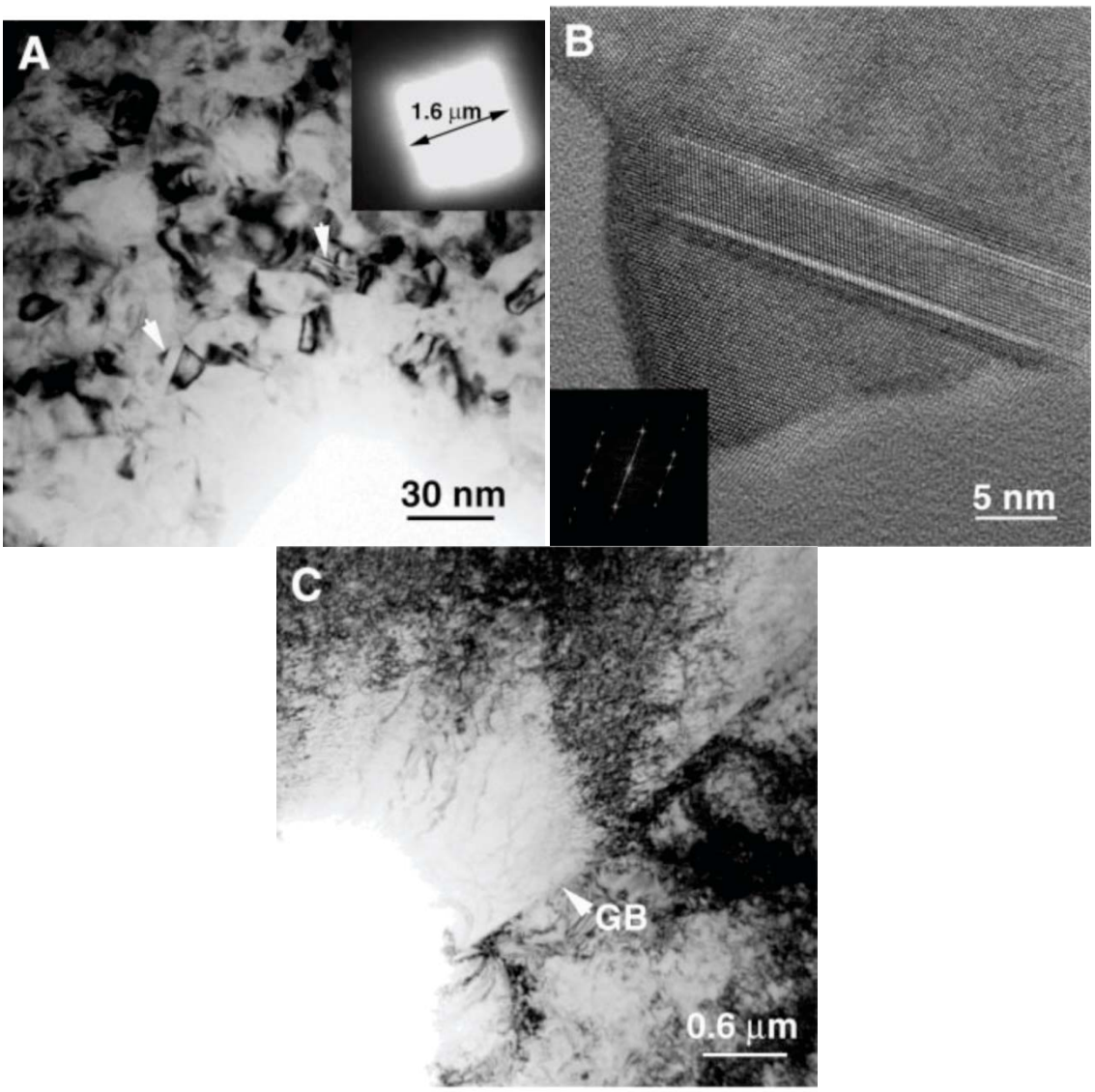

Figure 2.9 (A) TEM micrograph of deformation twins around an indent in nanocrystalline Al. The inset shows the indent with the fourfold geometry. (B) HRTEM micrograph showing a deformation twin in (A) with parallel boundaries. (C) Dislocations with a grain boundary around an indent in coarse-grained pure Al and no evidence of deformation twinning [71].

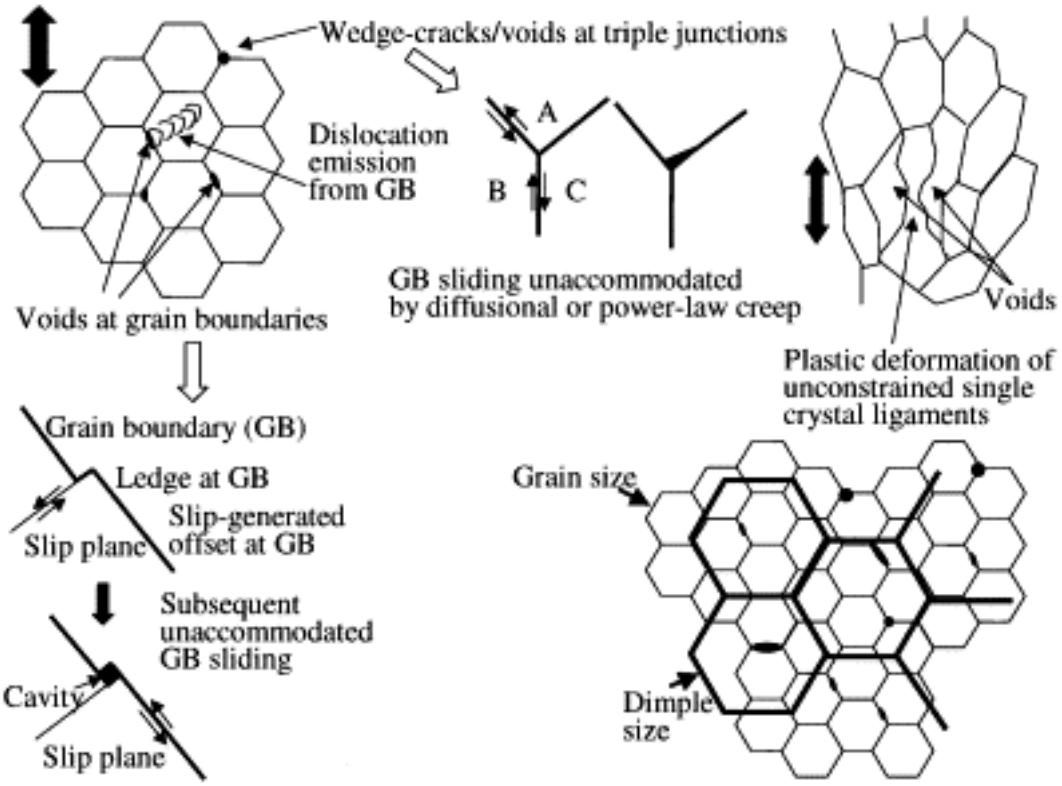

Figure 2.10 A schematic illustration depicting the deformation evolution process in the nanocrystalline Ni. Dislocation motion, void formation and growth at grain boundaries and triple junctions, the formation of partially unconstrained ligaments that deform plastically, and the interaction of these various features to produce the eventual fracture morphology are all synthesized in this figure [30].

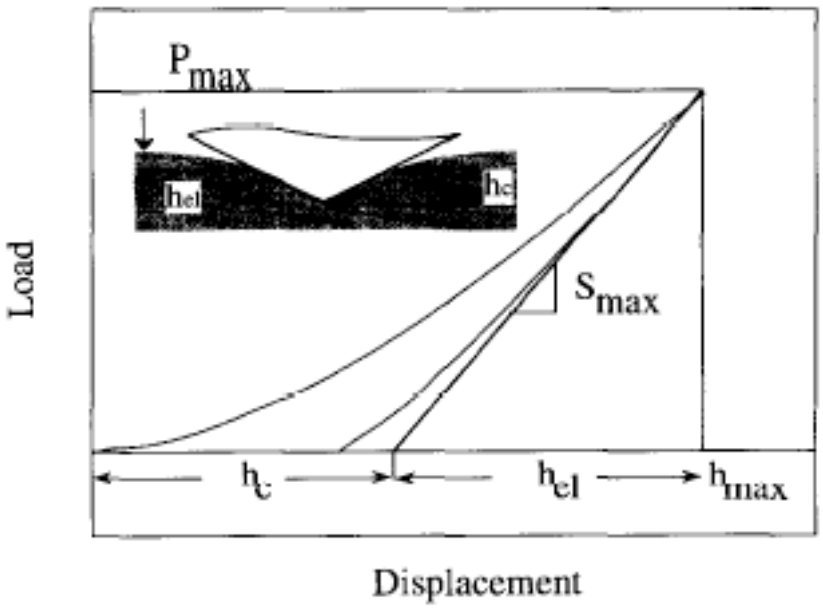

Figure 2.11 The curve of load versus displacement [89], where h_c, h_{el}, and h_{max} are displacement of contact, elastic deformation, and maximum respectively. P_{max}, and S_{max} are the maximum load and contact stiffness respectively.

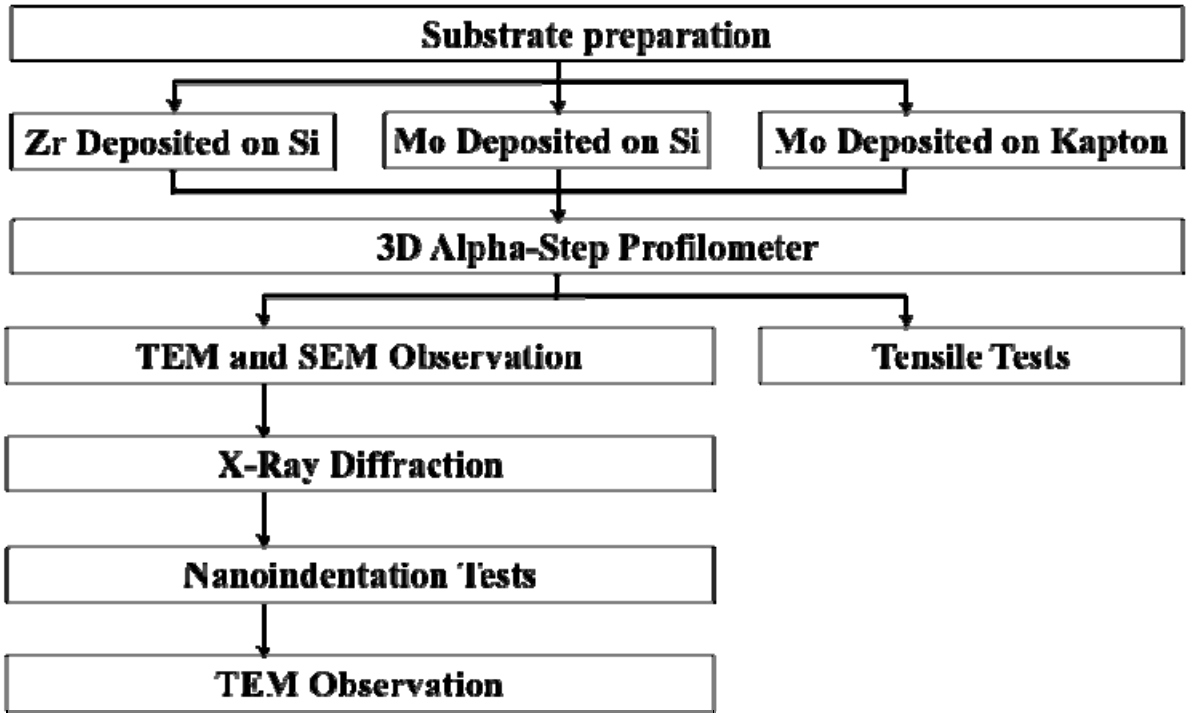

Figure 3.1 The flow chart of the experimental procedures.

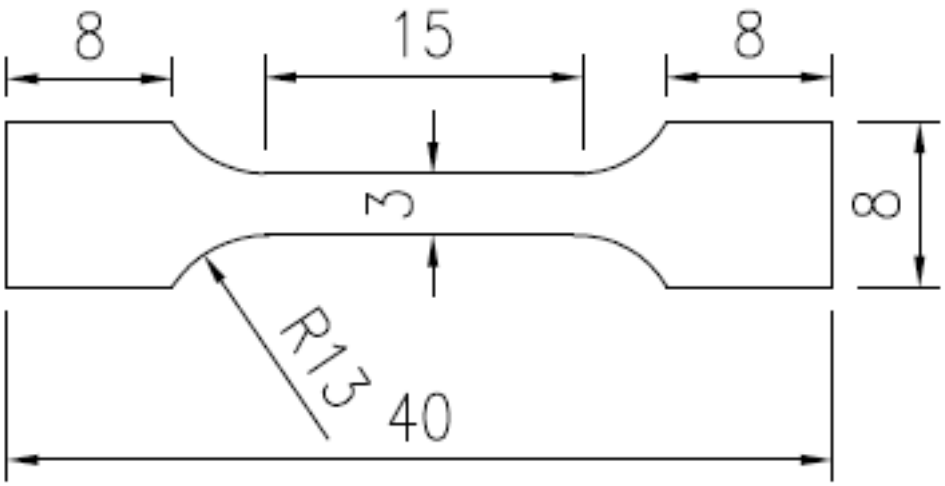

Figure 3.2 The geometry and dimension of the dog-bone-shape Kapton® HPP-ST foils. The thickness is 175 μm.

Figure 3.3 The multi-target magnetron sputtering system used in this study.

Figure 3.4 The Veeco Dektak 150 Stylus profiler 3D alpha-step profilometer used in this study.

Figure 3.5 The appearance of dual focus ion beam system (FIB, SEIKO SMI3050).

Figure 3.6 The MTS XP nanoindenter system and the computer used in this study.

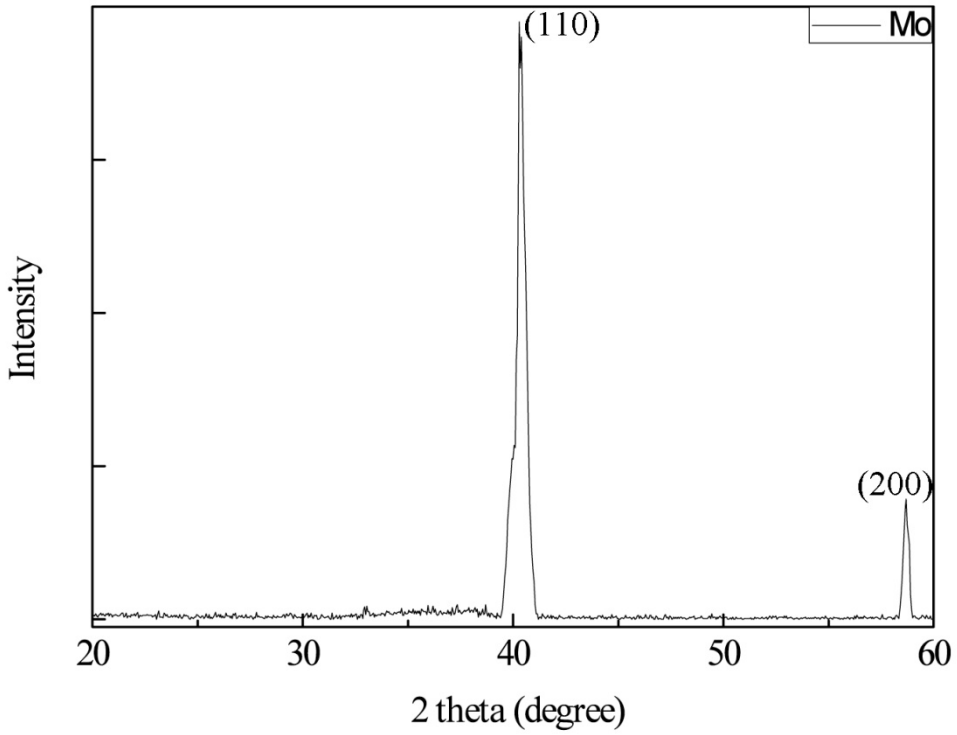

Figure 4.1 The X-ray diffraction pattern, scanned from 20° to 60°, of nanocrystalline Mo thin films.

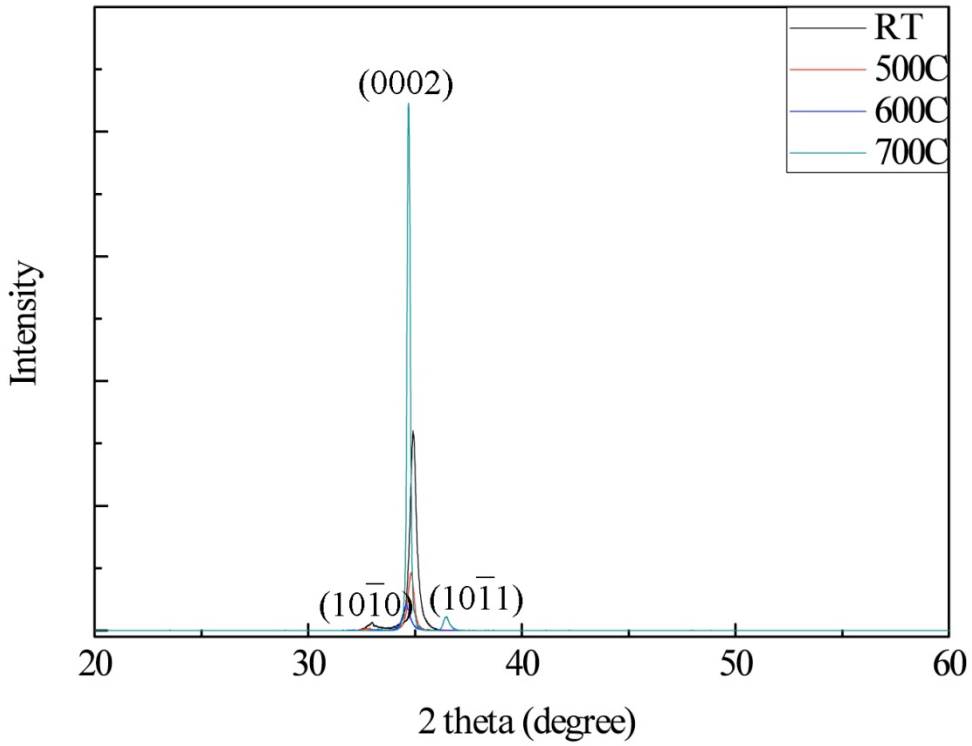

Figure 4.2 The X-ray diffraction pattern, scanned from 20° to 60°, of nanocrystalline Zr thin films annealed at different temperatures.

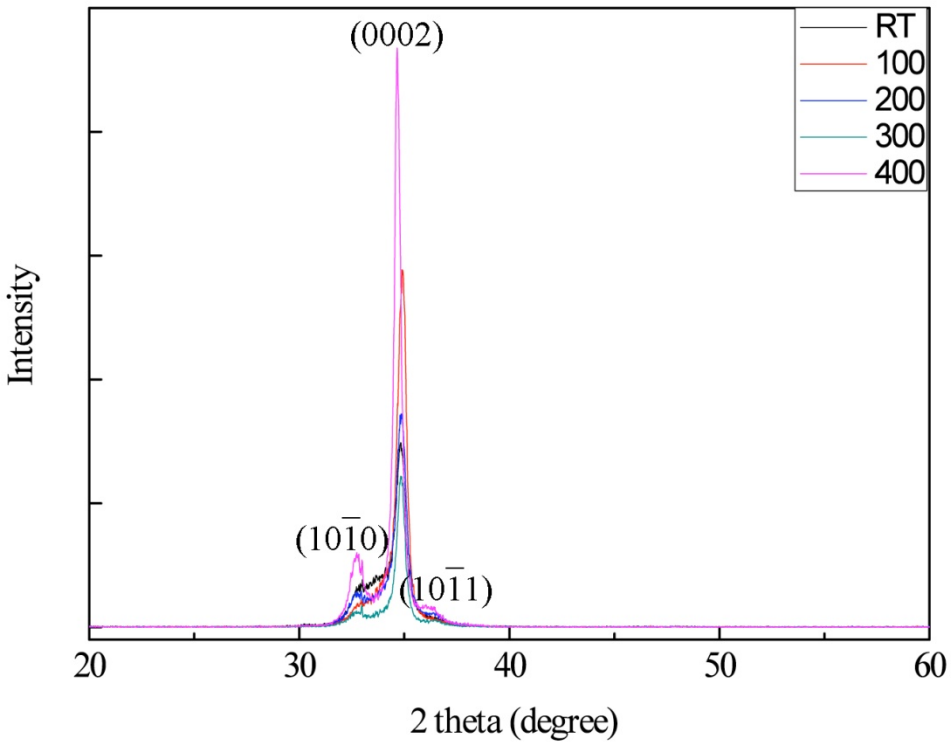

Figure 4.3 The X-ray diffraction pattern, scanned from 20° to 60°, of nanocrystalline Zr thin films deposited at different temperatures.

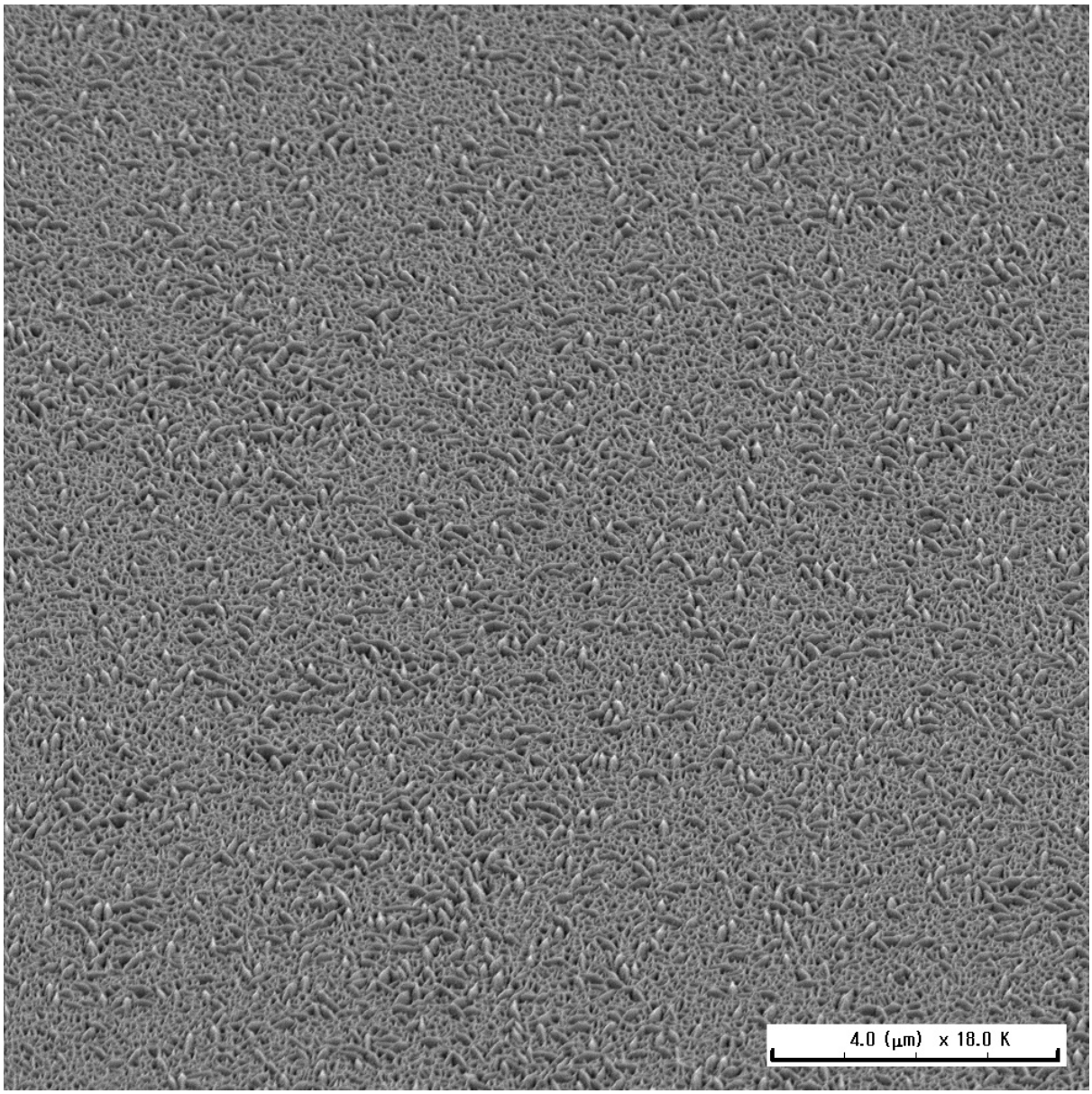

Figure 4.4 The surface of nanocrystalline Mo thin film on Si wafer.

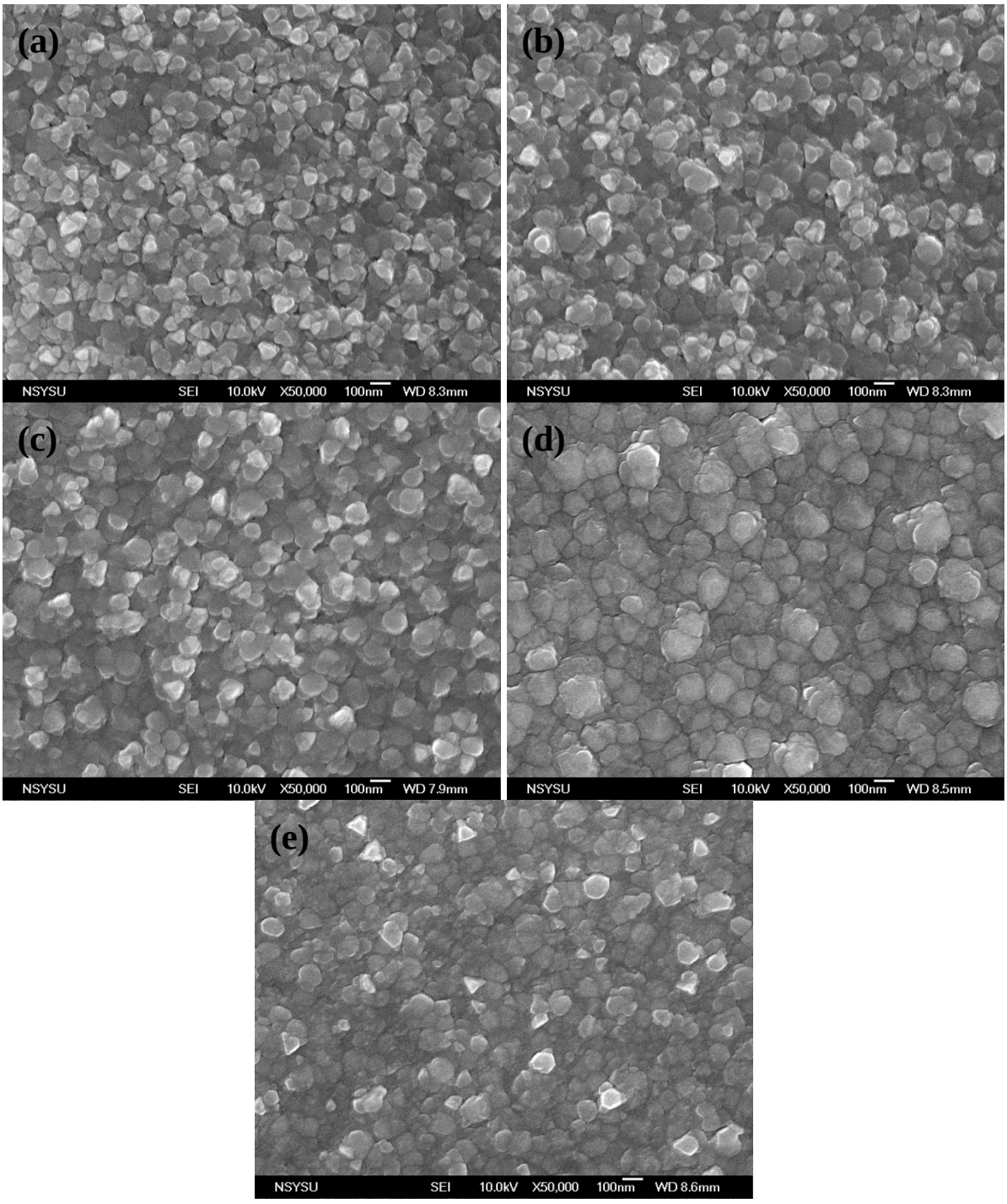

Figure 4.5 The surface of nanocrystalline Zr thin film deposited at various temperatures. (a) room temperature (b) 100 °C (c) 200 °C (d) 300 °C (e) 400 °C.

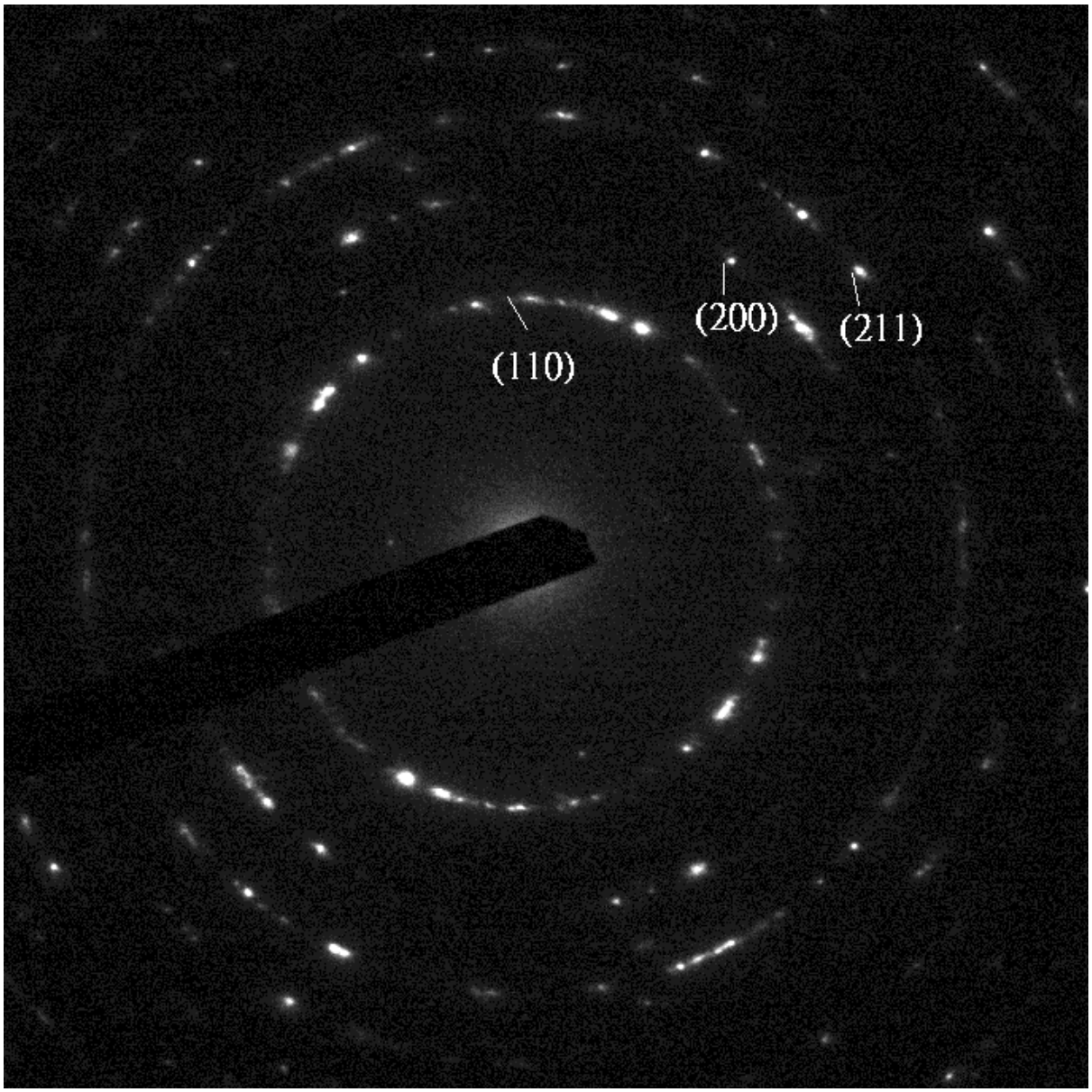

Figure 4.6 The SADP of nanocrystalline Mo thin film.

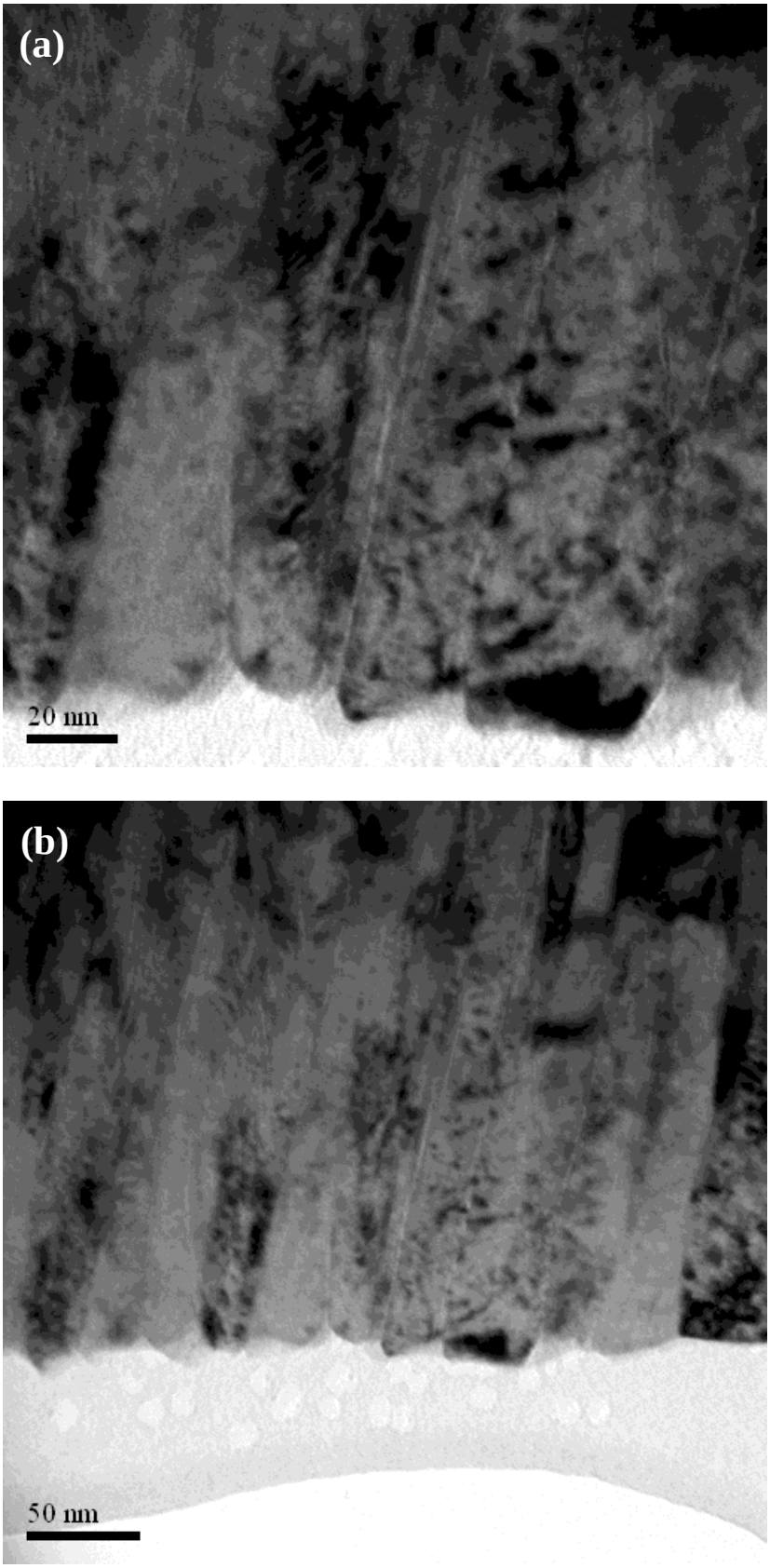

Figure 4.7 The bright field images of nanocrystalline Mo thin film at various magnifications.

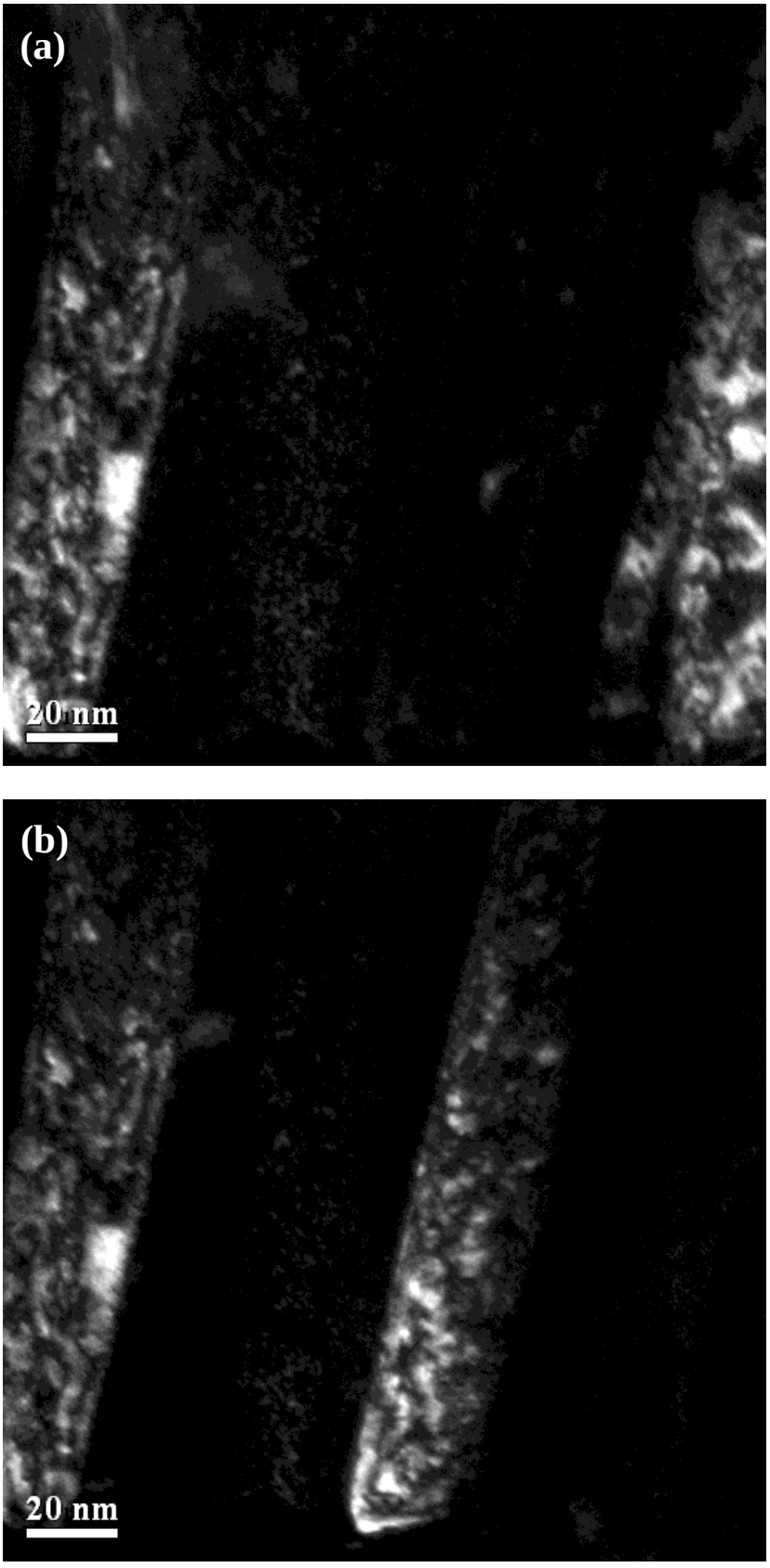

Figure 4.8 The dark field images of nanocrystalline Mo thin film using different diffraction beams.

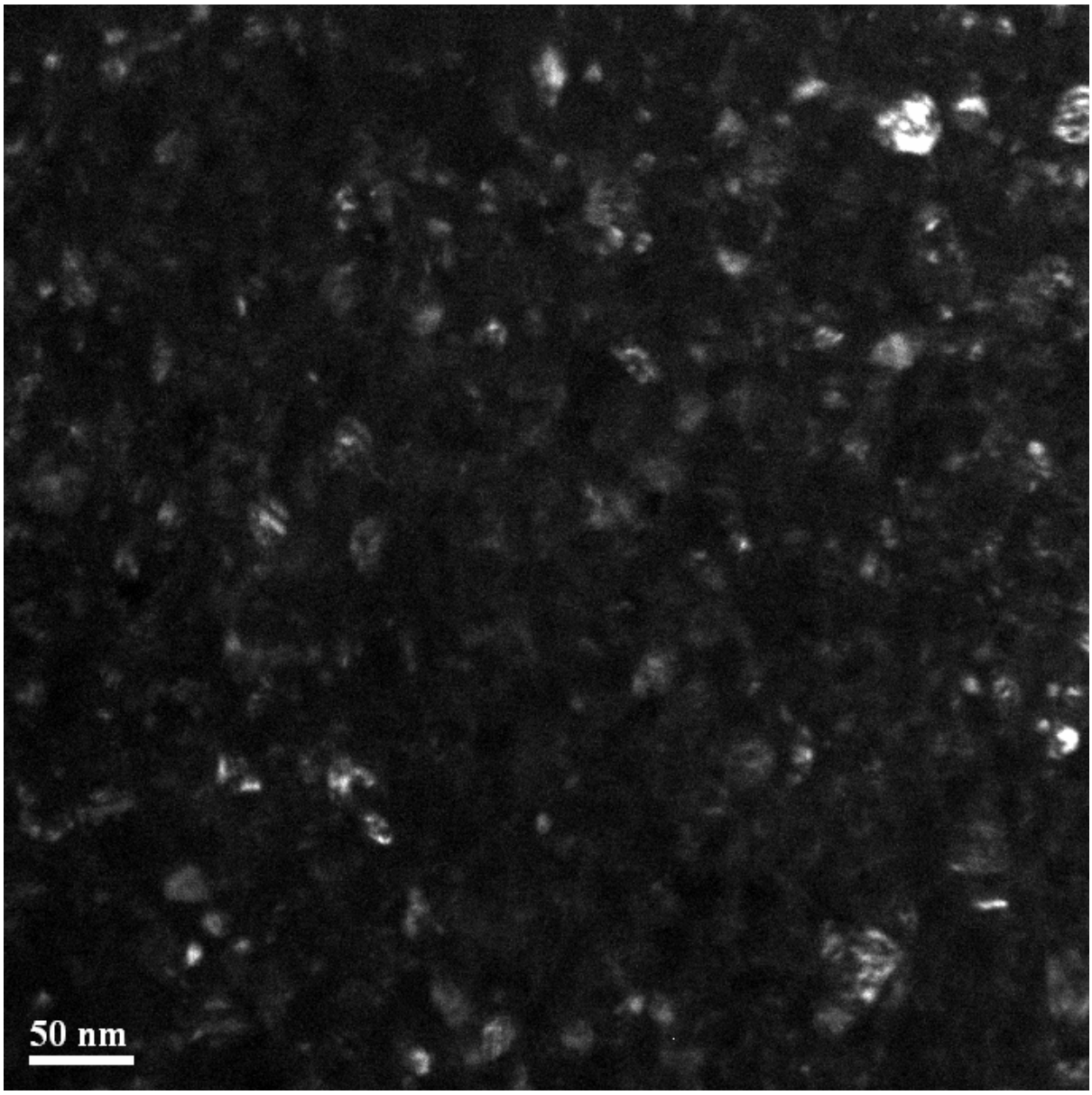

Figure 4.9 The dark field image of nanocrystalline Zr thin film deposited at room temperature.

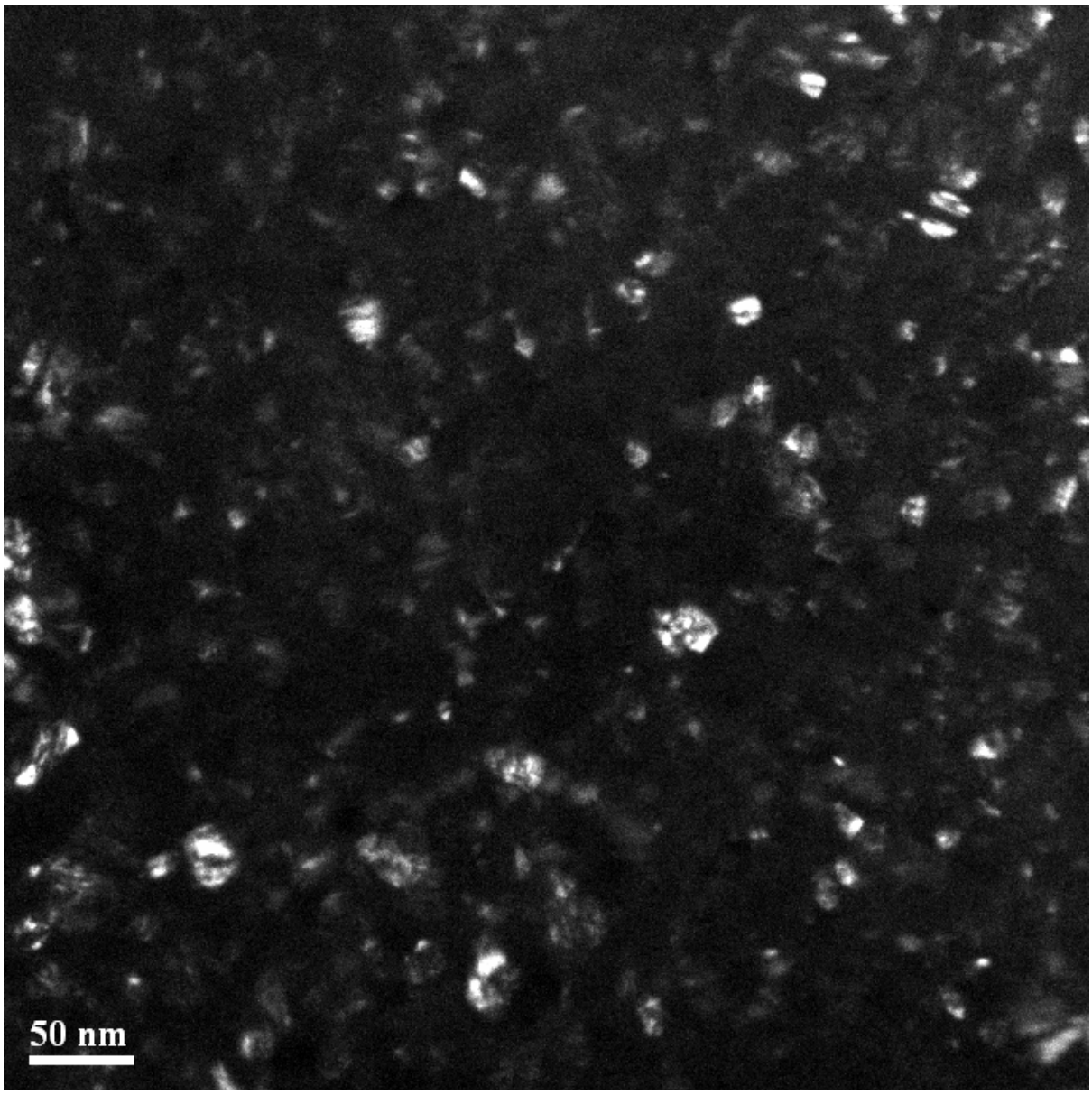

Figure 4.10 The dark field image of nanocrystalline Zr thin film deposited at 100 °C.

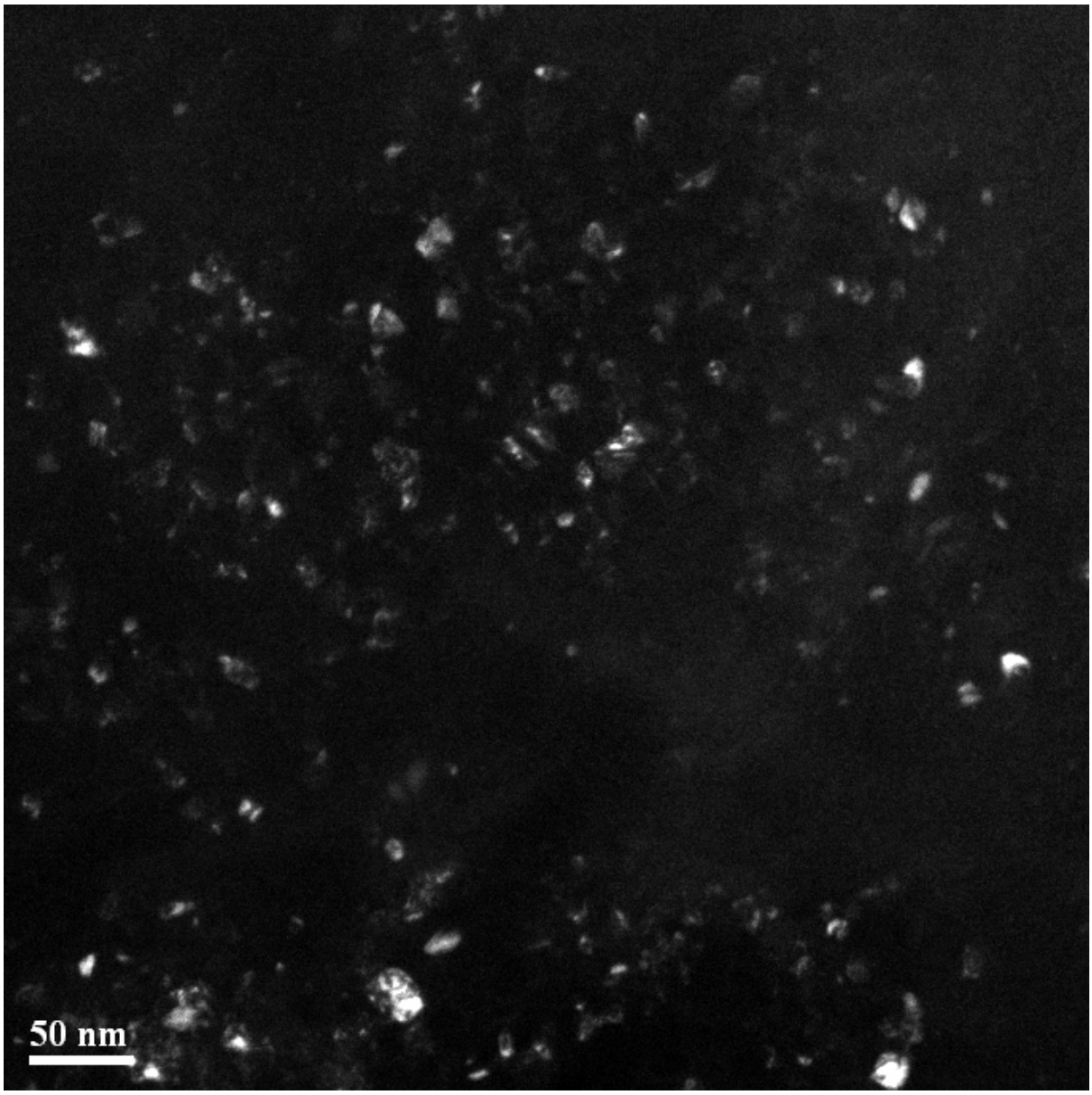

Figure 4.11 The dark field image of nanocrystalline Zr thin film deposited at 200 °C.

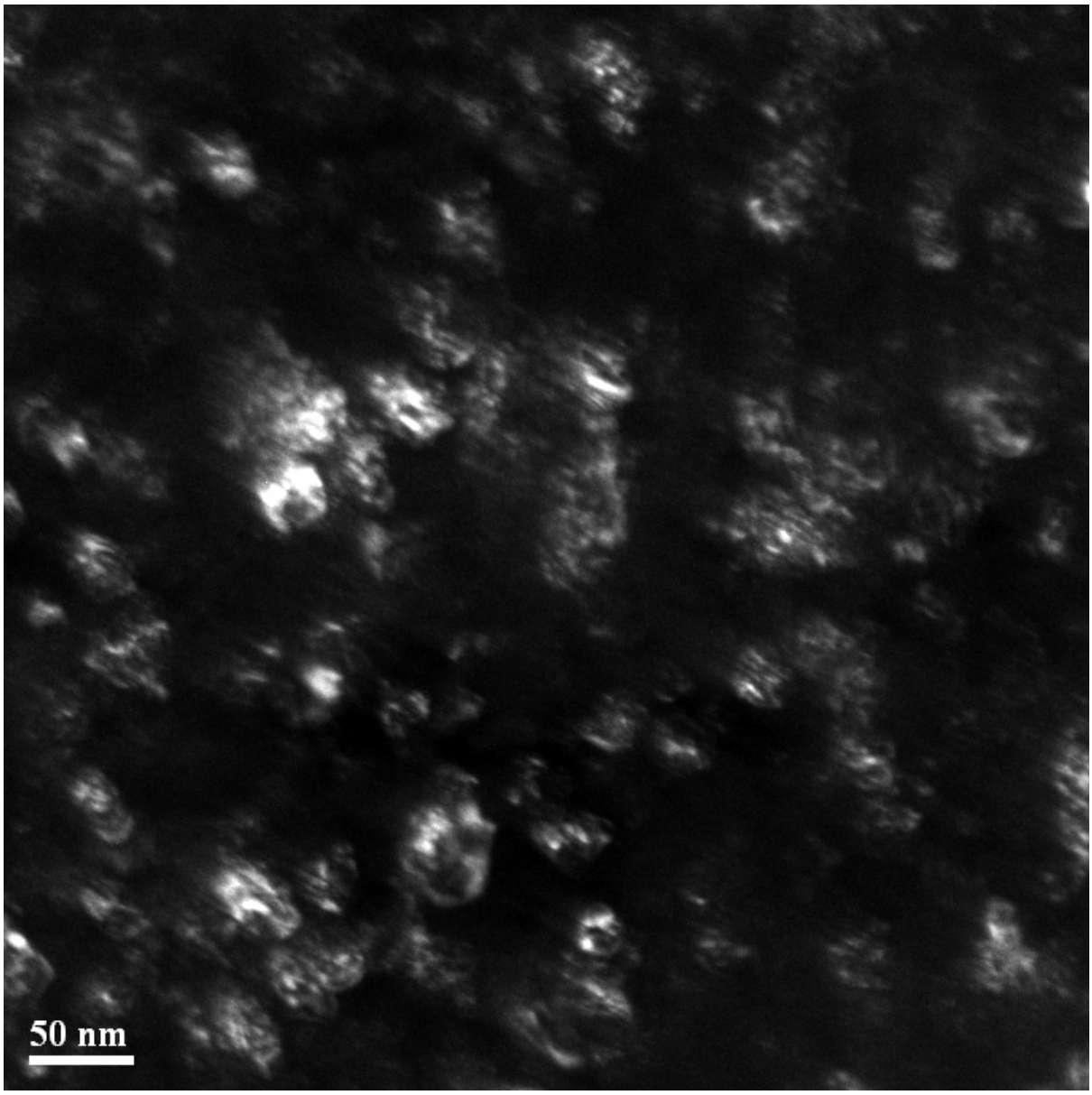

Figure 4.12 The dark field image of nanocrystalline Zr thin film deposited at 300 °C.

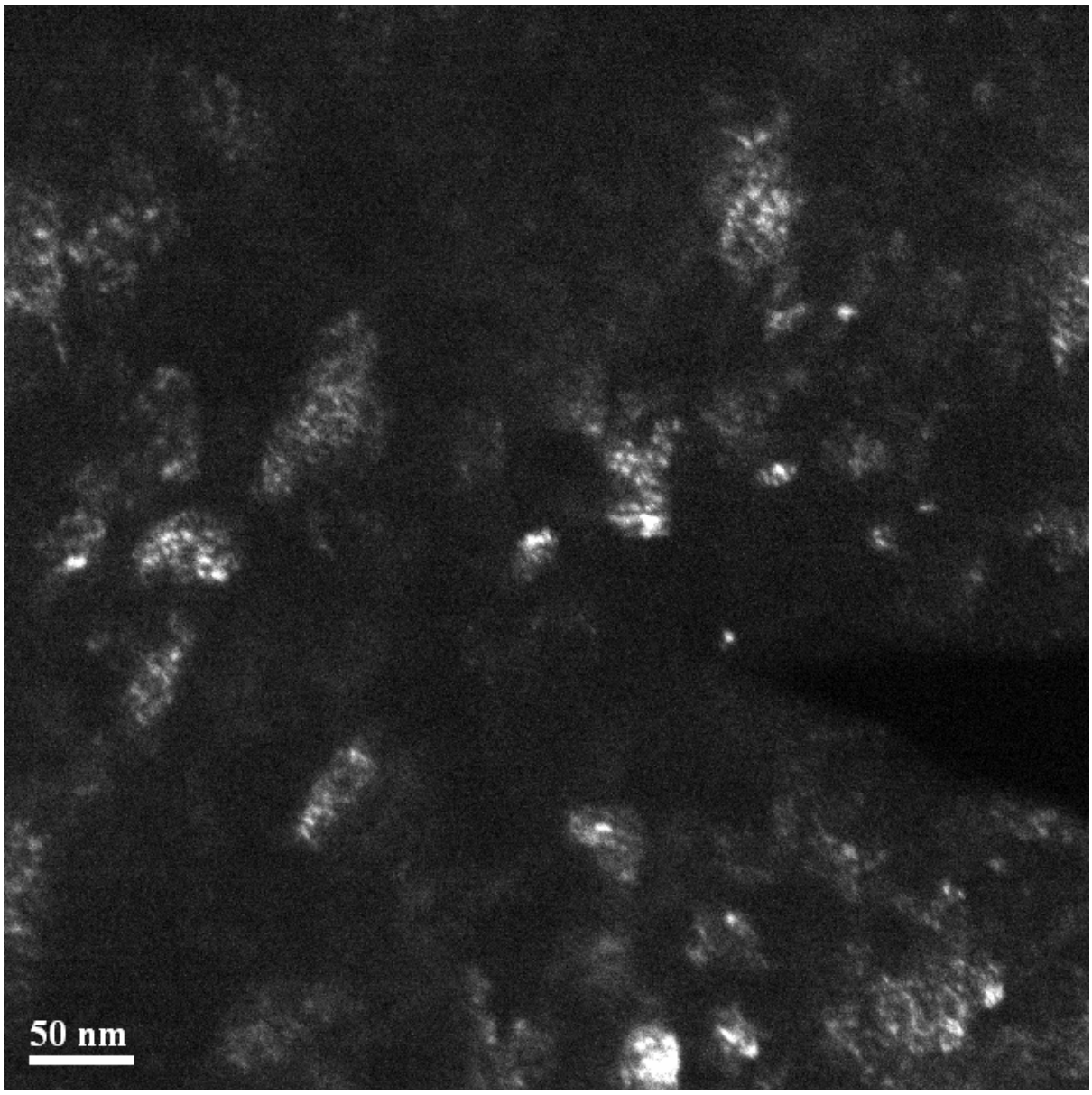

Figure 4.13 The dark field image of nanocrystalline Zr thin film deposited at 400 °C.

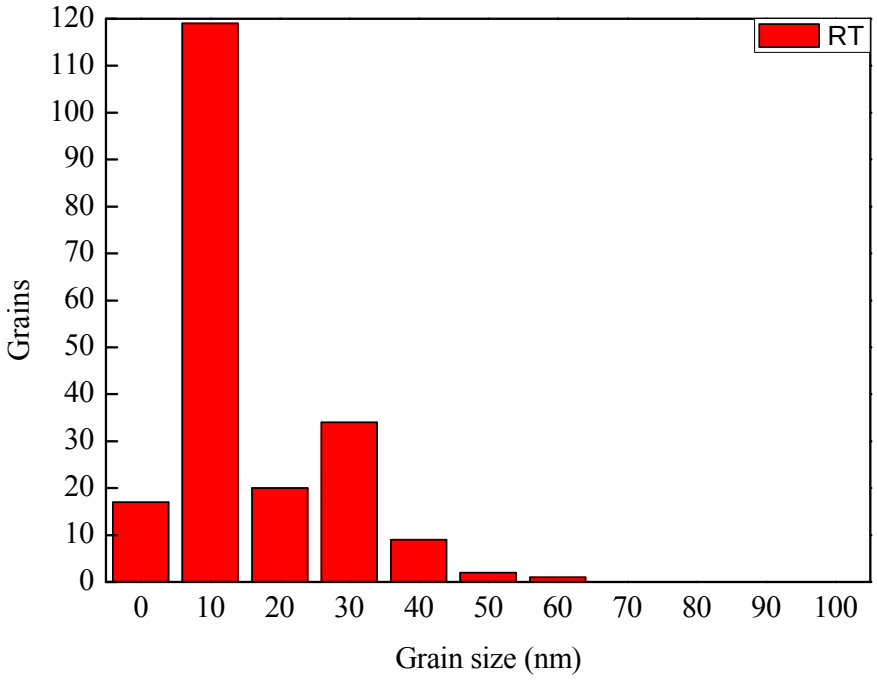

Figure 4.14 The distribution of grain sizes in nanocrystalline Zr thin film deposited at room temperature.

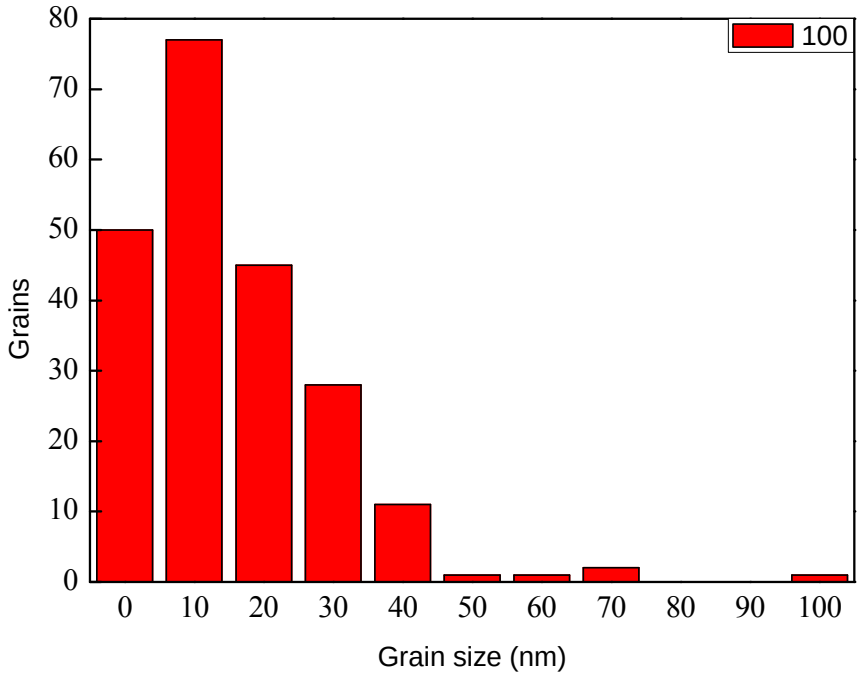

Figure 4.15 The distribution of grain sizes in nanocrystalline Zr thin film deposited at 100 °C.

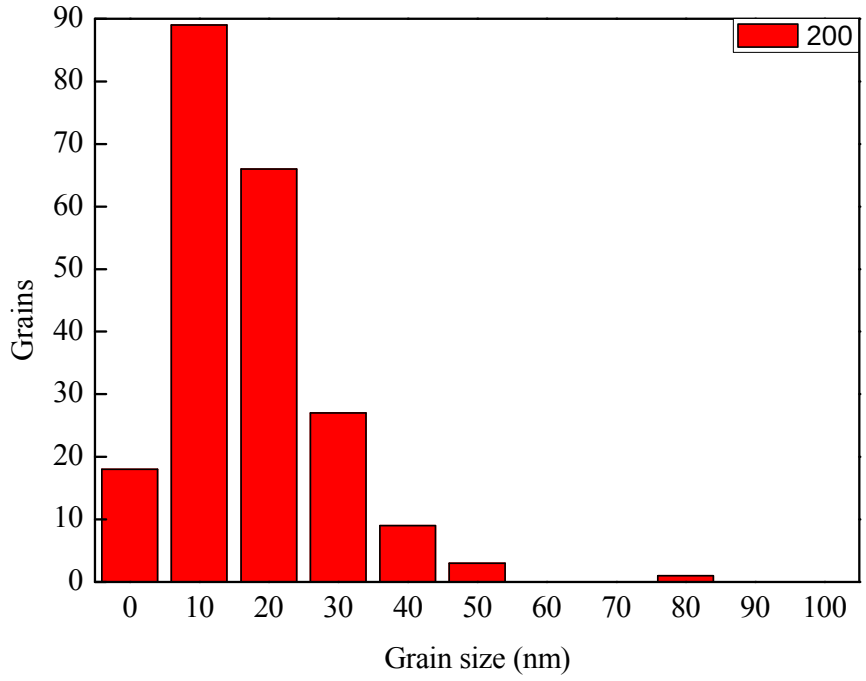

Figure 4.16 The distribution of grain sizes in nanocrystalline Zr thin film deposited at 200 °C.

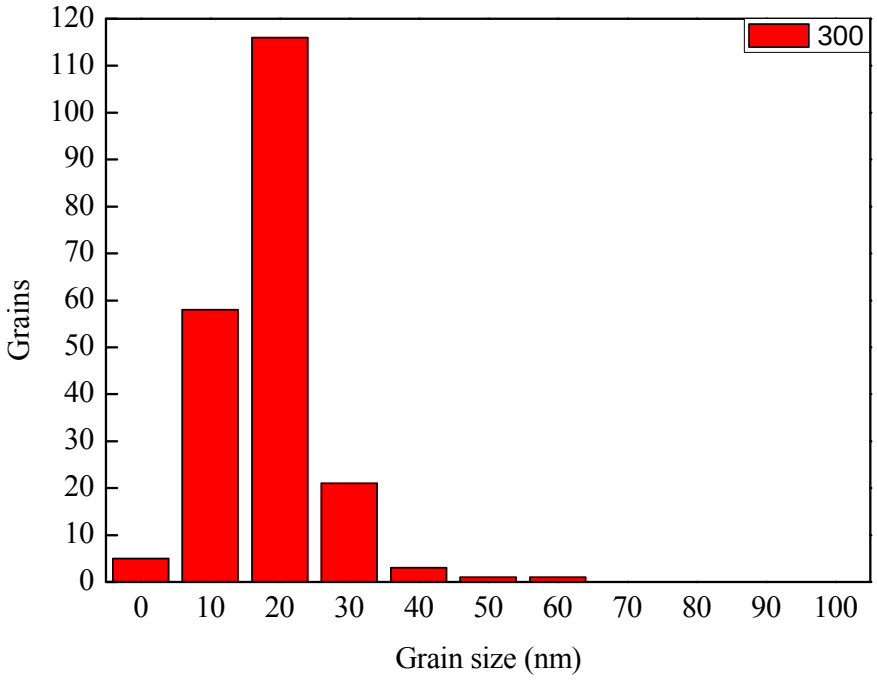

Figure 4.17 The distribution of grain sizes in nanocrystalline Zr thin film deposited at 300 °C.

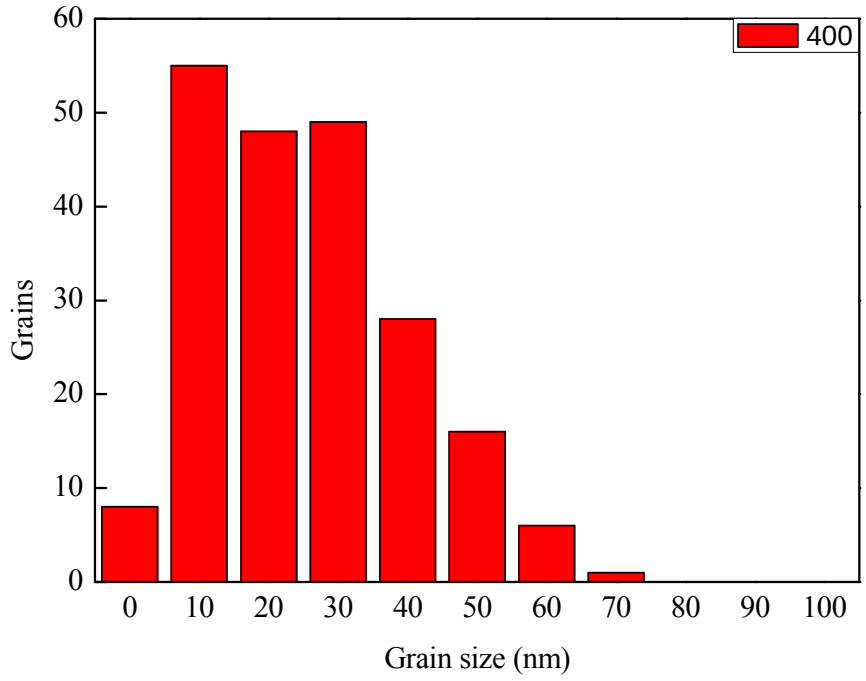

Figure 4.18 The distribution of grain sizes in nanocrystalline Zr thin film deposited at 400 °C.

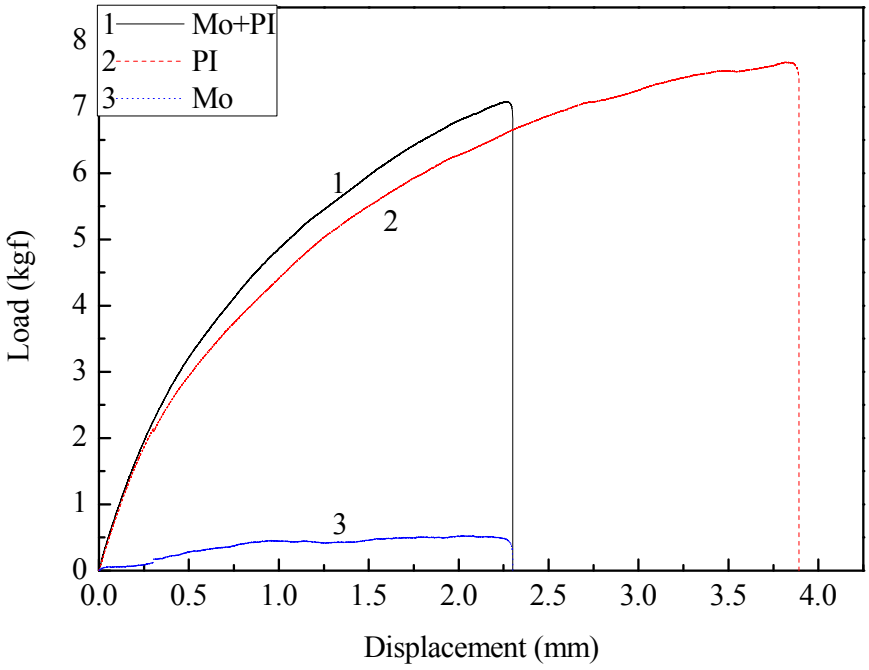

Figure 4.19 The load-displacement curves of Kapton foil, and 3.6 μm-thick nanocrystalline Mo thin film on Kapton foil at a strain rate 10^{-4} s^{-1}. The curve of Mo is calculated out.

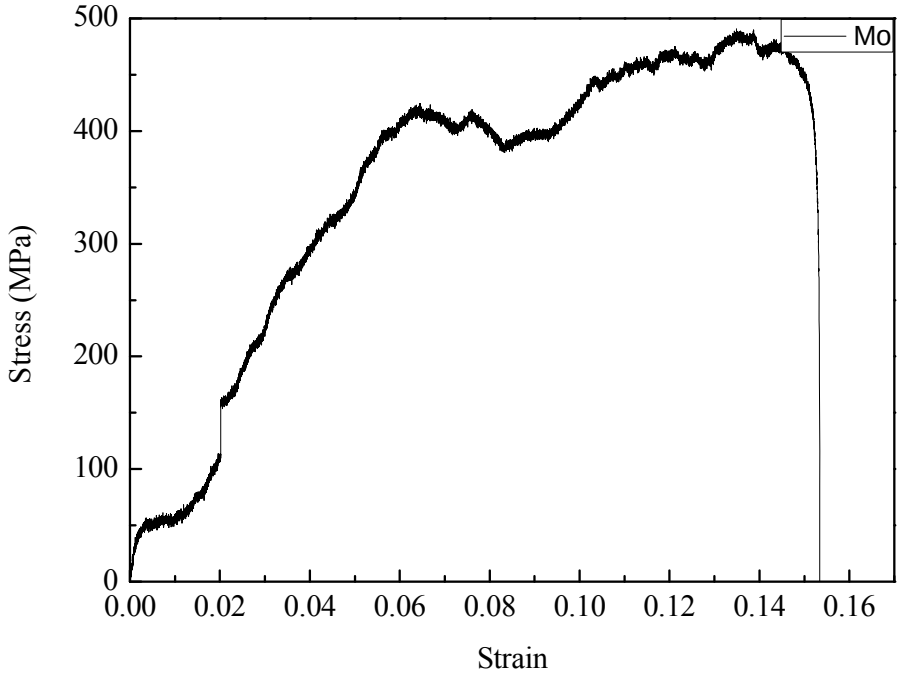

Figure 4.20 The stress-strain curve of 3.6 μm-thick nanocrystalline Mo thin film at a strain rate 10^{-4} s^{-1}.

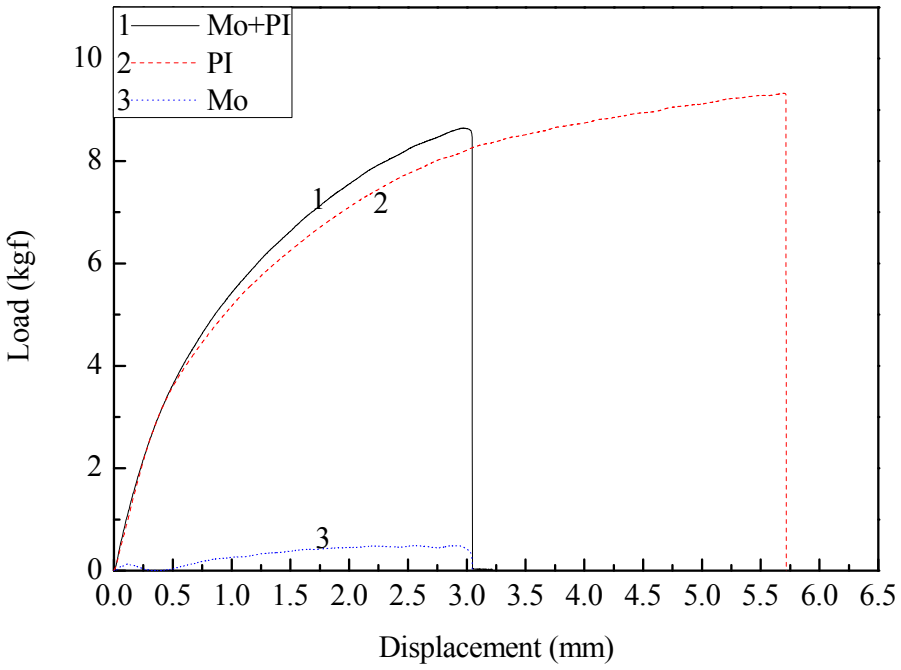

Figure 4.21 The load-displacement curves of Kapton foil, and 3.6 μm-thick nanocrystalline Mo thin film on Kapton foil at a strain rate 10^{-3} s^{-1}. The curve of Mo is calculated out.

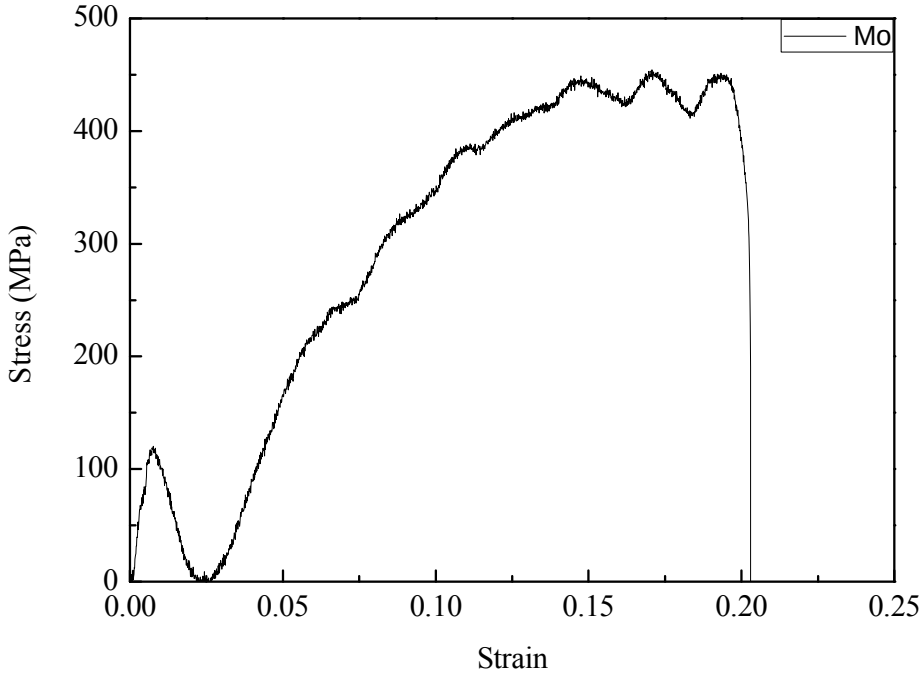

Figure 4.22 The stress-strain curve of 3.6 μm-thick nanocrystalline Mo thin film at a strain rate 10^{-3} s^{-1}.

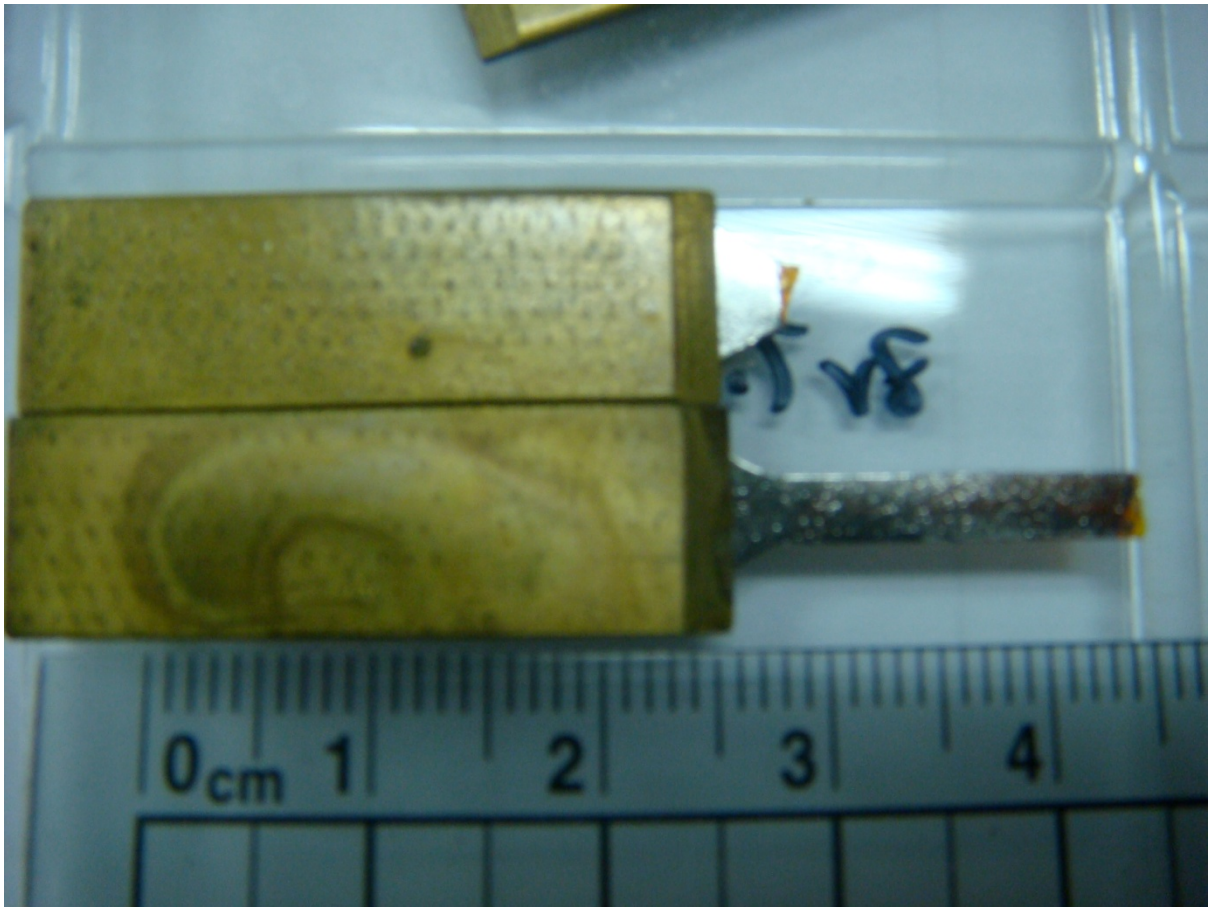

Figure 4.23 The sample after tensile test at a strain rate 10^{-4} s^{-1}.

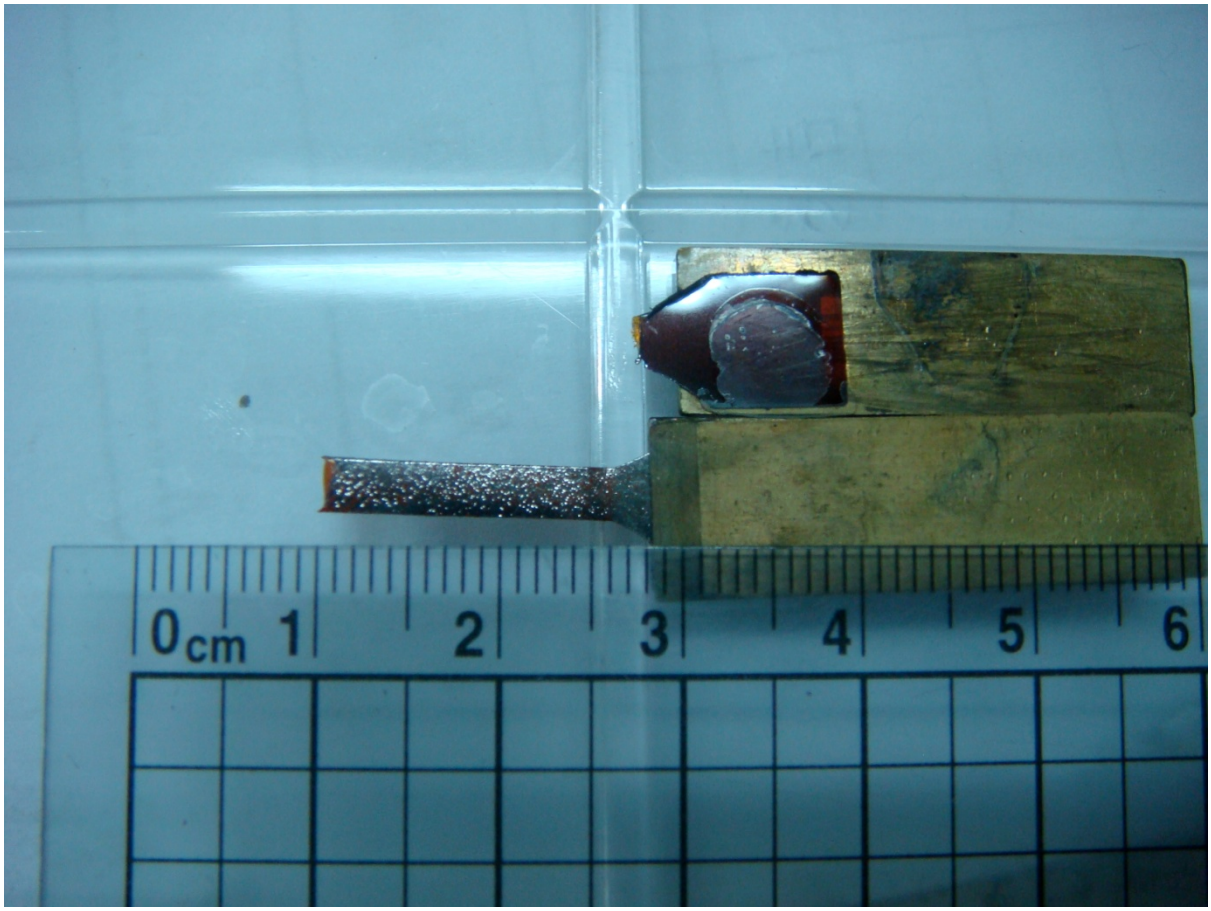

Figure 4.24 The sample after tensile test at a strain rate 10^{-3} s^{-1}.

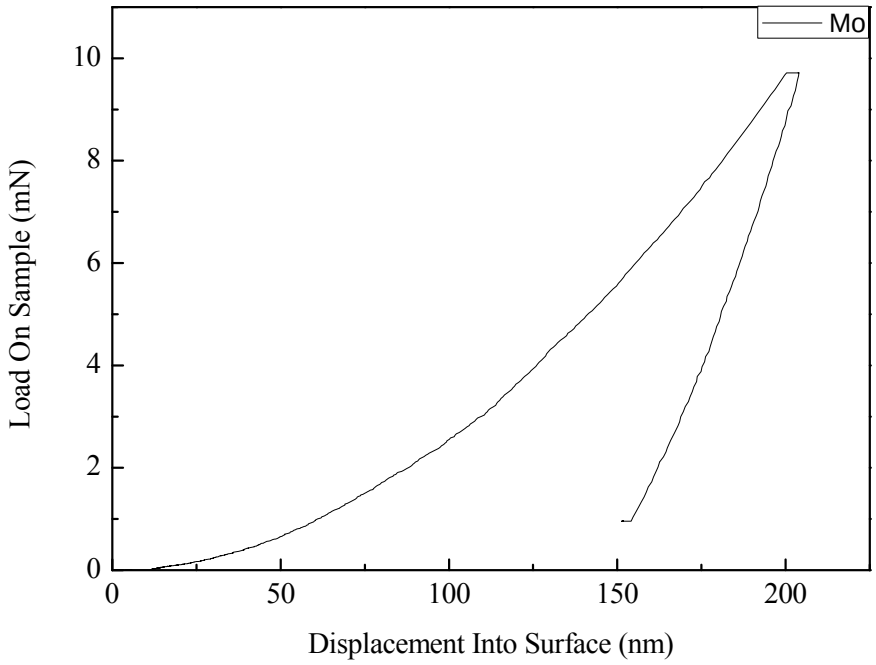

Figure 4.25 The load-displacement nanoindentation curve of nanocrystalline Mo thin film on Si at a strain rate 0.05 s^{-1}.

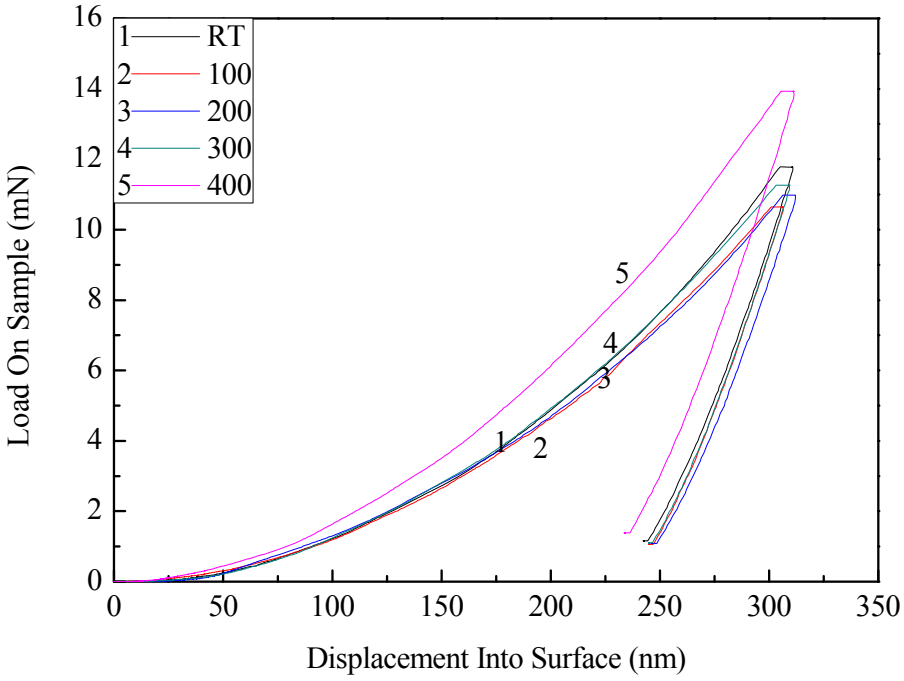

Figure 4.26 The load-displacement nanoindentation curves of nanocrystalline Zr thin films under the CSM mode.

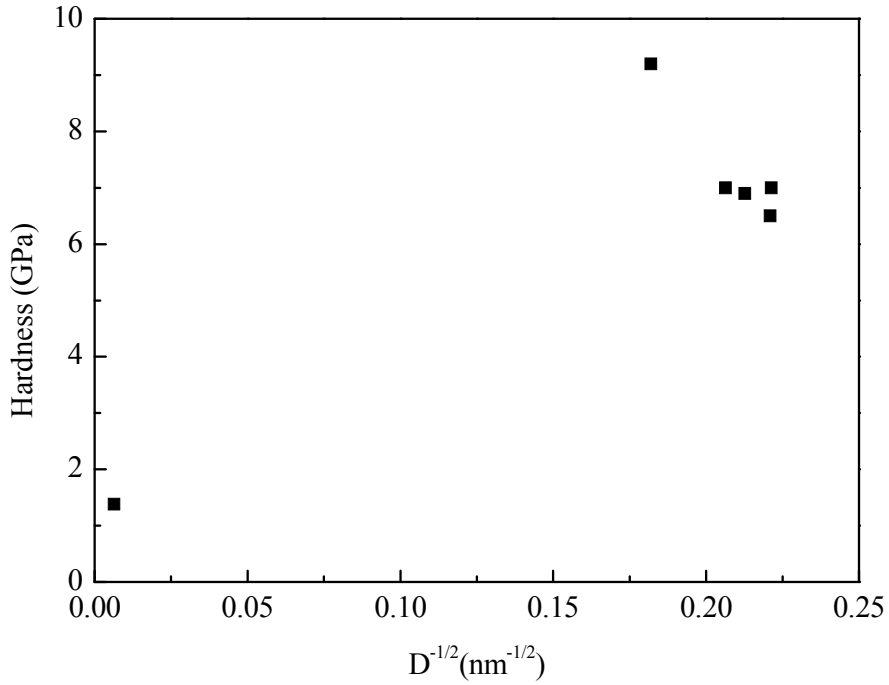

Figure 4.27 The relationship between hardness and grain sizes in nanocrystalline Zr thin films.

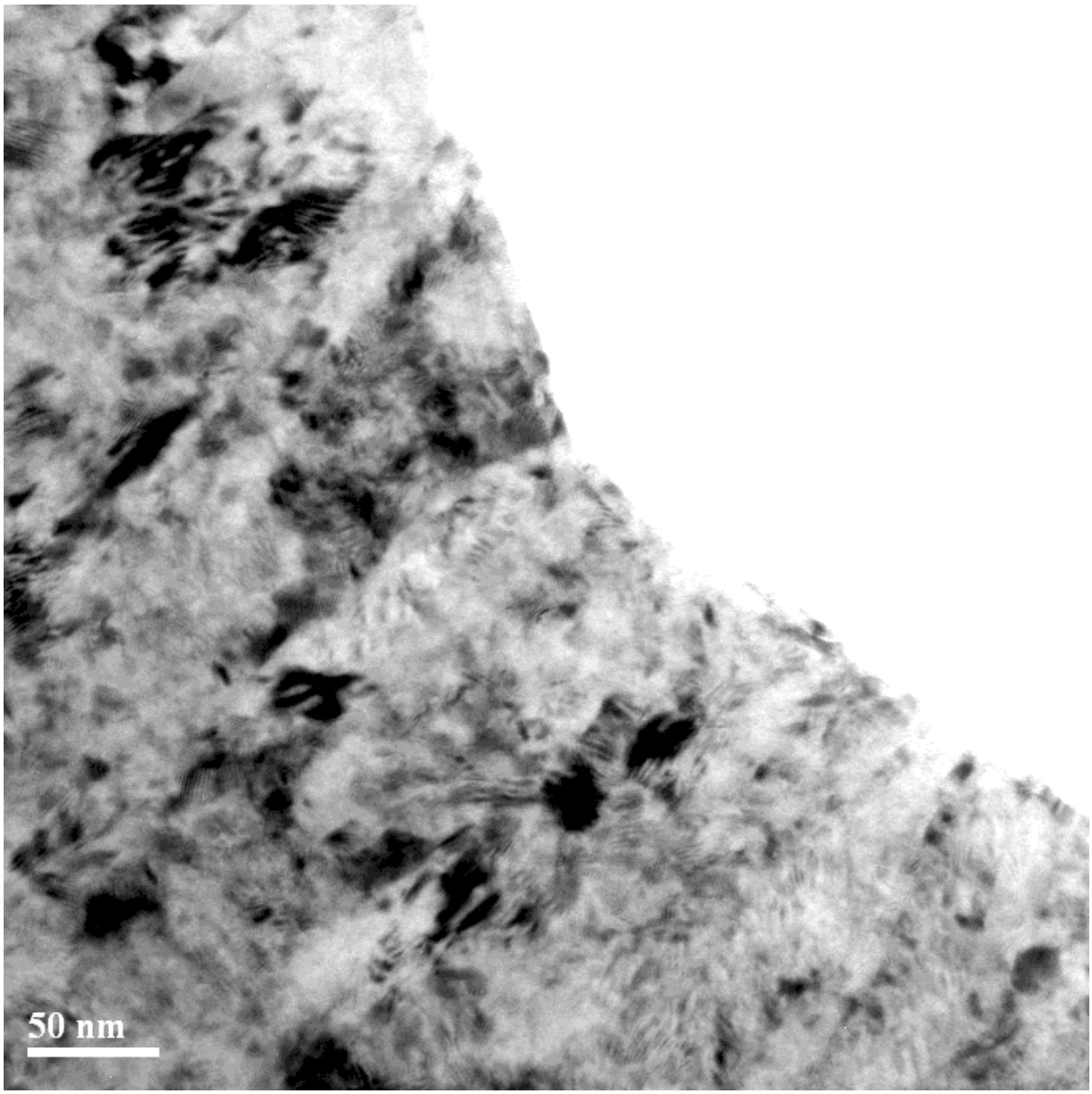

Figure 4.28 The cross-section of TEM micrograph of nanocrystalline Zr thin film deposited at room temperature after nanoindentation test.

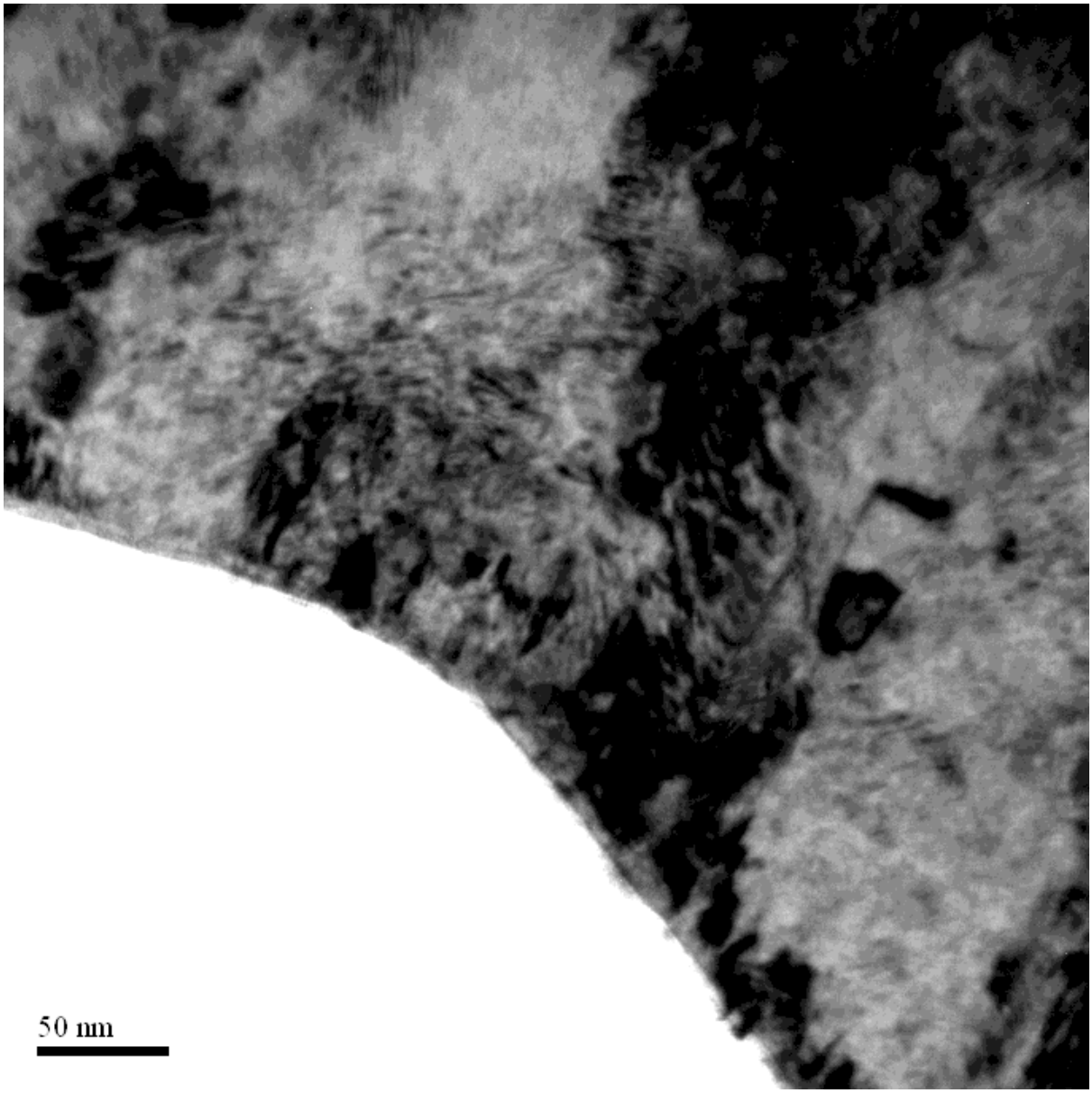

Figure 4.29 The cross-section of TEM micrograph of nanocrystalline Zr thin film deposited at 100 °C after nanoindentation test.

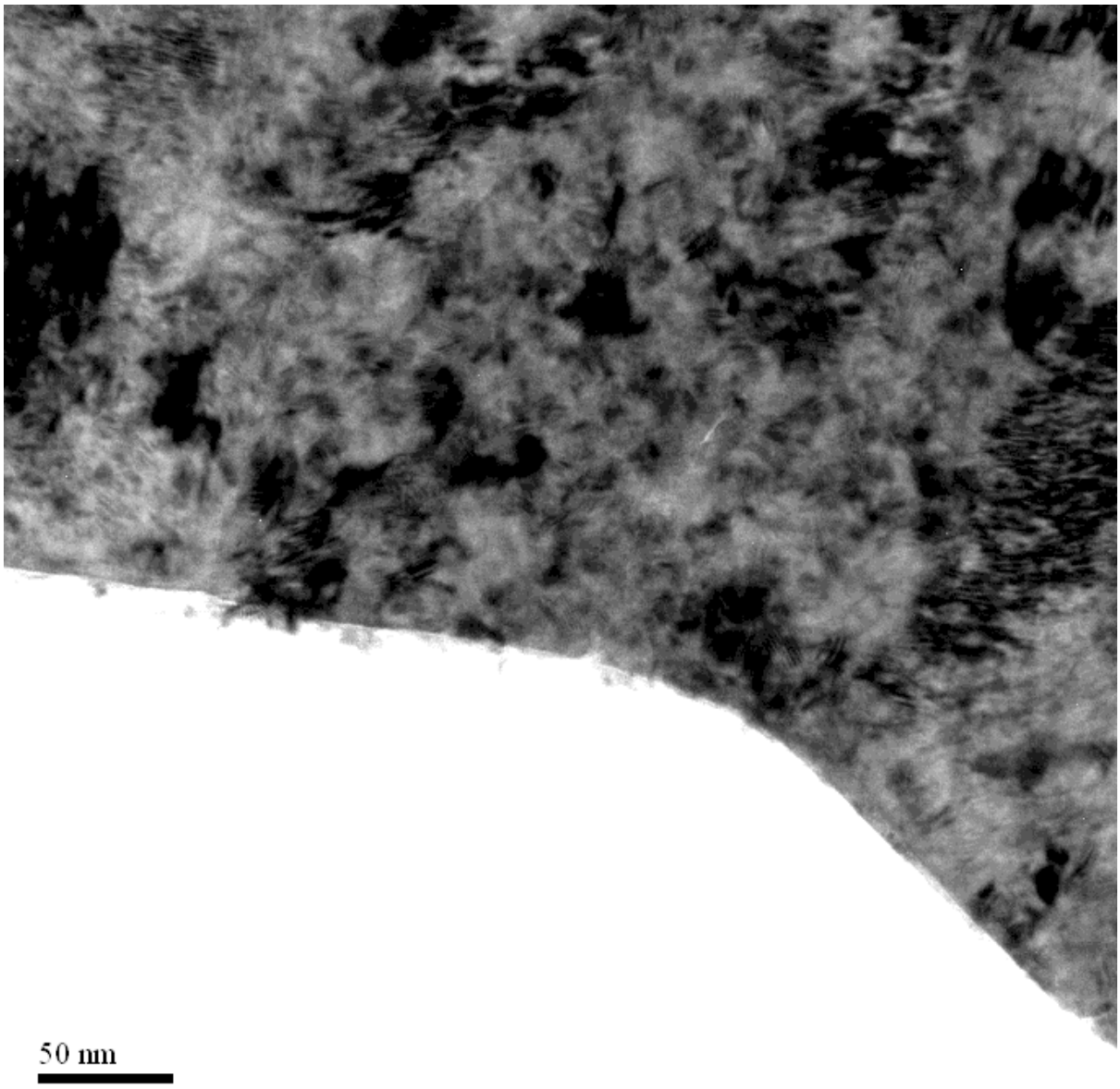

Figure 4.30 The cross-section of TEM micrograph of nanocrystalline Zr thin film deposited at 200 °C after nanoindentation test.

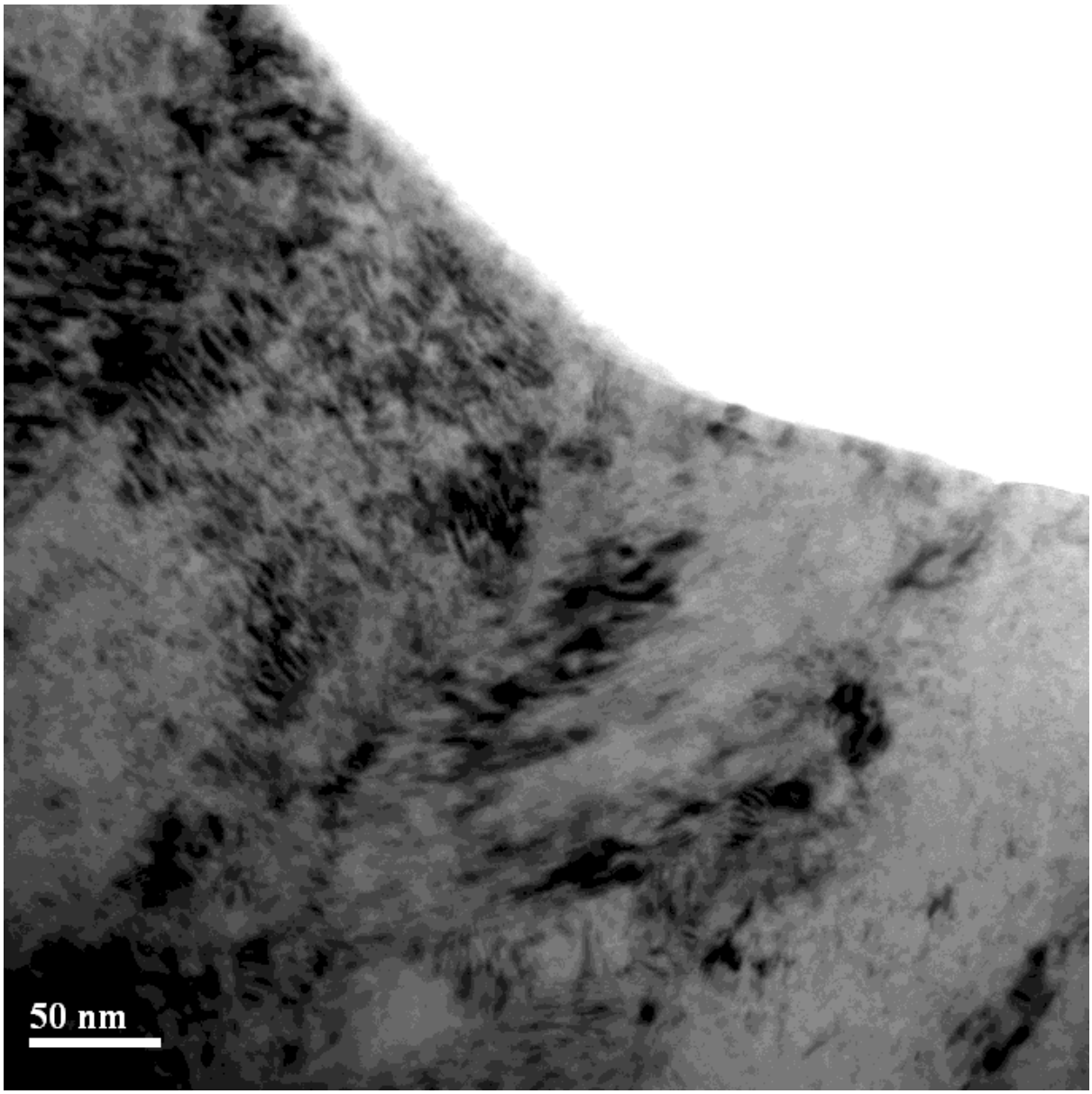

Figure 4.31 The cross-section of TEM micrograph of nanocrystalline Zr thin film deposited at 300 °C after nanoindentation test.

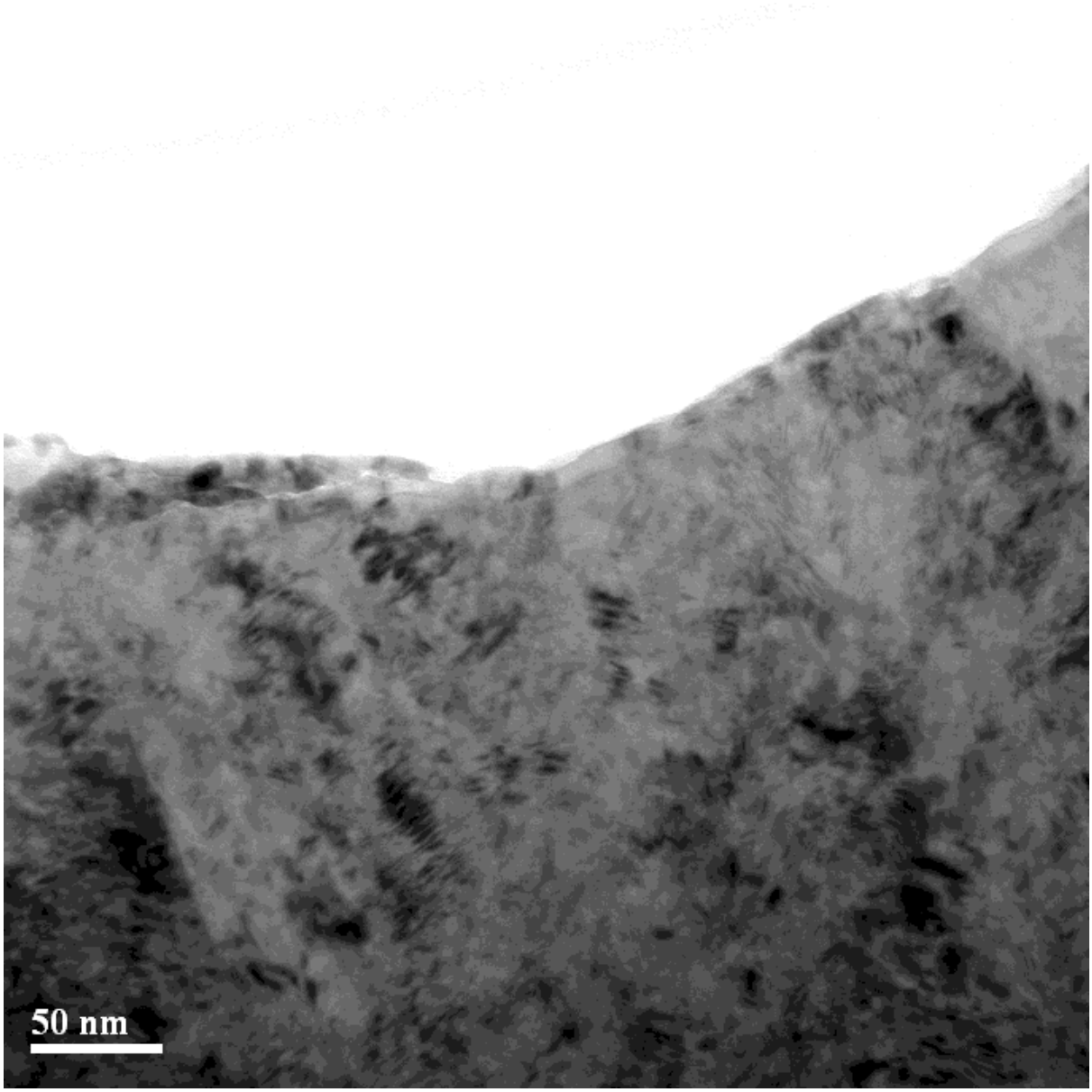

Figure 4.32 The cross-section of TEM micrograph of nanocrystalline Zr thin film deposited at 400 °C after nanoindentation test.